Polarimetric LiDAR for Target Characterization
Aiming at Autonomous Driving Implementations

Pedro Francisco Santos Braga Fernandesed

UMinho | 2019

Universidade do Minho
Escola de Engenharia

Pedro Francisco Santos Braga Fernandes

Polarimetric LiDAR for Target Characterization Aiming at Autonomous Driving Implementations

Julho de 2020

Universidade do Minho
Escola de Engenharia

Pedro Francisco Santos Braga Fernandes

Polarimetric LiDAR for Target Characterization Aiming at Autonomous Driving Implementations

Dissertação de Mestrado
Mestrado Integrado em Engenharia Física
Ramo de Dispositivos, Microssitemas e Nanotecnologias

Trabalho efetuado sob a orientação dos
Professor Doutor Eduardo Jorge Nunes Pereira
Doutora Irene Estevez Caride

Agosto de 2020

Acknowledgments

Without any particular order, I would like to leave it imprinted my most sincere appreciation, gratitude and recognition to the ones that either paved my academic path or somehow interfered positively in my life:

- To my advisor, Professor Eduardo Jorge Nunes Pereira, for giving me the opportunity of working in this project which allowed me to understand and fell the academic and company worlds, for the availability of always sparing his time with me, for always insisting on showing me the reality, despite my naivety, and for triggering my interest in the optics field.
- To my co-advisor, Irene Estévez Caride, for all tireless work spent in the lab, for showing me be beauty behind light polarization, for actively motivate me, and for always keeping my curiosity satiated and, somehow, craving for more, at the same time. For showing me that the lab can also be a joyful place.
- To all my team colleagues, in Bosch Chassis System Control and in the University of Minho, for embracing me in this internship and for the constant availability to listen and help me, and for the financial support offered by the company
- To my Bosch colleague, Luís Martins for his words of advice, for offering me one (not yet signed) copy of his book, and for the speared time between laughs and work in the lab.
- To my parents, Rosa Maria and Fernando, for the culture, education, opportunities, values, critical though, sacrifices and even for the discussions in our the dining table about politics or human rights, for agreeing and disagreeing with me, and most importantly for never letting me fell nulled and making our dining table the most warm.
- To my brother, Tiago, for not only being a brother but for being also a friend, for supporting and loving me unconditionally even if I stole his food, for teaching me how to walk, to teaching me the meaning and the necessity of protecting the ones we love the most.
- To my friend, D. Celeste, that since a youth fed me curiosity and discipline, for our snack breaks, and for giving me her most valuable advices, for telling me “o maior mal que te desejo é que sejas tão feliz quanto eu fui”.
- To my teachers, Carlos Pereira e Maria Cavaco, for the tenderness in their classes and for having encouraged my joy in science.

- To all my friends, for the dinners, for the trashy tv shows, for the most idiotic and non-sense talks, for the laughs, for the tears, for the making every moment a stunning memory, for somehow making my academic years a joyful and valuable path.
- To my best friends, Lau e Mi, for 13 years of friendship, for no-one standing us when we are together, for the confidence, esteem, respect and the protection, for never letting me alone and keeping my heart full of love for all this years, and for the unhealthy meals full of heathy thoughts.
- To my best friend Tiago, that never left me being and always pushed me forward. For the laughs, confidence, respect and protection. For being the brat that always makes me get out of my safe bubble and enjoy life as it is.
- To my one and only, for always letting me proud, for being my service psychologist and for making me feel good about myself, for all the secret notes and the secret ways to say "I love you", for being the shell to my shell and for loving me with all my flaws, but most importantly for being the reason my eyes smile. For being my person.

This work is supported by European Structural and Investment Funds in the FEDER component, through the Operational Competitiveness and Internationalization Programme (COMPETE 2020) [Project n° 037902; Funding Reference: POCI-01-0247-FEDER-037902].

STATEMENT OF INTEGRITY

I hereby declare having conducted this academic work with integrity. I confirm that I have not used plagiarism or any form of undue use of information or falsification of results along the process leading to its elaboration.

I further declare that I have fully acknowledged the Code of Ethical Conduct of the University of Minho.

LiDAR Polarimétrico de Caraterização de Alvos para Implementações na Condução Autónoma

Resumo

O LiDAR é um sensor ativo, utilizado para medir distâncias. Iluminando os obstáculos e medindo a luz retro-refletida, o LiDAR é capaz de medir a distância até um determinado obstáculo, bem como de prever a forma desse mesmo obstáculo.

Na condução autónoma, a elevada precisão e exatidão do LIDAR constituem uma enorme mais-valia para a tomada de decisões e para a segurança. O facto de ser uma tecnologia fundamental para a condução autónoma faz com que grandes empresas estão a alocar recursos ao seu desenvolvimento.

O projeto em que esta dissertação se insere tem como objetivo utilizar o conceito de polarização da luz no sistema LIDAR, a fim de permitir a classificação de alvos e facilitar o reconhecimento dos mesmos. No decorrer deste trabalho, foram construídos três diferentes Polarímetros de Mueller para considerar e avaliar a importância e utilidade da polarização na classificação de materiais. Dois setups foram desenvolvidos, com lasers de 1550 nm, nas instalações da Escola de Ciências da Universidade do Minho, sendo estes diferenciados pela utilização de diferentes componentes polarimétricos na geração e análise de estados de polarização: lâminas de quarto de onda ou cristais líquidos de atraso variável e polarizadores lineares. Os dois setups referidos e a informação polarimétrica obtida são apresentados neste documento.

O trabalho aqui apresentado envolveu, também, a construção de um quarto setup demonstrador de LIDAR, cujo objetivo era não só medir distâncias com elevada precisão e exatidão, como também introduzir componentes polarimétricas e reconhecer a importância da utilização de polarização na diferenciação de materiais.

Os resultados obtidos neste trabalho permitem concluir que a polarização, a um comprimento de onda de 1550 nm, tem uma importância muito significativa na classificação e reconhecimento de objetos. Conclui-se também que, um LiDAR de polarização a 1550 nm é capaz de distinguir entre pelo menos alguns materiais de elevada importância para a segurança de veículos autónomos.

Assim, propõe-se que seja prosseguida a linha de trabalho na polarização em sistemas LIDAR, de forma a aumentar as capacidades de reconhecimento do ambiente, em contexto de condução autónoma.

Palavras-chave: condução autónoma, LIDAR, LIDAR de polarização, classificação de materiais, matriz de Mueller, polarímetro de Mueller, polarização, vetor de Stokes.

Polarimetric LiDAR for Target Characterization aiming at Autonomous Driving Implementations

Abstract

LiDAR is an active sensor, used to measure distances. By illuminating obstacles and measuring retro-reflected light, LiDAR is able to measure the distance to a particular obstacle, as well as predict the shape of that obstacle.

In autonomous driving, the high precision and accuracy of LIDAR is an enormous asset for decision making and safety. The fact that it is a fundamental technology for autonomous driving means that large companies are allocating resources (monetary and intellectual) to their development.

The project in which this dissertation is inserted aims to use the concept of polarization of light in the LIDAR system, in order to allow the classification of targets and help their recognition. In the course of this work, different Mueller Polarimeters were built to consider and evaluate the importance and usefulness of polarization in the classification of materials. Two of the setups were developed, with a 1550 nm wavelength laser, in the facilities of the School of Sciences of the University of Minho, being different by using distinct polarimetric components to generate and analyse states of polarization: quarter wave plates or liquid crystals variable retarder and linear polarizers . The two 1550 nm setups and the obtained polarimetric information are described in this document.

The work presented here also involved the construction of a fourth setup: a LIDAR demonstrator, whose objective was not only to measure distances with high precision and accuracy, but also to introduce polarimetric components and to recognize the importance of using polarization in the differentiation of materials.

The results obtained in this work allow us to conclude that polarization at 1550 nm of wavelength has very significant importance in the classification and recognition of road scene objects. Moreover, a Polarization 1D LiDAR at a 1550nm is capable of distinguishing between at least some relevant materials of great importance in autonomous vehicle safety.

Therefore, it is proposed to continue this path of work on polarization in LIDAR systems, in order to increase the capabilities of recognizing the environment, in the context of autonomous driving.

Keywords: autonomous driving, LiDAR, Mueller matrix, Mueller polarimeter, material classification, polarization, polarization LiDAR, Stokes Vector.

List of acronyms

Acronym – Meaning

FoV – Field of View

HWP – Half Wave Plate

HLP – horizontal linear polarization

IEC – International Electrotechnical Commission

LiDAR - Light Detection and Ranging

LC – Liquid Crystal

LCP – Left Circularly Polarized

LCVR – Liquid Crystal Variable Retarder

LP – Linear Polarizer

LP$\pm 45°$– linearly polarized at $\pm 45°$

MCP – microchannel plate

MEMS – Microelectromechanical systems

MMT – Micro Motion Technology

M – Mueller matrix

$\mathcal{M}$ – Normalized Mueller matrix

M_{ij} – Mueller matrix ij element

m_{ij} – Normalized Mueller matrix ij element

OPA – Optical Phased Array

PMT – Photomultiplier Tube

PSA – Polarization State Analyzer

PSG – Polarization State Generator

QWP – Quarter Wave Plate

RCP – Right Circularly Polarized

S – Stokes Vector

$S_{0,}\ S_1, S_{2,}\ S_3$ – Stokes parameters

SPAD – single-photon avalanche diode

TCSPC – Time-Correlated Single Photon Counting

ToF – Time-of-Flight

VLP – vertical linear polarization

Index

List of Figures

List of Tables

1. Introduction

1.1. Context

There might be no greater invention, in the last century, which has influenced human behaviour as deeply as transportation vehicles. The majority of us uses automobiles on our daily basis, as our primary way of transportation. In fact, it is estimated that over one billion passenger cars are on the road worldwide [1].

Despite the importance of automobiles, today's cars are "grossly inefficient", whenever we are talking about human health, energy or human productivity [2]. Only in the last year, there were over 2.5 million car accidents recorded of which resulted in around 400 thousand injured passenger or pedestrians and 3 thousand fatalities [3], moreover transportation directly generated about 23% of global carbon dioxide emissions [4], [5].

The presented problems made automakers ideate new vehicle designs to keep up with the consumer necessities [6]–[11]. These demands have conducted human development to the introduction of autonomous driving, improving safety, comfort, convenience and energy efficiency [6], [8].

Statistics predict that Automated Vehicles will come with improved engines and designs, as well as better traffic management. These improvements will result in a lot less fuel usage [12]–[14]; accident savings, either in healthcare-related costs or car repairs [12]; and productivity gains, since the time used to drive can be then used to develop deskwork and goods transport can be made by analysing traffic and improving traffic flow, avoiding daytime traffic [12], [13] .

Lately there has been an increasing amount of publications on this subject matter, driven by the engagement of the market player to develop their own expertise. It is expected that, the global ADAS (Advanced Driver Assistance System) market will reach approximately USD 67 billion by 2025, at considerable annual growth rate of 19% [15].The enormous efforts being made by companies like BOSCH Group made possible that experts plan to market the first autonomous vehicles in the coming years (such as BMW [16], Volvo [17] and the PSA Group [18]) [8].

1.1.1. The Levels of Automated Driving

Although there is not a completely autonomous car yet, some technology advances in Automated Driving have been developed and some automated functions have been implemented in modern vehicles. For this reason, in order to provide a taxonomy for vehicle automation, the Society of Automotive Engineers (known as SAE), conceived the standard J3016™ in 2014 [19]. This document has the intent of promoting a common language for discussions and a foundation to further development activities in the automotive field [20]. This report evidences "the motor vehicle ranging" in six levels, from 0 (no automation) to 5 (full automation) evolving continuously. The latest J3016 graphic, shown in Figure 1, was presented in 2019. The scope of this visual chart is to simplify and clarify the "Levels of Driving Automation" for costumers. For these reasons, the "Automated Driving" levels are descriptive and technical, rather than normative or legal standards.

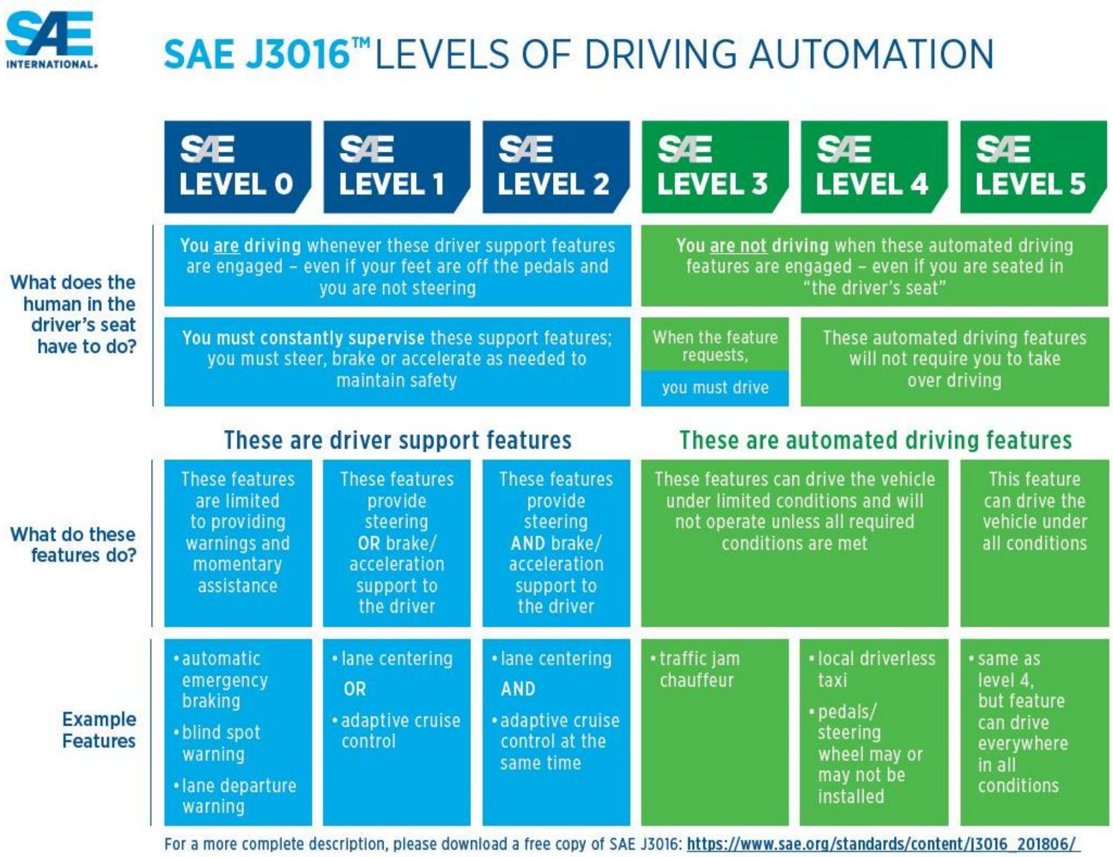

Figure 1. SAE Standard J3016 automated-driving graphic to simplify and clarify the "Levels of Driving Automation" (from reference [21]).

In a level 0 of automation, the human driver makes the full-time performance and all the driving tasks (see Figure 1). More precisely, the system can intervene shortly, but the control of the vehicle is always in charge of the human driver. In the level 1, also named as “Driver Assistance” level, the system may take control of some variables, such as acceleration and deceleration, taking into account the information acquired about the environment, but always with the expectation that the human driver is still in charge [22]. The human driver has to constantly monitor the vehicle and, in case of system failure, the driver has to be capable of taking corrective actions immediately, at any time [23]. In the level 2, or “Partial Automation” level, the system takes full control of the execution of steering and acceleration or deceleration under certain conditions, considering the environment. The system controls longitudinal and lateral vehicle motion in defined use cases [23], and the driver must be aware to interfere immediately in case of the occurrence of a failure in the automated system [22]. At the level 3, called the “Conditional Automation” level by SAE, the driving tasks are in the system responsibility, but only in defined use cases [23]. Meaning that the human driver is only needed to intervene in case of a system request [22] (i.e., a failure occurs or system limitations are reached [23]). At the level 4, or “High Automation” level [22], the driver is no longer needed to be watchful, even if the limits of the system are reached or a failure occurs [23]. The vehicle is self-driving in most scenarios and, if not, it is capable of correct a not appropriated response of the driver to a request to intervene. The level 5 is the last level, the “Full Automation” level [22], and it contemplates the full-time performance by the automated system. Note that in case of a system failure, the system is still responsible of the driving task and of the vehicle’s safety performance [23]. In this sense, the system is capable of handling every possible scenario, meaning that, at this stage, the pedals and the steering wheel are no longer included.

At this moment, several ADAS levels (1 and 2) are being implemented by multiple companies, progressively achieving autonomy. For example, it was estimated that *Tesla*'s autonomous vehicles had logged about 3 billion kilometres in October 2019 [24]. Concerning level 3 systems, it was claimed that Hyundai Motor, in partnership with *Glovis*, completed 40 km on highway in South Korea in August 2018 [25]. In addition, the Audi A8, launched in 2018, claimed to be a level 3 automated driving system that can take control of the majority of the driving tasks below 60 Km/h [26]. Since 2016, *Renault-Nissan* has been collaborating with *Microsoft* and later with *Waymo* to work on self-driving car technology for its vehicles, planning to release autonomous cars in urban conditions in 2020 [27]. *Tesla* ’s CEO Elon Musk suggested that *Tesla* will be fully autonomous by the end of 2020 [27].

1.1.2. Perception Sensing and the Autonomous Vehicle

The much needed autonomous vehicles incorporate various technologies such as processors, mapping, software algorithms and sensors. The referred technologies are designed to remove the onus from the human driver. To complete this goal, certain requirements are necessary, such as obstacle detection and trustworthy processing, decision-making, and possible obstacle avoidance, all in real-time. As one might realize, sensing systems for autonomous driving technology are an essential and challenging task. In this sense, one of the main open challenges is to detect and recognize different kinds of static or moving objects, as pedestrians, road signals or cars; or to analyse the road conditions. To improve the detection process, multiple sensors might be included in autonomous vehicles providing data diversity and redundancy [28]. This is called Sensor Fusion [29].

Sensors to automotive purposes are divided into two categories: active and passive [30]. Passive sensors simply gather information about and from the environment without the need to emit a wave [30]. In this category, cameras might be the most accurate way to create a visual representation of the world [28]. On the other hand, active sensors emit energy in the form of waves onto its surrounding, acquire the reflected wave and analyse it to position various objects within the Field of View (FoV) of the sensor. As examples of this sensor's category are Radars, Sonars and LiDARs [31], [32] (see Figure 2).

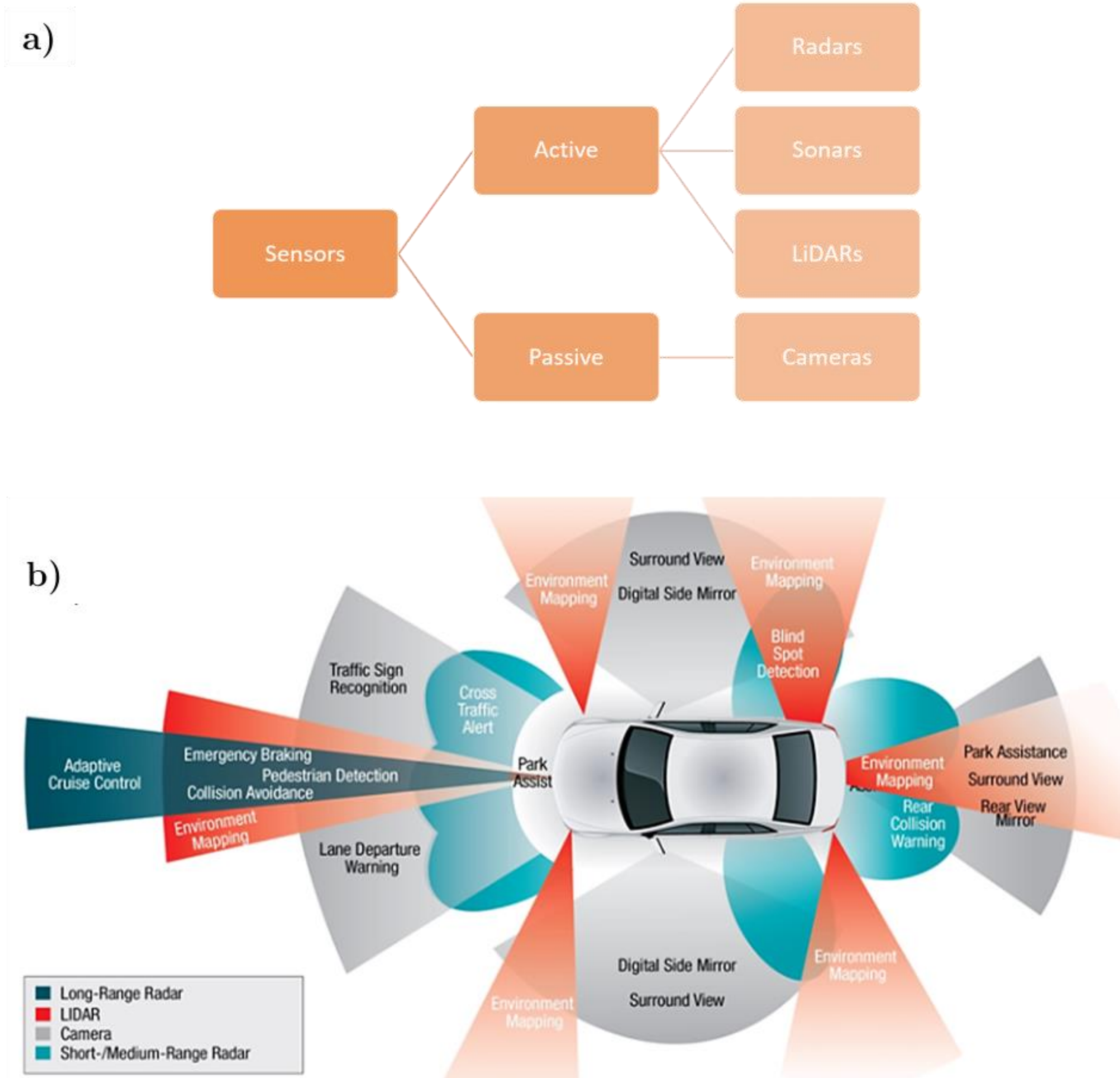

Figure 2. a) Chart of Surroundings Sensors. b) Schematic representation of Surrounding Sensors capability of self-driving vehicles (dark and light blue denote Long-Range Radars and Short/Medium-Range Radars, respectively, red denotes LiDARs and grey denotes cameras). Image from reference [33].

Cameras

As referred above, cameras are passive sensors. The majority of nowadays vehicles feature some sort of visible light cameras to provide video streaming to the driver. Stereo cameras are incorporated for detecting and recognizing small obstacles and for 3D mapping in a range greater than 15 meters [34].

By far, between the most common driving sensors, cameras are the most inexpensive and available optical sensors in the market. Different sensing functions are implemented by combining cameras and smart algorithms [35]. For example, stereo cameras capture scenes from more than one viewpoint and, by using various techniques such as triangulation, frame differencing or background subtraction, and based in the arrangement of pixels [34]–[36], it is possible to obtain depth perception of the surroundings, providing information about the position, distance and the speed of objects [28], [31], [37].

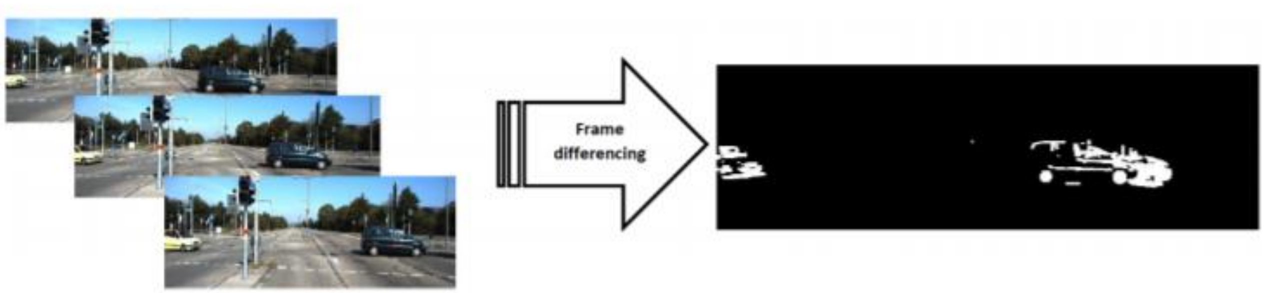

Figure 3. Frame differencing with a static camera. The moving cars are determined by calculating the difference between consecutive images (Figure from reference [35]).

However, cameras have some significant drawbacks, such as night-time and bad weather conditions that might not allow an efficient recognition or may even not be capable of recognizing street objects [34]. These disadvantages are expected of being compensated by integrating other types of sensors. In addition, cameras also have an enormous amount of data, which implies slow algorithms cannot make them real-time reliable [37].

<u>Radars</u>

Nowadays, automotive radars are already used in adaptive cruise control, allowing them to supplement cameras in low visibility conditions, improving object detection [31], [36]. Note that since radars are active sensors, they work by emitting either electromagnetic pulses or frequency modulation (FMCW) in the radio frequency (RF) spectrum, covering 360 degrees of the horizontal *FoV*. Once those waves hit an object, they are reflected and detected by the sensor, providing accurate data about objects' distance and speed. These pieces of information are determined either through the Time-of-Flight (*ToF*) or through the frequency shifts between the emitted and detected signal.

On the one hand, the *ToF* method is used to measure the distance between an object and a sensor, depending on the time difference of the emitted and returned signal (Δt) [35]. Knowing that the speed of light in the medium is c, then, the distance between the sensor and the object is $\frac{c\ .\ \Delta t}{2}$ [38]. On the other hand, the FMCW method measures the distance between a target and the sensor by measuring the frequency shift and its change in time.

FMCW radars are more widely used to autonomous driving than ToF radars. They can be incorporated into two different categories, as a function of their ranges and their final application: short-range and long-range sensing [30] (see Figure 2 b)). At this moment, Long-range radars, also known as 77GHz radars, range in frequency from 76 to 77 GHz[39], while the available Short-range radars are either narrow band (NB) short-range radars, which range in frequency from 24.05 to 24.25 GHz, or are ultra-wide band (UWB) Short-radars, ranging from 21.65 to 26.65 GHz [40]. Nevertheless, the European Union decided that 24 GHz radars will not remain valid from the January 1st of 2022 on [41].

Like automotive cameras, radar sensors can detect objects, determining distances and speeds. On the one hand, long-range radars have a low resolution but are capable of measuring speed and detecting targets that are up to 200m away [42]. On the other hand, short-range radars can also sense velocities and distances, but their resolution is limited by the complexity of the returning signals due to their broad beams and long wavelengths [42]. Compared to the other sensors on the car, radars are more efficient in bad weather conditions (rain, fog, ...). Nevertheless, radars have less angular accuracy, especially in the vertical direction [42]. At the end of this section, Table 1 compares more technical characteristics between automotive sensors.

<u>Sonars</u>

Sonars have been commonly placed in cars for parking finalities [30]. In the majority, this sensor's application is limited within a few meters, which it could be a disadvantageous, but they become ideal for low-speed use cases [30], [34]. The limitations of sonars are own to these systems being highly affected due to noise caused by external sources like traffic or due to the atmospheric attenuation [43]. This type of sensor has to operate in high frequencies of about 40-70KHz to make it fairly robust against acoustic noise [44]. Higher frequencies can also be used to improve resolution although, it will diminish its range [45].

As radars, sonars also make usage of the *ToF* principle, assuming now that the speed of sound in the air is $v_s \approx 343.2 \text{ m/s}$. The distance between the sensor and the obstacle is calculated by $\frac{v_s \, . \, \Delta t}{2}$, where Δt is the time lapse between the emitted and detected signal [38].

Despite the provided data from radars, cameras and sonars; these instruments are not sufficient for upper levels of automated driving. For this reason, other types of sensors are used for self-driving applications, such as LiDARs.

LiDARs

Light Detection and Ranging (LiDAR) is an active sensing technology that, as radars, operates either on the FMCW principle [46] or on the time-of-flight (ToF) principle, by illuminating the scene using a laser beam at eye-safe levels and measuring the return signal [47]. The 9xx nm and 15xx nm wavelengths are usually used in LiDAR systems owned to a conjugation of multiple factor like safety, water absorption and technology components (a further analysis is done in section 4.1.1).

The echoed signal are brought as a point cloud due to a beam scanning mechanism, creating a 3D image of the surrounding [30] (see Figure 4). Those echoed signals are just a portion of the light that was emitted. The distance to an objects is determined like radars, and its geometry and composition is determined by the amount of light and the properties changes made on it [48]. The detected information by LiDARs has tremendous importance that allows separating and classifying different objects, using segmentation and classification machine learning algorithms [48]. Meaning this that it allows the improvement of safety [49], and since safety's value proposition became as important as engine performance and fuel economy, it also became a concern to car manufacturers [49].

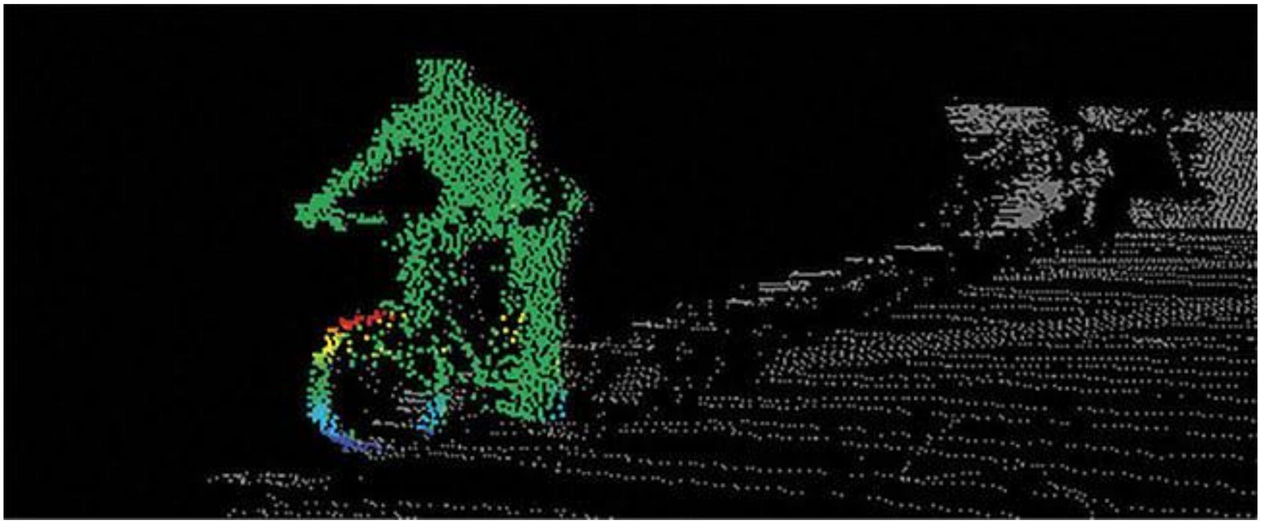

Figure 4. Representation of a Lidar's point cloud (from reference [50]*).*

To develop a system that is capable of recognizing obstacles and execute the safe procedures to avoid them, it is needed to involve all the referred technologies (cameras, radars, sonars and LiDARs). Table 1 summarizes the qualitative performance (using the five levels scale: Needs Improvement, Barely Satisfactory, Good, Very Good and Ideal Solution) of the different sensors, summarizing the finality of each perception system.

Table 1. Summary of the qualitative performance of the different technologies using the five levels scale: Needs Improvement (red), Barely Satisfactory (orange), Good (yellow), Very Good (green) and Ideal Solution (blue) (adapted from reference [49]*).*

	Radars		**Ultrasonic**	**Cameras**		**LIDAR**
	Short Range 24GHz	**Long Range 77GHz**		**Stereo Vision**	**Infrared**	
Short Range (0 to 2m)	Very Good	Barely satisfactory	Ideal solution	Barely satisfactory	Ideal solution	Very Good
Medium Range (2 to 30m)	Very Good	Very Good	Barely satisfactory	Barely satisfactory	Ideal solution	Ideal solution
Long Range (30 to 100m)	Barely satisfactory	Ideal solution	Needs improvement	Barely satisfactory	Good	Ideal solution
Narrow Vertical FoV <10°	Good	Good	Needs improvement	Ideal solution	Ideal solution	Ideal solution
Wide Vertical FoV >30°	Barely satisfactory	Barely satisfactory	Very Good	Good	Very Good	Ideal solution
Angular resolution	Barely satisfactory	Very Good	Needs improvement	Good	Very Good	Ideal solution
Object speed measurement	Ideal solution	Ideal solution	Very Good	Needs improvement	Needs improvement	Ideal solution
Bad weather operation	Ideal solution	Good	Good	Barely satisfactory	Very Good	Very Good
Blockage (impurity on sensor)	Good	Good	Good	Needs improvement	Good	Very Good
Night operation	Good	Good	Good	Needs improvement	Ideal solution	Ideal solution
Sensitivity to Light	Barely satisfactory	Barely satisfactory	Good	Needs Improvement	Good	Ideal solution
Cost	Very Good	Very Good	Ideal solution	Good	Barely satisfactory	Needs improvement

1.1.3. Sensor Fusion to Achieve Autonomous Driving Vehicles

Sensor Fusion is the combining sensory data or data resultant from sensory data such to produce improved data in the form of an internal adequate representation of the environment [51]. Achieving Sensor Fusion means attain robustness, extended spatial and temporal coverage, improved resolution and reduced ambiguity and uncertainty, leading to an increase of the system's confidence [51].

The goal of Sensor Fusion in Automated Vehicles (AVs) is building a more accurate scenario of the environment [30], [51], [52], since autonomous driving is a tremendously complex task (due to the different road topologies, climacteric conditions, speed limitations, pedestrians movement randomness…) of high responsibility (pedestrians, passengers, other vehicles…) [28], [49], [53] .

There are three not mutually exclusive fundamental types of sensors conjugation [52]:

- Complementary: Sensors do not directly depend on each other, but they are combined to give a more complete image of the scene under observation, solving the incompleteness of sensor data [51].
- Competitive: Sensors are competitively configured, whenever each sensor delivers independent measurements of the same property. This method allows detecting sensor failures and, in specific cases, this configuration also provides robustness to the system [51].
- Cooperative: Information provided by two independent sensors are used to determine the information that would not be available from one of the single sensors (e.g. a three-dimensional image can be achieved by combining two-dimensional images from two cameras at slightly different viewpoints) [51].

Recalling what it was mentioned before about vision sensors, sonars play a minor role in autonomous driving. Its applicability is directed to parking assistance in a short-range parking distance (due to the strong attenuation of ultrasonic waves). Regarding cameras, these instruments provide high resolution 2D pictures (Stereo Vision Cameras are even sensitive to colour), becoming vital in objects' classification and interpretation. Although the limited FoV of cameras might be a limitation that generates the need of multiple strategically integrated cameras to achieve a 360° coverage, the real issue comes with the data's lack of three-dimensionality and the strong dependence on exterior lighting. Regarding radars, its data is targeted to measure distances and speeds with independency of exterior lighting. It manifests itself as the most appropriated for longer ranges measurements and its great sturdiness in harsh weather conditions is noticeable. However, it has some important shortcomings in terms of resolution due to diffraction effects (radars do not differentiate shapes very well) and in terms of reliability. LiDARs are also indicated for distance measurements with external lighting independency. The LiDAR's shorter wavelength and greater beam properties of the emitted light waves offer a better choice for 3D imaging and point cloud generation, filling in the gap between cameras and radars. Nevertheless, LiDARs are not an ideal solution since bad weather conditions (such as rain, snow, fog, ...) [42] and blockage severely deteriorates its analysis. For these reasons, Sensor Fusion is recommended, not only to compensate flaws that each mentioned system might show, but also to associate, correlate and combine information from multiple systems to acquire a more refined, complete and timely estimation of the environment. In other words, Sensor Fusion data is robust, reliable, resilient and redundant. Figure 5 shows a distribution of sensors in Sensor Fusion for an automated vehicle.

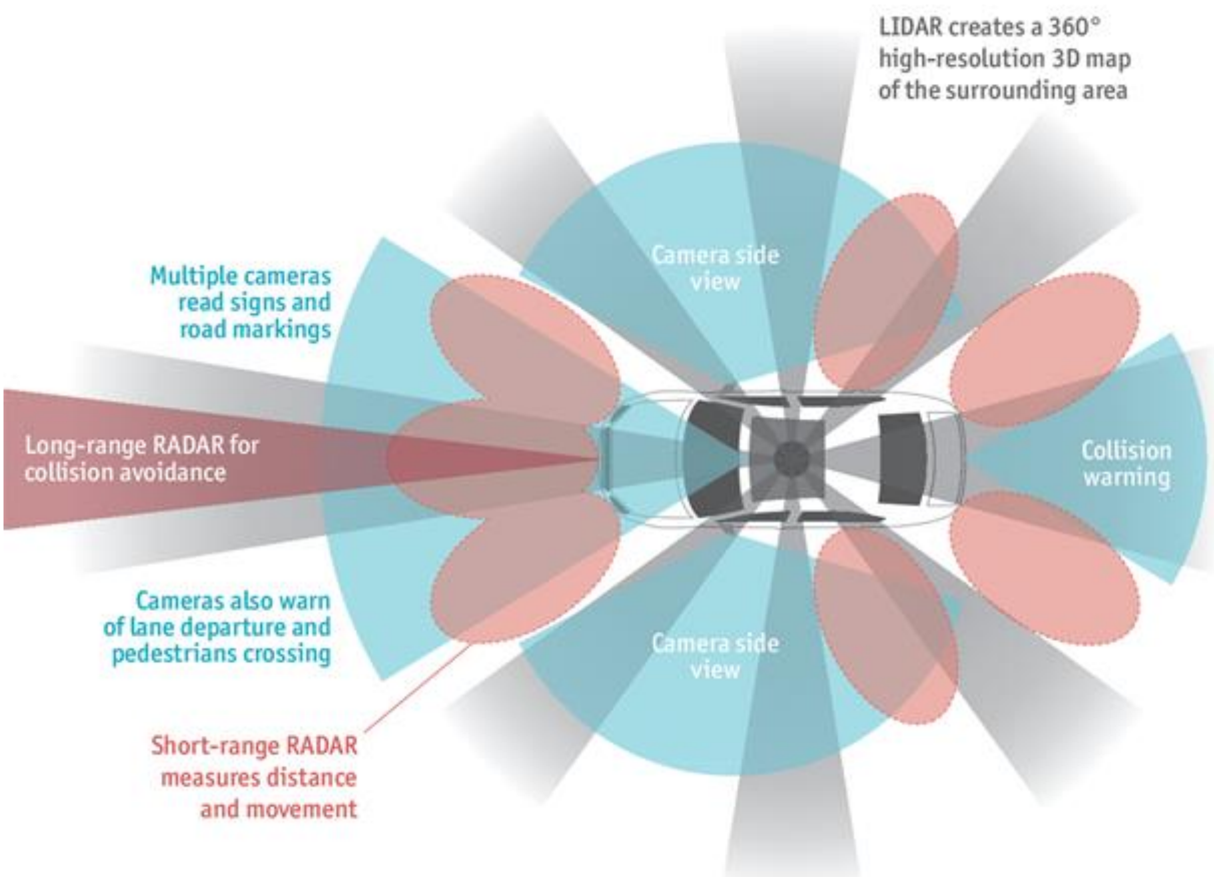

Figure 5. A Sensor Fusion distribution for an automated vehicle providing the autonomous vehicle visuals of its surroundings, combining cameras, radars and LiDARs. From reference [54]*.*

Note that, although perception sensors are the ones to return information about the environment, the interpretation of the acquired data is performed by a computing platform responsible for fusing all the data and recognizing objects. The processing unit evaluates the scene and decides about how to proceed and act in each situation. Figure 6 discretizes the elements predicted for higher levels of automated driving.

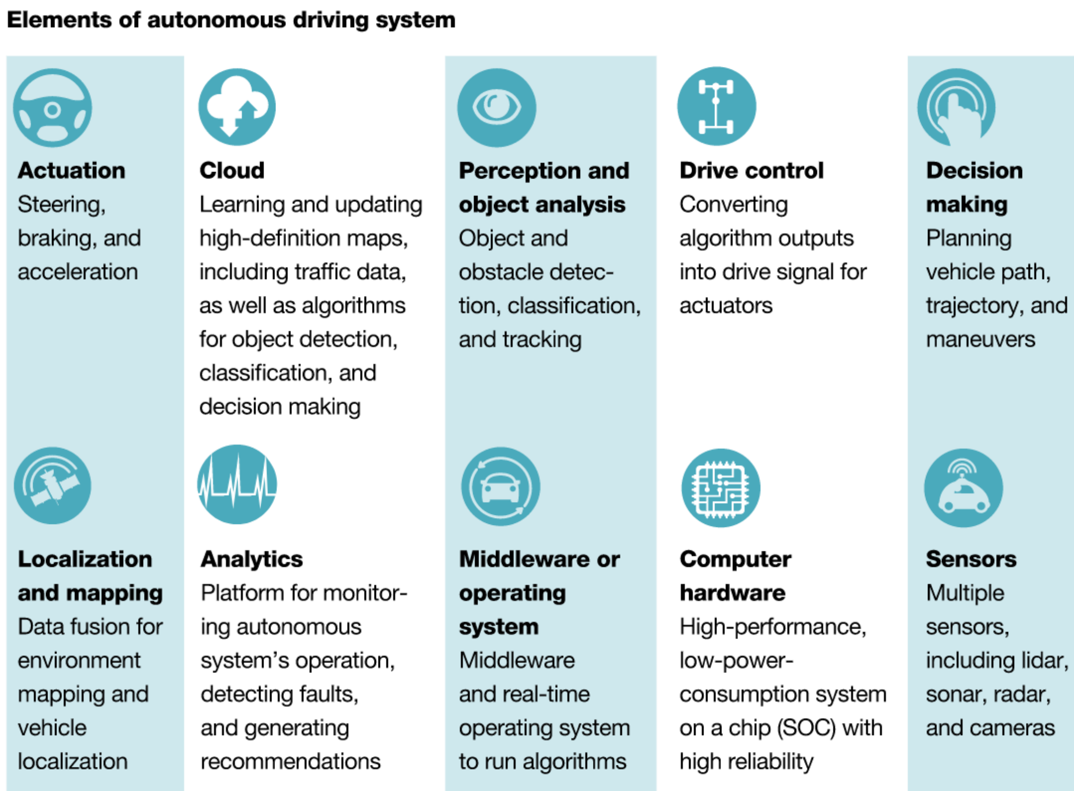

Figure 6. Elements of autonomous driving system. From reference [53].

In short, none of the sensors alone completely fits every case scenario and so, multiple various sensors are essential to correctly unambiguous visualize and timely interpret the vehicle's surroundings.

2. Motivation and Objectives

As one can understand from the chapter 1, LiDAR sensors are a key element to achieve greater levels of automations and it is expected having a major role in the sensors fusion for autonomous driving. Although LiDARs are already used in different fields, their application in the automotive market is not mature once compared with stereo cameras or radars, that are used intensively in other industries. Hence, the lack of development of this technology leads to current high price solutions, and without a doubt, compromises the development of a driverless vehicle.

The goal of the present work (and my master's thesis projects) was to implement a single point LiDAR capable of measuring distances and distinguish materials through polarization. To understand how the polarization of light should be implemented, a comprehensive polarization study was pursued. The motivation behind this study is that polarization properties of light may vary once interacting with matter. These changes depend on the wavelength and the sample rotation angle of the incident beam, and the characteristic properties of materials (roughness, refractive indices, ...). Thereupon, the backscattered light can provide information about the target material, supporting object recognition. In addition, the objective of this work is also to suggest an implementation of scanning system using a MEMS scanning micromirror to steer the beam vertical and horizontally, providing a 3D polarimetric LiDAR. The final objective of this thesis dissertation is not to implement a fully working LiDAR, but to acquired critical knowledge in LiDAR, polarization and the capabilities of integrating them as one. A fully apt LiDAR is an optical system of high complexity addressed by complete teams of multiple interdisciplinary areas of knowledge.

3. Framework and Content

This master thesis dissertation is composed of nine chapters that discuss subjects like: an introduction to LiDAR, a contextualization of LiDAR systems, the light polarization and its benefits to LiDAR, experimental work, conclusions of this thesis and recommendations of work to be done in the future.

- The first chapter aims to give a background of what an autonomous vehicle system is and the elements that should include, demonstrating the relevance of LiDAR in self-driving applications.
- The second chapter, that is a brief chapter, refers the motivation and objectives within the present master thesis dissertation.
- The third chapter explains the framework and content of this master thesis.
- In the fourth chapter, the LiDAR system is presented in greater detail and it is discussed the working principle of lasers and the safety classification of laser light systems, the detector used in LiDAR's systems and the main scanning technologies.
- The fifth chapter reports the geographical companies' distribution investing in automotive LiDAR systems and the state-of-the-art of the automotive LiDAR sensors. A comparison of some of the current systems in the market is summarized to show the variety of the available products. Some soon to entering in the market products is also referred. In this chapter, it is also discussed the polarization LiDARs and their current applications.
- The sixth chapter starts by giving a contextualization of the physical conceptualization of light waves, the concept of polarization and the Stokes-Mueller formalism. In addition, it is also discussed the experimental polarimetric measurement principle, two experimental 1550 nm Mueller polarimeter setups, and some conclusions derived from the study of the acquired data.
- In the seventh chapter, the 1D LiDAR's optical experimental setup and the electronics behind it are presented. An accuracy calibration is sought, and the system precision is evaluated.
- The eighth chapter features the experimental Polarization 1D LiDAR and presents a brief experimental study of its capabilities on distinguishing different material.
- The last chapter (ninth chapter) contains the conclusion of this project and some guidelines for future work.

4. The context of LiDAR

As it was introduced in Chapter 1, a LiDAR (Light Detection and Ranging) system consists on a laser or an array of laser sources [47], [55], [56] capable of emitting either continuous light either electromagnetic pulses over the desired FoV [47], [56], [57], and an efficient detector to accurately detect and track objects [58]. Furthermore, LiDARs typically work in visible and near infrared frequency ranges [47], [55], [56] (NIR wavelengths are usually used for terrestrial mapping [59]).

Figure 7 presents a conceptual diagram of a LiDAR system. The laser purpose is to emit light waveforms in order to obtain range information. In addition, specific electronic devices, capable of generating the desired waveform, control this element. The laser together with a high-precision clock only allows the detection of distance to an obstacle in its line of sight. In this sense, to acquire a two-dimensional field of view, a prospect system (scanning or non-scanning) is implemented to regulate horizontal and vertical directions [60].

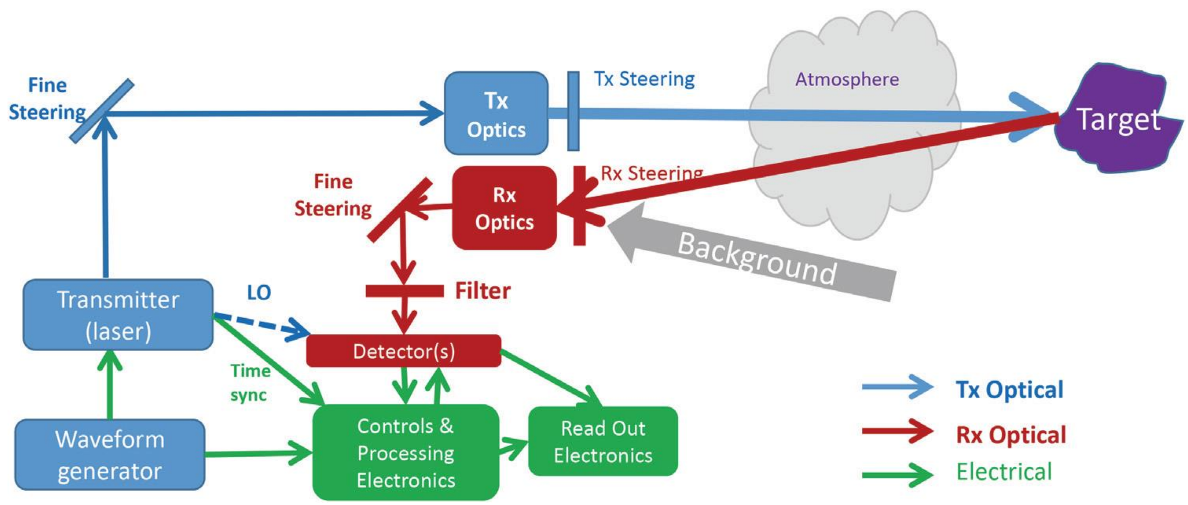

Figure 7. LiDAR Conceptual diagram [55]*: The transmitter (Tx) and receiver (Rx) components are in blue and red respectively and in green are the electrical components.*

Note that Figure 7 represents a bistatic system, where the transmitter (Tx) and the receiver (Rx) are completely separated, while in monostatic implementations, the light is emitted and received by the same aperture. The optical systems (Tx and Rx optics) in Figure 7 are integrated separately into the generator and receiver ends, respectively, to improve the Signal-to-Noise Ratio, i.e. to improve the sensing performance [55]. These systems are responsible for collimating and shaping the output beam (e.g. beam expanders [57]), focusing the reflected one into the detection system and filtering it to eliminate background noise (developing a better

Signal-to-Noise Ratio [55]), improving the sensor's overall sensitivity [55], [57]. Under the bistatic scenario, the background signal is significantly reduced and fewer photons that suffered multiple scattering can be manipulated to less likely to be detected [57], leading to a more precise system. In addition, a detection system is needed. The detected beam from the outcome light from the reflection reaches the light sensor and it is converted into an electrical signal. The signal is now amplified and stored, for it to be then digitally filtered and manipulated to achieve its purpose [55], [57], [61]. This is further processed by analog of digital analysis to eventually obtain the targets distance. The now obtained signal together with its direction is stored and processed to construct a point cloud [30] and then, to reconstruct the surrounding environment through recognition algorithms [30], [35].

The system is protected by housing [62], [63] to protect LiDAR from external damaging and thermal oscillations, which creates the need to have at least one optical aperture so that the generated light is able to reach the environment and come into the detector [55], [57].

The communication between the central processor, responsible for taking into account the data acquired from all sensors, and the information determined by LiDAR should be done by wired interface communication to avoid shielding by a metallic housing [62], [63]. A CAN (Controller Area Network) interface could be used to acquire the fastest and the most reliable results [64].

4.1. Major Devices in a LiDAR

In this section, the major devices in a LiDAR are described.

4.1.1. Laser Source

Physical Principle

A "light amplification by stimulated emission of radiation" (laser) is a device that emits monochromatic, coherent and highly collimated light through a process of optical amplification based on the stimulated emission within an amplifying medium, population inversion and on optical resonators [65]. To understand the physical principle behind these concepts, one shall recall that quantum mechanics forces electrons to take a discrete energy level once orbiting an atom [65]. Taking this into ponderation, one can consider two energy levels of electrons of which E_1 is the ground state and E_2 is the excited state (a higher electronic energy level). Whenever a photon, with energy equal to the energetic difference between the ground state and the excited one, is focused on an atom, the ground state electron gains enough energy to jump to the excited state E_2 (see Figure 8 (a)). In non-metal crystals, this phenomenon generates a pair electron-hole where one can consider there is an electron in the higher energy state and a hole in the lower energy state [65].

The electron, now in the excited state, can decay either by spontaneous emission (where electrons move naturally from one state to another, so the photon emission occurs naturally, meaning there is no control over the emitted light – incoherent light, see Figure 8 (b)), either by stimulated emission (it occurs when a passing photon is absorbed by an electron in the excited state and triggers the recombination of an electron with a hole, emitting a second photon with the same frequency, momentum and phase [65], [66] – coherent light, see Figure 8 (c)) [65]. The probability of a stimulated emission event to happen is inversely proportional to its time constant of decay [67].

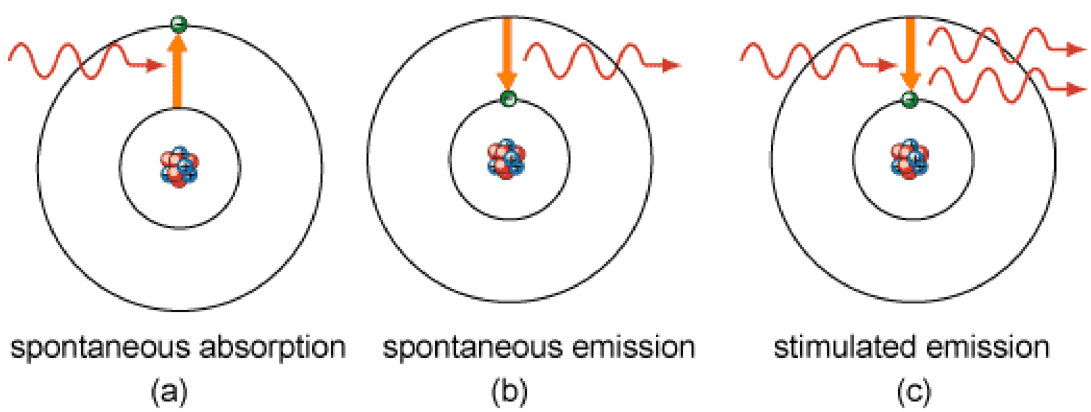

Figure 8. Electron transition in an atom. From reference [68].

Stimulated emission occurs when a passing photon is absorbed by an electron in the excited state and triggers the recombination of an electron with a hole, emitting a second photon with the same frequency, momentum and phase [66], [69], [70]. Unlikely spontaneous emission, stimulated emission guarantees that the big majority of the emitted photons have the same energy, phase and direction [69], [70]. This is because the system is designed in a way that the time decay of spontaneous emission is very long when it is compared with stimulated emission [69]–[71]. Note that in any real crystal's case of study, the probability of stimulated emission is very small. Furthermore, the majority of the electrons are in the E_1 energy ground state [70], [72]. In fact, thermodynamics Boltzmann's principle predicts that whenever a system in thermal equilibrium at a temperature T, the population at the excited energy level (N_2) in terms of the population at the energy ground state (N_1) and the energy of the two different levels (E_1 and E_2) is [73]

$$N_2 = N_1 \cdot e^{-\frac{E_2 - E_1}{k_B T}} \tag{1}$$

where k_B is the Boltzmann's constant. One can rearrange this equation and substituting $E_2 - E_1$ for the energy of the photon ($\hbar\omega$), obtaining

$$\Delta N \equiv N_1 - N_2 = N_1 \cdot \left(1 - e^{-\frac{\hbar\omega}{k_B T}}\right) (> 1) \tag{2}$$

where ω is the angular frequency, and $\hbar$ is the reduced Planck constant. Thus, it is possible to conclude that in a normal population of atoms there will always be more electrons in the ground state than in the higher energy levels [72]. Meaning that amplification will not be possible because the probability of the absorption of a photon and the probability of spontaneous emission is the same. Consequently, to achieve a laser, a "population inversion" is required to happen [70], [72].

Population inversion of the gain medium occurs once the higher energy state has a greater electronic population than the lower energy state [70], [72]. This kind of event is only possible if one considers more than two energy level in a crystal, and the greater the number of energy states, the greater the optical gain will be. To a better understanding of this concept, let us consider a three energy levels system with energy levels E_1, E_2, E_3, so that $E_1 < E_2 < E_3$, and let N_1, N_2 and N_3 be the number of electrons in its respective energy level (see Figure 9 (a)) [69], [70]. Under normal conditions, a lower energy level will have a greater number of electrons occupying its state. For that reason, it can be concluded that $N_1 > N_2 > N_3$ in normal circumstances [69], [70].

Whenever provided the energy $\Delta E_{1,3} = E_3 - E_1$ to excite the ground state electrons, referred to as pumping, it is possible to achieve a greater population in the third energy state. Such an arrangement is known as "population inversion" (see Figure 9 (b)) [69], [70].

A medium suitable for laser operation has to have the shortest lifetime constant from the third to the second level, transferring the energy of this decay to the crystal lattice by processes without radiation emission [69], [70]. Due to the short lifetime, only a small population of electrons will accumulate in the E_3 energy state (see Figure 9 (c)) [69], [70]. As a result, the population of the E_2 energy state will become, not only greater than the population of the energy states E_3 but also, greater than the population of the E_1 energy state [69], [70]. If this condition is guaranteed and if a photon with a frequency of $\frac{E_2 - E_1}{\hbar}$ is now inserted in the system, an electron in the second energy state level will be stimulated to decay to the first level by stimulated emission (see Figure 9 (d)) [69], [70].

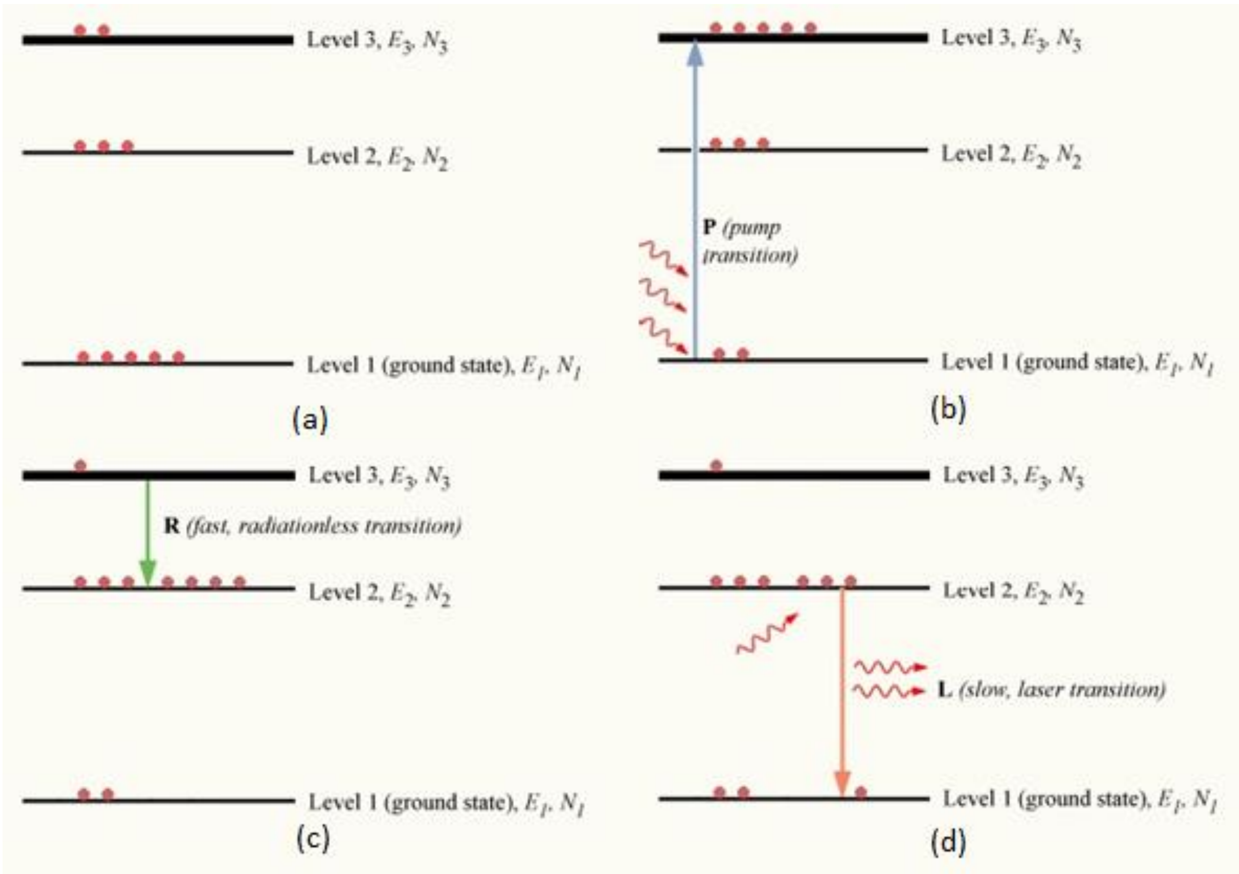

Figure 9. Population Inversion in a 3-level crystal (adapted from reference [74]).

One way to significantly amplify the output signal of this process is via a positive feedback mechanism called optical resonator [72]. An <u>optical resonator</u> is a system of mirrors that reflects undesirable (off-axis) photons out of the system and reflects on-axis photons back into the system [72], [75]. Meaning that emitted photons have an opportunity to stimulate new decays emitting another photon. As the on-axis are reflected back and forth, they will interact, each time, with more excited electrons increasing the stimulated emission [72]. However, to have a laser beam, the optical resonator needs to let a small percentage of the reflected light out of the system. To execute this purpose, one of the mirrors has a considerably lower reflectance, allowing a certain amount of photons getting out of the cavity [72].

Laser systems safety classification

Lasers are devices categorized by their wavelength and for public general usage theirs maximum power has to be limited to make them "eye safe" [76], [77]. For the purpose of most terrestrial LiDAR applications, the laser source makes use of near infrared (NIR) wavelengths [78] because, for long ranges, a better resolution is achieved by providing shorter wavelength light pulses [76]. In this sense, the used infrared wavelengths are those that avoid eye injury. One of the most used wavelengths is 905 nm and it was chosen for early LiDARs because: pulsed diode laser emitters were readily available and relatively inexpensive; silicon detectors could be used to detect the referred wavelength; and also, because the solar spectrum at sea-levels reaches a low irradiance at a wavelength of 905nm . But as this wavelength can penetrate the interior of the eye and reach the retina, the allowed power density is limited. Nevertheless, lasers with a wavelength of 1550 nm are presented as an alternative, as they are absorbed in the cornea instead of the retina [79], which makes them "eye safe" (by the IEC standard 60825-1 [80]) at much higher power levels [76].

The International Electrotechnical Commission, IEC, is an organization responsible for standardization comprising all national electrotechnical committees. In 2001, IEC published the standard 60825-1 regarding laser products' safety that has the intention of:

- Protecting people against hazards from radiation, by reducing injuries from radiation and by introducing a system of classification of laser products and working spaces according to their degree of hazard [80].
- Ensuring adequate warnings of hazard to individuals, by improving the precautions taken into account and through protective safe protocols [80].

Any laser product carries legible, permanent and clearly visible labels in accordance with its class and some self-explanatory cautions. Table 2 presents the laser classes and their functionalities to evidence the risks associated with each laser product class.

Table 2. Brief Summary of the associated risk of each laser product class (adapted from reference [80]).

Laser Product Class	Wavelength Range	Associated Risks
1	-	Safe under reasonably foreseeable conditions of operation.
1M	302,5 nm – 4000 nm	Safe under reasonably foreseeable conditions of operation, but may be hazardous if the user employs optics within the beam
2	400 nm – 700 nm (visible)	The blink reflex may be expected to provide adequate protection under reasonably foreseeable conditions of operation.
2M	400 nm – 700 nm (visible)	The blink reflex may be expected to provide adequate protection under reasonably foreseeable conditions of operation, but it can be compromised if optics are employed within the beam.
3R	302,5 nm – 10^6 nm	Direct intrabeam viewing is potentially hazardous but the risk is lower than for Class 3B lasers. The accessible emission limit is within five times the accessible exposure limit of Class 2 in the wavelength range from 400 nm to 700 nm and within five times the AEL of Class 1 for other wavelengths.
3B	-	Lasers that are normally hazardous when direct intrabeam exposure occurs. Diffuse reflections are normally safe.
4	-	Lasers that are also capable of producing hazardous diffuse reflections. They may cause skin injuries and could constitute a fire hazard. Their use requires extreme caution.

4.1.2. Spatial Resolution of an Optical System

Diffraction is an optical effect in regard to the wave nature of the light that has a great impact in the resolution of an optical system [81]. Spatial resolution is directly connected to angular resolution, because starting by the second one might have a much more intuitive approach: Angular resolution describes the reasonable ability of an image-forming device to distinguish small details of an object [81]. The angular resolution of an optical system can be estimated by the Rayleigh criterion for resolution. If one considers diffraction through a circular aperture, the angular resolution θ in radians is [82]

$$\theta = 1.220\,\frac{\lambda}{D}\,[rad] \tag{3}$$

where λ is the light's wavelength and D is the diameter of the output aperture [83].

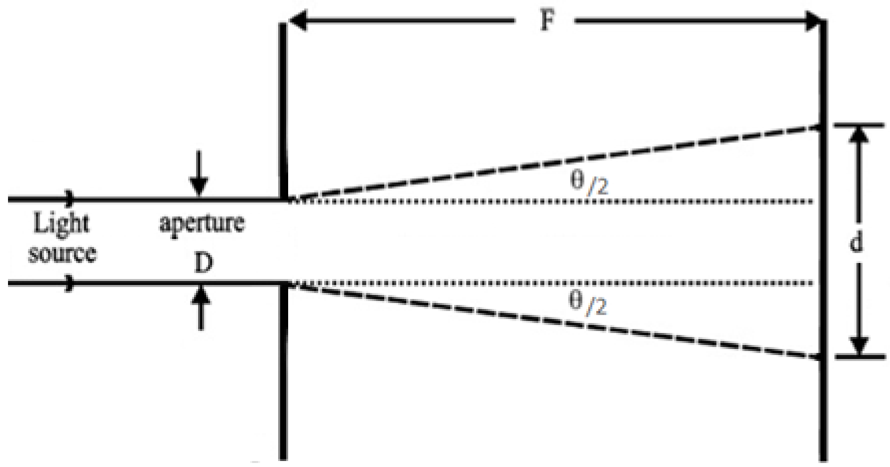

Figure 10. Diffraction limit of a Camera [adapted from reference [84]*].*

Hence, the minimum achievable spatial resolution in a given direction, d, at a distance F from the outer aperture is

$$d = D + 2F\tan\left(\frac{\theta}{2}\right) \tag{4}$$

In terms of LiDARs and radars, the diameter of the outer aperture is usually neglected. Since LiDARs usually use much shorter wavelengths than radars (near infrared versus radio waves), its angular resolution will also be significantly shorter leading to the LiDARs' better spatial resolution. Imperfections in lenses, misalignments and weather conditions are some other factors that also affect the resolution [81].

The weather condition greatly affects LiDARs resolution due to the unavoidable light scattering phenomena that droplets inflict. The relation between the particles' size and the LiDAR's wavelength (905nm or 1550nm) allow to conclude that two main phenomena can occur: Rayleigh scattering (particles' dimensions $\ll \lambda$) and Mie scattering (particles' dimensions are from the same magnitude λ or even greater) [85]. For that reason, Rayleigh scattering is usually considered as the main source of scattering in fog-like conditions. Furthermore, the Mie scattering is usually considered in rainy-like conditions [85]. As droplets' size continue increasing, the distribution becomes more pointed in the forward direction and only a part of the light is transmitted, deteriorating LiDAR's resolution [85].

4.1.3. Receiver Electronics

Photodetectors are the devices that are responsible for reading and recording the light signal backscattered from the object in analysis [76], [86]. In addition, in some optical systems, time resolution is needed. To this type of system, it is implemented Time-Correlated Single Photon Counting (TCSPC) as a solution [87], [88]. TCSPC is a digital counting technique for, as its name says, counting photons that are time correlated in relation to a short excitation light pulse [89]. The periodic excitation, from a light source of high pulsed repetition rate, allows extending the data collection and building a digital signal that represents the optical flux [87]–[89]. This extremely time-precise method [90] is an extraordinary technique for recording low-level light signals with picosecond precision. It consists of repetitively record an input signal, in relation to a reference signal. This is achieved by the generation of multiple START, usually a signal similar to the optical output signal, and STOP pulses, which are typically the signal that reaches the detector [87]–[89]. The reverse case is also a possible way to process TCSPC [89], [90].

The reverse mode has a clear advantage at high rates of the light source: Because some objects might be further away than the path done by the light between START pulses, the TAC (Time-to-Amplitude Converter) might have some START signals which are never stopped by a STOP signal, leading the system to execute a reset at overflow [89], [90]. In this process, electronics of the system are kept busy for at least 20 times the amount of needed time [90]. The full system capability is used in the reverse mode of TCSPC, where the high rate signal is connected to the STOP input and the lower rate signal (the traveling signal) is connected with the START input [90]. Another advantage of using the reverse mode is that one can use a delay box and adapt the delay added to the reference so that the pulse-to-pulse jitter time is minimum. The disadvantage of this kind of system is that an external system is needed for the reference signals to be delayed and to arrive later then the START signal [90].

As the technique requires a single photon to be detected, a sensor capable of detecting a single-photon must be used. To reach this goal, the detectors that can be used are Photomultiplier Tubes (PMT), Micro Channel Plates (MCP), Single Photon Avalanche Diodes (SPAD) or Hybrid PMTs [87].

4.1.4. Detectors

As mentioned previously, detectors for a type of technique like TCSPC must have a sufficiently high gain to produce a measurable electrical pulse for a single detected photon [87], [89]. The electrical signal must be short so that it is possible to resolve individual photons at a high-count rate. For that to happen, the translation of the optical signal into an electrical one must be as fast as possible [87], [89]. The detectors introduced in section 4.1.3, i.e. PMT, MCP, SPAD, and Hybrid PMT; usually meet these requirements, but they are still far from ideal. In the scope of obtaining the best possible results from a TCSPC experiment, one must understand the typical performance and possible side effects of these detectors.

<u>Photomultiplier Tube - PMT</u>

A photomultiplier tube is a device that contains a photocathode, an electron multiplier and an anode inside of a glass housing where vacuum is made (see Figure 11) [89], [91]. The electron multiplier consists of several electrodes, called dynodes, that are held at a positive potential, each one at a greater voltage state than its precedent [89], [92]. In this scheme, whenever an electron hits the first dynode, multiple photons are released, making an overall gain reaching values of 10^6-10^8 in a few nanoseconds [89], [91]–[93]. This principle is known as the secondary emission [89], [91]–[93].

As one can see in Figure 11, incident photons strike the photoelectric element (the photocathode) and, due to the photoelectric effect, electrons are ejected from this surface [89], [91]–[93]. The arising electrons are now reoriented, by the focusing cathode, and accelerated, due to the electrical field generated by the voltage source between the photocathode and the anode, towards the first dynode up until the end of the electron multiplier, reaching the anode [89], [91]–[93].

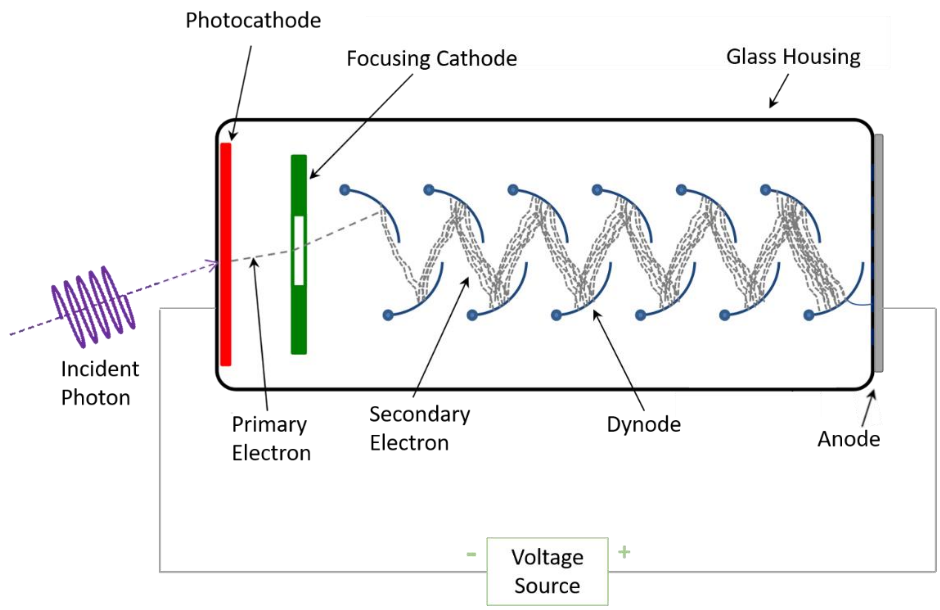

Figure 11. Schematic of a photomultiplier tube (adapted from reference [94]*).*

A huge drawback of a photomultiplier tube is that the first emission of electrons is originated from a photocathode, so its primary step of detection is by the external photo effect principle, meaning that electrons are emitted in all directions [89], [95]. They also are substantially large and require high voltages to be operated. Since electrons can be emitted back to the photocathode the quantum efficiency, i.e. the probability that a photon releases an electron, is smaller than 50% [89], [95].

Microchannel Plate - MCP

A Microchannel Plate is a detector closely related to the electron multiplier because it also amplifies a single-photon signal by the secondary emission principle [89], [96], [97]. This sensor consists in one or more plates containing a large number of small channels (4 to $25\ \mu m$ of diameter [87], [98]) within themselves. A high voltage is applied along with them, so that the capillaries walls, made of an electron-emissive material, work as secondary emitters (see Figure 12.a)) [89], [96], [97]. Two or three microchannel plates can be arranged in series for that one can obtain a higher gain. Due to the small deviation that the electrons have from the propagation line in this kind of system, the transit time can be as short as 25 picoseconds [87]. If one has a necessity of position sensitivity, the anode can be replaced by an array of smaller anodes that individually will detect pulses (see Figure 12.b)) [89], [96], [97].

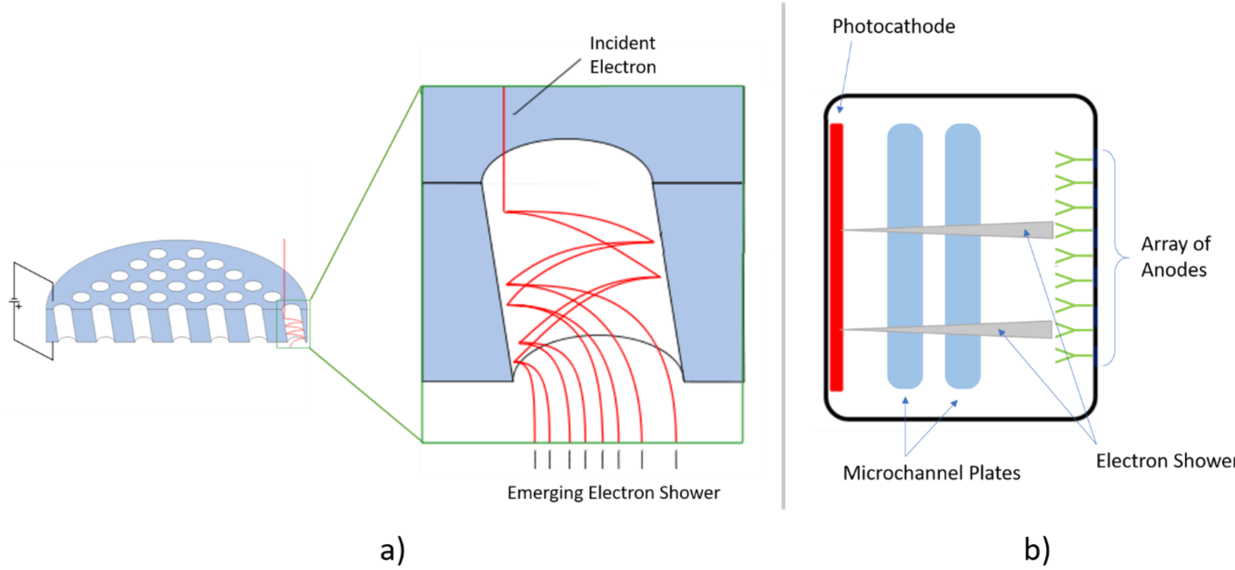

Figure 12. Schematic of a) a microchannel plate (adapted from reference [99]*) and b) and MCP system of 2 plates sensitive to position.*

<u>Single Photon Avalanche Diode - SPAD</u>

An avalanche photodiode (APD) is a semiconductor-based photodetector (photodiode) [65], [89], [100], [101]. In photodiodes, a high electrical field is responsible for, whenever a photon interacts with the semiconductor, creating an electron-hole pair, separating the electrons and holes, to generate a current through the device [65], [89], [100], [101]. The operation principle of a single-photon avalanche diode can be observed in Figure 13. The current produced by one electron-hole pair is not enough to be recorded directly, and the photon presence can only be detected if the semiconductor has an internal gain that does not introduce thermal noise. This kind of behaviour, called the "Avalanche Effect" [65], [89], [100], [101], occurs, whenever a photodiode is operated at a high reversed voltage, close to the device's breakdown voltage, causing the moving carriers to free new electron-hole pairs from the semiconductor lattice [65], [89], [100], [101].

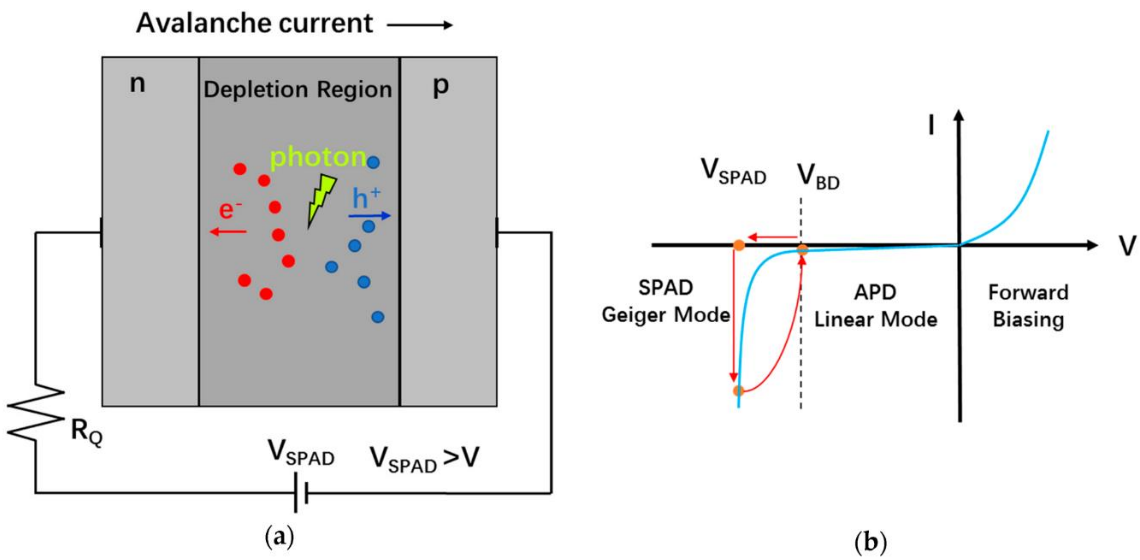

Figure 13. Single-photon avalanche diode operation principle: (a) Avalanche breakdown process in a reverse biased p-n junction; (b) I-V characteristic curve of a SPAD device (adapted from reference [102]*).*

This effect, used in standard APDs, is still not enough to allow the detection of a single photon with the time resolution required for TCSPC, forcing it to have higher gains, resulting in instability, and also could cause the photodiode to collapse [89], [100], [101]. To avoid the collapse and to have greater gains, the reverse voltage is set several volts above the breakdown voltage, and a quenching circuit is added, to restore the normal operation to the semiconductor, after each photon detection. This is known as the Geiger mode and it is the principle behind a single-photon avalanche photodiode (SPAD) [89], [100], that allows it to reach gain values of 10^8 [101]. The quenching mode can be active or passive (see Figure 14) and the one to be used must be selected considering the count rate and efficiency [89], [100], [101].

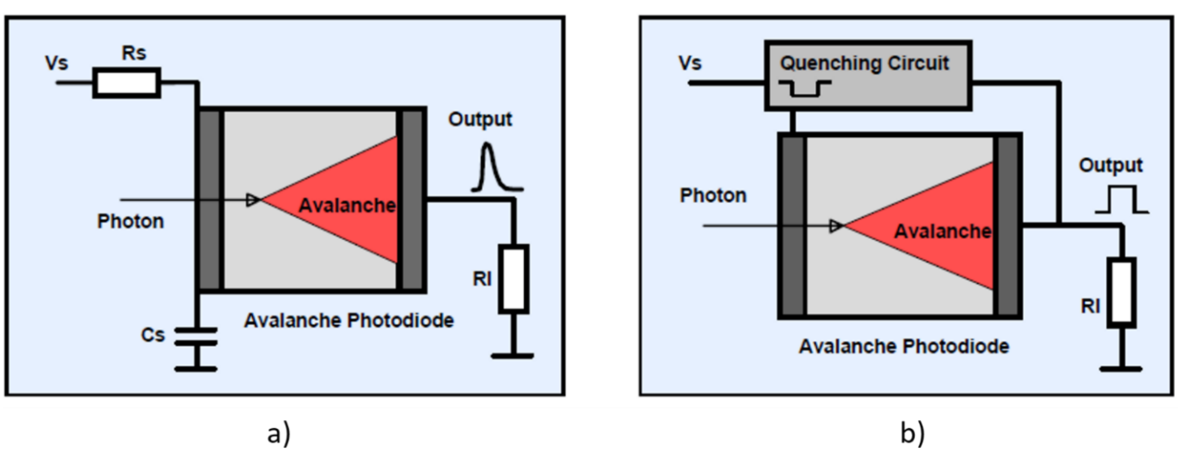

Figure 14. Quenching systems for SPAD devices: a) Passive quenching; b) Active quenching (from reference [89]*).*

The Single Photon Avalanche Diode is capable of detecting a single photon up to 50% of probability with 0.8 of quantum efficiency and a time accuracy of down to 30 picoseconds [87].

Hybrid Photomultiplier Tube

Hybrid PMTs are vacuum tubes integrated with photocathodes and avalanche diodes [89], [103], [104]. A scheme of a hybrid photomultiplier tube is represented in

Figure 15. As in PMTs, whenever a photon is absorbed by the photocathode, there will be electrons emitted and accelerated by a high electrical field to the semiconductor avalanche diode [89], [103], [104]. By taking this type of approach, one first obtains an electron-bombardment gain and afterward an avalanche gain [89], [103], [104]. The combination of these two technologies offers beneficial features like a high speed, a high pulse height resolution, a time uncertainty on the order of $50 - 100\, ps$, small latency and, in addition, it allows to develop a compact device [87], [89], [103], [104].

One can understand that this process's gain is obtained in one step, which means that they will deliver single-photon narrow pulses, allowing them to distinguish one or multiple detected photons [89], [103], [104]. More than that, the absence of an electron multiplication system made it possible to successfully not having electrons getting neither absorbed nor reflected [89], [103], [104]. The major advantage of this detector is that there is no afterpulsing in its measures [89], [103], [104]. The afterpulsing are the background pulses that appear a few milliseconds after the detection of a photon in the detected signal [89]. It is a phenomena believed to be caused by ion feedback, by luminescence of the dynode material, by the glass of the PMT or by the electrons and holes in the previous avalanches of SPADs [89].

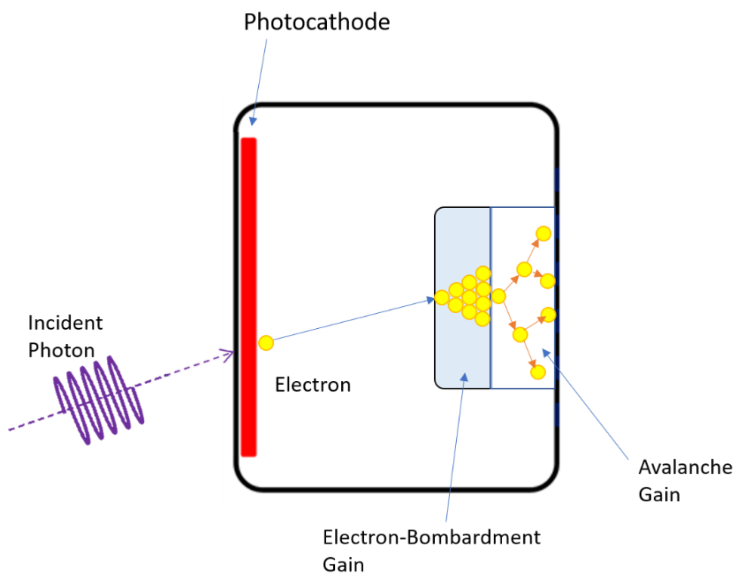

Figure 15. Schematic of a Hybrid Photomultiplier Tube.

4.1.5. Scanning system

The scanning mechanism is conceived to consistently steer laser pulses in order illuminate surroundings with laser light and to measure the reflected pulses [78]. There are different methods of scanning the scenery available, granted for different purposes, such is achieved by regulating the azimuth and elevations, dual-axis scanner, dual oscillating plane mirrors and polygonal mirrors [77]. It is important to note that this system will determine the range and resolution of the device, but the speed at which images can be built up will be affected by the speed of scanning [77].

In 3D scanning, the scanning mechanisms are the systems responsible to direct laser beams with a range finder within the FoV. By taking the distance measured in various directions and from different viewing angles the device is able to capture the surroundings point cloud. The scanning systems available are presented in Figure 16. The following subsections briefly summarize some of them.

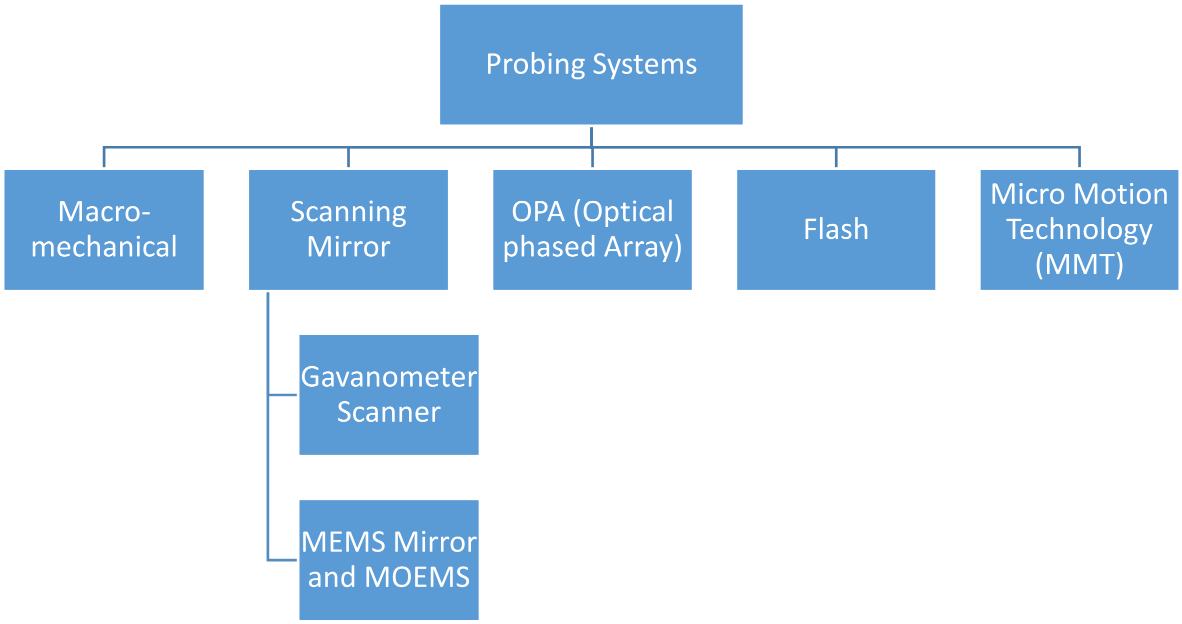

Figure 16. Probing Systems for 3D LiDAR.

Mechanical Macro-Scanners

Mechanical scanner systems are rotating systems that, in order to cover a 360° horizontal FoV, rotate their fixed laser-receiver assemblies around their vertical axis [105], [106]. Meaning this that each frame is obtained by completing a turn. That is, the point cloud density is placed vertically and the horizontal is a function of the rotation speed (see Figure 17). The vertical scanning of this kind of systems is achieved by aligning multiple laser-receiver assemblies covering different angular directions, meaning this, that vertically the resolution and point density are established by the used number of laser-receiver assemblies and the angular spacing between them.

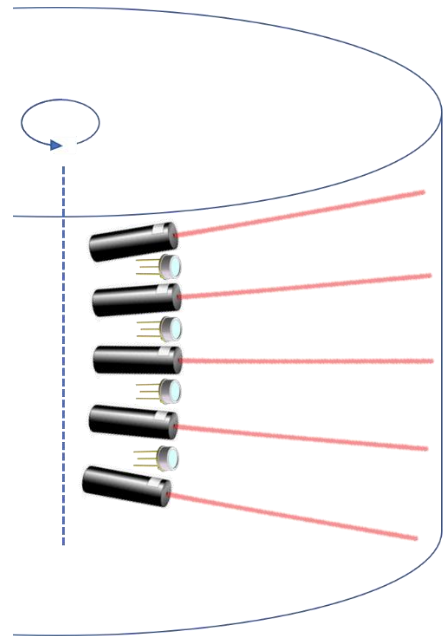

Figure 17. Representative scheme of a Mechanical Scanning System

Due to the simple scientific background, it is easy to control and predict the behaviour of mechanical macro-scanners [105]. Thanks to these characteristics, these systems are usually used to make the minimum viable LiDAR product [105]. For this reason, mechanical scanning might be the most used scanning system. As an example, one of the most used mechanical macro-scanner LiDARs is Velodyne with Alpha Prime™ LiDAR (see reference [107]).

Note that this kind of mechanism is the only one to be presented that is not a steering beam scanner, meaning this is the only system that does not use optical elements to control the beam vertically and horizontally.

<u>Scanning mirrors</u>

The majority of beam steering scanners use moveable mirrors to direct the light beam. In a system using scanning mirrors, a stationary laser beam is controlled through an optical system of lens and mirrors to redirect the light beam. One of these mirror systems is the galvanometers scanner represented in Figure 18.

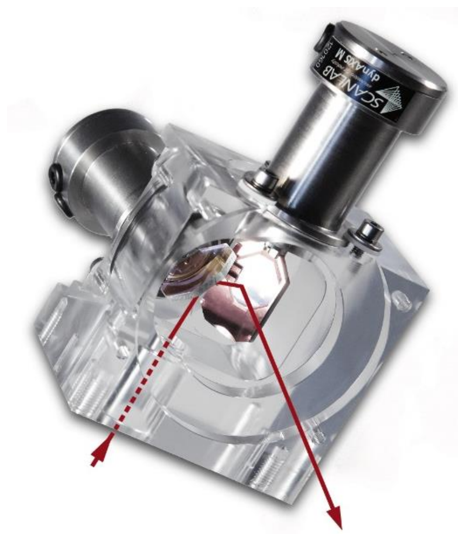

Figure 18. Galvanometer Module from SCANLAB AG. From reference [108].

A Galvanometer Scanner, also called Galvo, is a system that consists of galvanometers, mirrors and a controller to regulate the system [109]. A Galvo uses at least 2 galvanometer mirrors in order to capture the vertical and horizontal dimensions of the FoV. Galvanometer mirrors are electromechanical devices constituted by a galvanometer and a mirror, combined to deflect the light whenever an electric current is sensed [110].

Galvanometer scanners are widely used in laser scanning because the provide the easiest way of steering a laser beam [111] and also for its incredible accuracy and precision [110]. However, the simplicity of making the beam travel across the FoV is, accompanied by the bulkiness of the system [111], and it might probably be the architecture most affected by the car movements and vibrations.

<u>Microelectromechanical System - MEMS Mirror</u>

Another way of realizing a scanning mirror apparatus is by using a micro scanning mirror, which is a more compact, lighter and lower power consumption way of steering a light beam. A MEMS mirror (see Figure 19) can be made, depending on the MEMS morphology, either by translation or rotation, on one or two axes, by electrically derived from repulsive force actuators [112].

This type of system also has some downfalls as, for example, the efforts made to align it are much intricate, the FoV is limited by the mirror's maximum deflection and the resolution of the system depends on the minimum measurable quantity variation of the mirror controller electrical signal. Modern LiDAR systems for the automotive industry are using MEMS mirrors that operate by being controlled by a system called MEMS Driver [113].

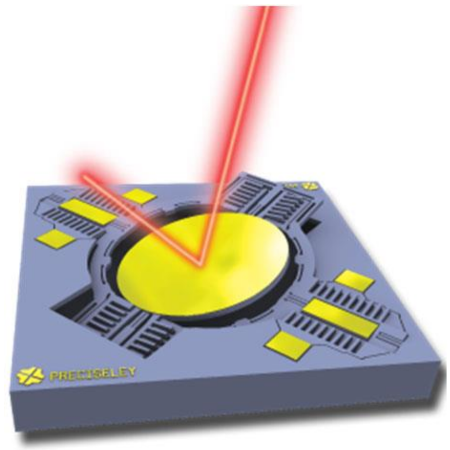

Figure 19. MEMS scanning mirror of Preciseley Microtechnology Corp (from reference [114]*).*

A scanning MOEMS (Micro-opto-electro-mechanical system), or scanning optical MEMS, is a special class of a MEMS and it is a combination of a MEMS with micro-optical elements [115].

<u>Solid-State probing</u>

There are two types of solid-state probing systems: The Optical Phased Array (OPA) and the Flash technique.

Using the OPA beam steering technique, the beam is precisely steered without any moving part [116], [117]. This device is used for aiming laser beams on a macroscopic scale by firstly splitting the light source's beam through a power splitter tree, followed by aiming each segment of the light to a phase shifter, and lastly adjusting the phase of light waves, reflected or transmitted, through a surface of phase modulator crystals, called the array [116], [117]. The wavefront of the combined elements will then have the desired shape and direction of propagation and, consequently, redirecting the laser beam in a desire direction [116], [117]. Some examples of the referred capability of this method are represented in Figure 20.

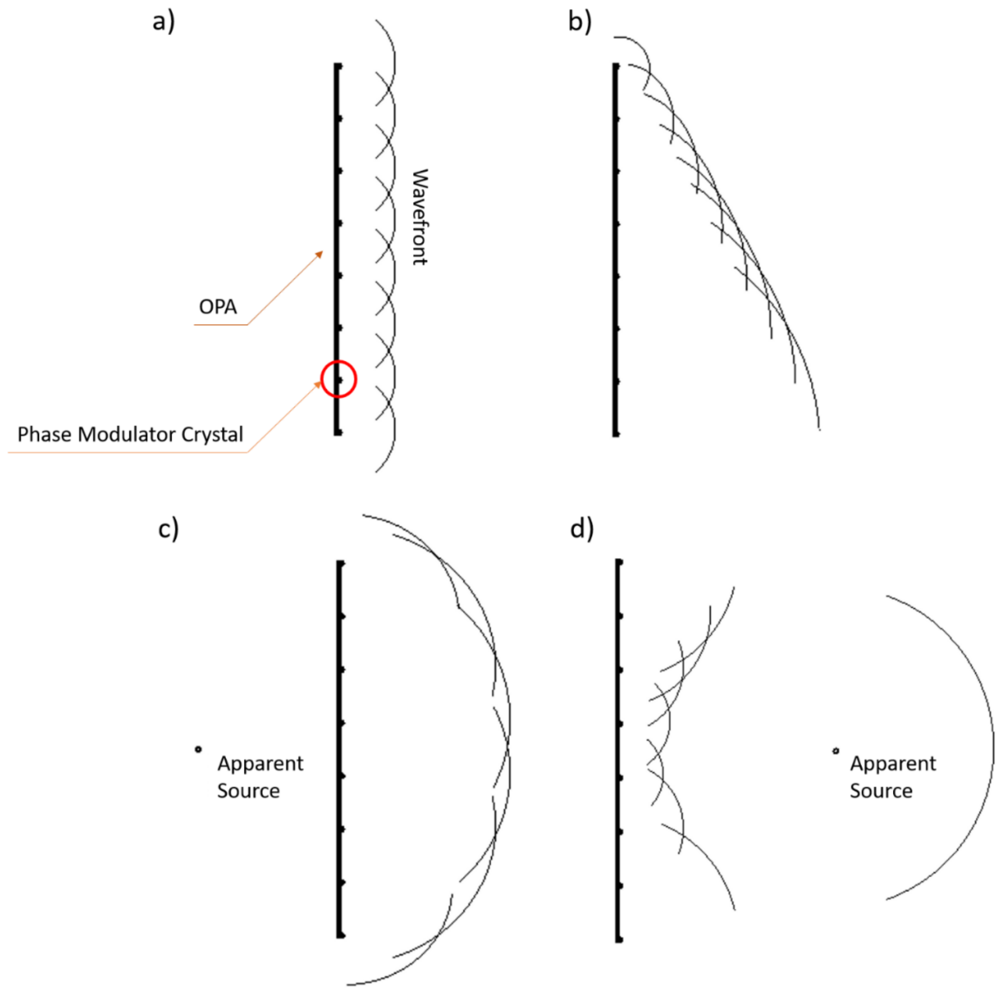

Figure 20. Waves emanating from discrete sources in a phased array interfere to create a) a plane wave that appears to come from a distant source behind the array; b) a plane wave that propagates at an angles from the array surface; c) a spherical wave that appears to come from a point behind the array surface; d) a wavefront that appear to originate in empty space in front of the array (Adapted from reference [118]*).*

Furthermore, a Flash probing technique uses a single light source that illuminates the entire FoV in a single pulse that will posteriorly be detected by a 2D array of detectors. Each pixel of the 2D array detects the time it takes each laser pulse to hit the target and return to the sensor, as well as the location and intensity of the reflected pulse [119], [120]. The returned signal is processed by embedded algorithms to generate the fastest way to create a 3D rendered image of the FoV of the sensor [120]. One can understand that this is a high accuracy tool for applications in highly precise real-time imaging [121]. Figure 21 compares a beam steering scanner and a the briefly presented flash scanner in order to illustrate their differences.

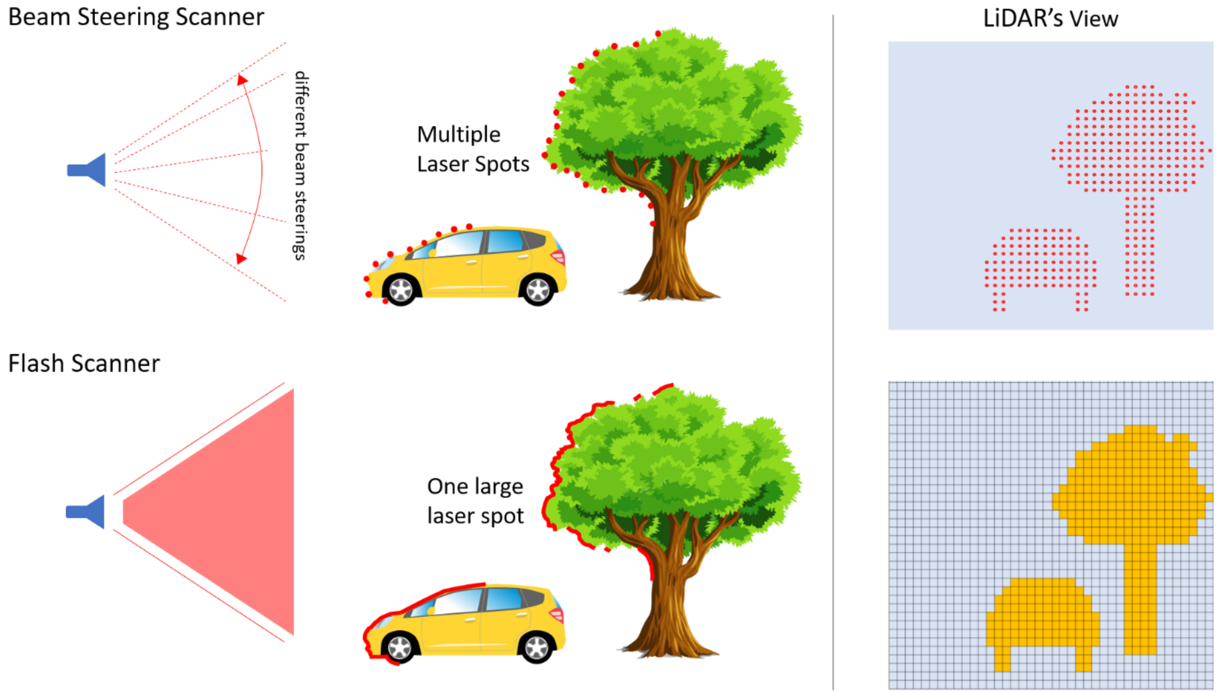

Figure 21. Comparative scheme of a Beam Steering Scanner and a Flash LiDAR.

<u>Micro Motion Technology - MMT</u>

The US start-up company *Cepton* patented Micro Motion Technology (MMT) in 2016 [122]. This technology is supposed to minimize the use of mechanical components making the system frictionless[123], which translates into reducing costs and increasing reliability [124], [125]. At present, it is not exactly known how the MMT system works but it is said that it allows smalls movements of the laser sources and the detectors by making the use of coils [124], [125].

5. State of The Art

It is suggested to consider that this research was made in February 2020 and because the automotive market is such a ferocious demand, new products and improvements are constantly being brought to the public eye.

Also, one must consider that there are more marketplaces to LiDAR than automotive, such as agriculture, urban planning, astronomy, pollution modelling and meteorology, species conservation management, geology and mining, and green energy safety management [126].

5.1. Automotive LiDARs

The majority of the global market players are located in North America's Continent, more specifically in countries like the United States of America and Canada, being the first, the one with either the most promising start-ups and either the most established veteran companies [127]. European countries like Germany, Sweden, United Kingdom and Austria; along with Canada, Israel, and Japan; are constantly making significant progresses[127], [128]. Moreover, although China and Korea are in preliminary stages of LiDAR production and R&D, they are blooming, and they are expected to have a great contribution in this sector [127].

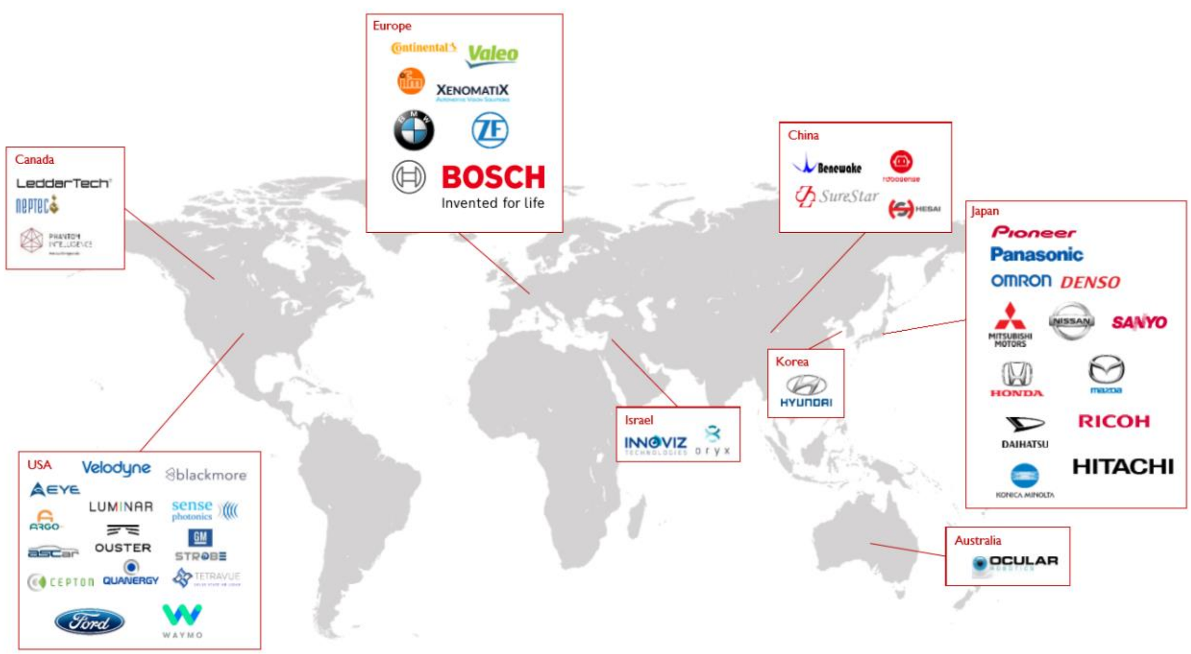

Figure 22. Global automotive LiDAR Manufacturers (adapted from reference [129]*).*

On August 14th, 2019, the International Society for Optics and Photonics (SPIE) published a proceedings paper in recent developments of automotive LiDAR technology, its industry and trends. This study also identifies OEMs tech companies, suppliers and manufacturers of the necessary components, such as illumination sources, photodetectors, and optical elements integrated circuits [127]. Following this report jointly with more up to date LiDAR's news, potential products to autonomous driving were selected to serve as an object of study and the results are discussed below. To this purpose, the main comparison criteria were the technology, range, horizontal and vertical FoV, angular resolution and range resolution.

Due to different technologies have been implemented in different products, a complete comparison is limited and not viable. For this reason, an attempt was made to approach all the technological implementations referred to in chapter 4 "The context of LiDAR".

5.1.1. Comparison of Automotive Current Products

In this section, some of the automotive first front company's best products are compared. The companies that are going to be the object of study in this state of the art are Velodyne, Ouster, Innoviz, Aeye, Omron, Quanergy, Cepton and LeddarTech. In Table 3, an attempt was made to do a summary of some of the best LiDARS, approaching multiple wavelengths and all the scanning technologies. Due to the diversity of the technologies being implemented in prototypes and commercial LIDARs targeted for automotive applications, a complete comprehensive (of all the possible LIDARs) is not viable. For this reason, the referred table criteria selected to analyse the presented products were wavelength, technology, range, horizontal and vertical FoV, angular resolution and range resolution.

Bearing in mind the evaluation done in Table 3 of some of the best current products, Velodyne is still leading the mechanical LiDAR market with Alpha Prime™, in terms of performance. Its 128 channels allow high-speed support for autonomous driving, but this product still is not available to mass production. In addition, Velodyne advanced in "CES2020" , organized by the Consumer Technology Association, that the company was ready to start mass production of their other products such as Velarray™ and Velabit™ [130]. The latest is the most recent announced product but there is not yet any information about the working principle of the device beyond working with metamaterials. Moreover, Velodyne informed that Velabit™ is able to work with cheap electrical components [131]. For this reason, the company promised that this LiDAR will be sold for less than 100 US dollars [132].

Table 3. Comparison of some first front company's current automotive LiDARs.

Company	Product	Wavelength [nm]	Technology	Range [m]	Horizontal FoV [°]	Vertical FoV [°]	Horizontal Angular Resolution [°]	Vertical Angular Resolution [°]
Velodyne	Alpha Prime™	903	Mechanical (128 CH)	300	360	40	0.2	0.1
Ouster	OS-2	-	Mechanical (64 CH)	200	360	15.8	0.18	0.12
Innoviz	InnovizOne	905	MEMS	250	115	25	0.1	0.1
Valeo	Valeo SCALA®		MEMS	200	145	-	0.8	-
Aeye	AE100	1550	MOEMS	200	60	30	0.1	0.1
LeddarTech	Leddar Pixell	905	Flash	41	177.5	16.0	-	-
Omron	3D-LiDAR For long range	-	Flash	150	140	14.4	0.5	0.5
Quanergy	S3	-	OPA	180	120	10	0.5	0.5
Velodyne	Velarray™	-	"Frictionless Mechanism" (32CH)	200	120	35	-	-
Cepton	Vista-X120	905	MMT (120 Lines)	200	120	-	0.15	-
Velodyne	Velabit™	903	Metamaterial	100	60	10	-	-

The high resolution LiDAR Vista-X120 from Cepton is also a product that has kept some attention for itself, not only for its price point in the hundreds of dollars once in mass production, but also for its rugged, durable and reliable MMT technology that is also a well-kept secret [124].

5.2. Polarization in remote sensing

A fundamental principle of light is that the electric field vector, $\vec{E}$, of the electromagnetic wave can exhibit some orientation dependence either in time or space. This phenomenon is called polarization. The polarization content of light beams can be grouped in elliptical polarized light (with special cases being linear and circular polarized) and non-polarized contributions. Essentially, these names are derived from the shape of the electric field that oscillates normal to the direction of light propagation. To see this type of shapes, one might either consider a time-moment and move through space, considering one point of the light path and move through time.

Unpolarized light should also be considered, which is essentially when a light beam randomly varies polarized waves and it is not possible to describe a time nor spatial dependence of the electrical field. In addition, partially polarized light is defined as a combination of fully polarized and unpolarized light, where some polarization states are more likely than others.

The use of polarization in remote sensing is a well settled concept in the literature [133], [134].

Polarimetry is vastly used as a remote sensing technique that provides information, largely uncorrelated with spectral and intensity images, that allows enhanced contrast in intensity images with little to no contrast [135]. This technique is used in a wide range of applications like atmospheric remote sensing, target detection, astronomy, biomedical application,...[136] Figure 23 is a representative example of the use of polarization to enhance target detection. In this example, two pickup trucks in the trees can be detected by using polarimetric techniques.

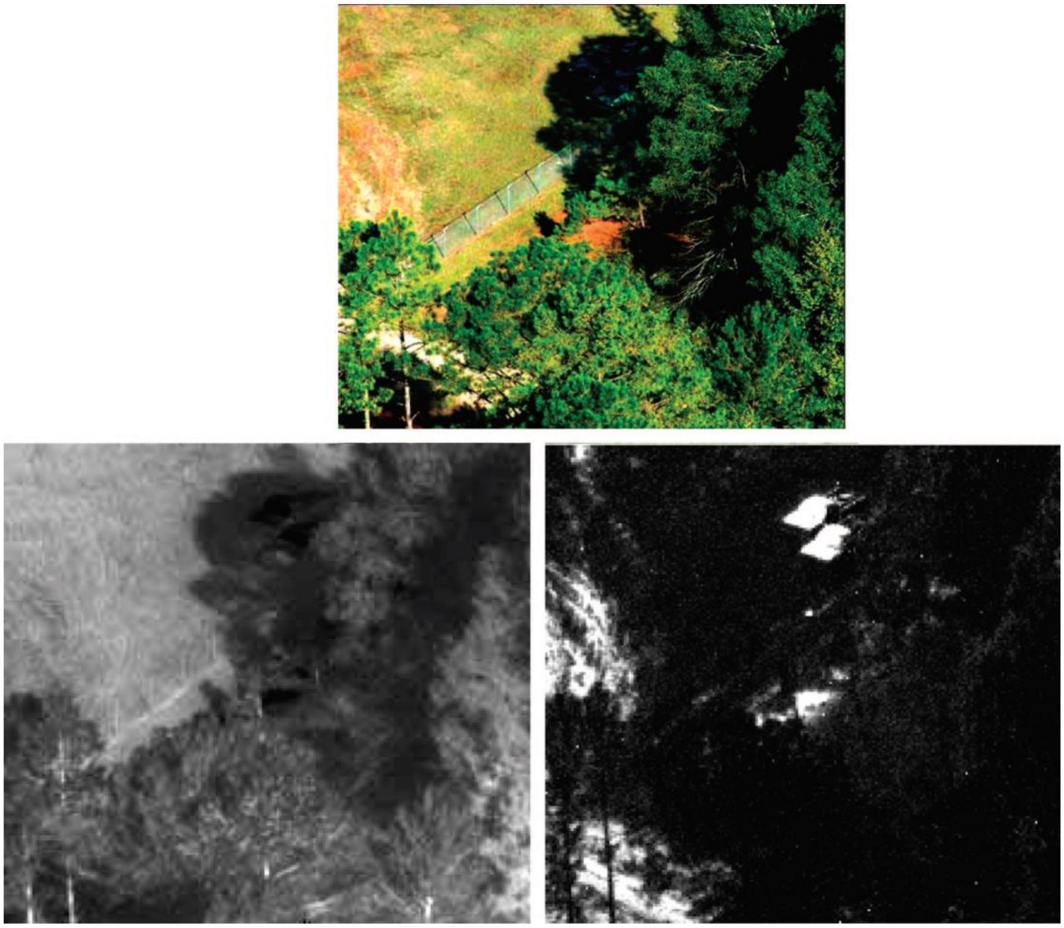

Figure 23. (Visible picture of two pickup trucks in the trees' shade (top), long-wave IR intensity image (bottom left), and long-wave IR polarization image (bottom right). Strong contrast in the polarization image shows advantages for enhanced target detection using imaging polarimetry. From reference [135].

Measuring the polarization response has been used vastly in remote sensing and it is clear that it can be advantageous in many fields of the optical metrology, providing additional information about a wide range of sources and objects, that can be exploited to better distinguish between targets.

Therefore section 5.2.1 presents multiple LiDARs which exploits polarization as a metrology technique.

5.2.1. Polarization LiDARs

In this section, the state-of-the-art of the use of polarization in LiDAR is illustrated. Note that, although polarization LiDARs exist, their use in autonomous driving to recognize objects is innovative and it has never been done. For this reason, in this section, the summarized applications are not related to autonomous vehicles.

Atmospheric study using a Polarization LiDAR

Leibniz Institute for Tropospheric Research published a research (see references [137], [138]) that studied the concept of depolarization to distinguish aerosol particles and dust. In this study, they have observed, by using a LiDAR, that differently shaped particles will interact with polarized light differently [137], [138]. A LiDAR representation of the one used in this research is presented in Figure 24.

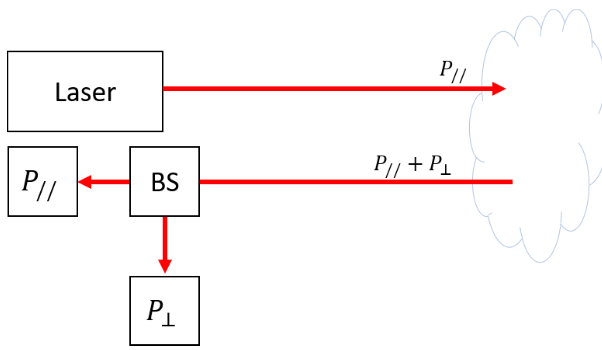

Figure 24. Schematic representation of the LiDAR system used in the study of reference [137]. $P_{\perp}$ *and* $P_{//}$ *are the perpendicular and parallel linear polarization states with respect to the emitted light, respectively, and BS stands for Beam Splitter.*

Their proposal is to use a LiDAR that emits linearly polarized light into the atmosphere, where it interacts with atmosphere particles [137]. The emitted light is then backscattered and, once it arrives at the LiDAR, it is separated into two different channels with crossed polarization states (horizontal and vertical polarization states, see Figure 24) [137]. By doing this, it is possible to determine the degree of depolarization made by the interaction with the particles in the atmosphere and so, to determine the presence of aerosol droplets and dust [139]. This study is sustained by spherical particles do not change the state of polarization in the single scattering regime, whereas non-spherical particles cause depolarization in the backscattered light via multiple internal reflections [137], [139].

Ultraviolet (UV) Polarization LiDAR for remote sensing of new particles forming in the troposphere

A key factor of air quality and climate change previsions is the accurate observation of nucleation events. So, the understanding of new particles development in the atmosphere is critical [140]. Nanometer-sized particles, named ultrafine particles, are mainly the cause of new particle formation [141], and to the recognition of those, a 355 nm-wavelength Polarization LiDAR was proposed [140]. The UV Polarization LiDAR described in reference [140] can remotely observe new particles formation events, promoted by dust particles or volcanic ash particles, while it also provides a range resolved visualization [140]. Likewise, the LiDAR apparatus proposed, enables to see the threshold at which dust starts to promote nucleation [140].

The CALIPSO mission: Spaceborne lidar for observation of aerosols and clouds

The CALIPSO mission is a collaboration developed between NASA and CNES that aims to provide information and improve the understanding of aerosols and clouds in the Earth's climate system [142]. CALIPSO satellite uses passive imagers in the visible and infrared spectral regions and an active LiDAR to profile vertically clouds and aerosols and their properties [142]. The satellite consists of a two-wavelength polarization sensitive LiDAR that qualitatively classify aerosol sizes via the wavelength dependence of the backscattered light and provide information on the vertical distribution of cloud ice/water phase through polarization (via the ratio of signals in two orthogonal polarization channels) [142].

The CALIPSO mission consists in combining data from the CALIPSO satellite and other two satellites, to allow fundamental understanding of the links between aerosols, clouds, and radiation, which are needed to accurately assess future climate changes [142].

Polarization modulation in LiDARs

This section presents two different types of systems that implement polarization modulation. Although the two systems perform polarization modulation, the first system is already available in the current market and it implements this concept in the detection to predict the distance of the illuminated targets, while the second system is yet in an investigation stage and it implements polarization modulation to distinguishing different materials from each other.

- *TetraVue's method for 3d imaging systems: The US8471895B2* [143] and US20170248796A1 [144] patents in Flash LiDAR

TetraVue is an innovative company that patented the concept of encoding distances to targets through polarization in flash Laser Imaging and Ranging Systems (LIMARS). This patent was registered in 1992 and it states that reading the income signal, that passes by a Pockels cell, with conventional camera sensors, the targets' distance are decoded [143], [145]. This concept is considered to be the basis of the distance determination of its current product: 4D Solid State Flash LIDAR Video Cameras.

The use of a modulator (like a Pockels cell), to encode the range of a target by ways of intensity changes, removes the need of expensive and complex circuitry. Meaning that, instead of using expensive high sensitive light sensors, it uses more conventional sensors [143], [145].

Since 2017, TetraVue has the property right of the patent US20170248796A1 [144], where the principle of using polarization to estimate distances is maintained. This newer patent seems to keep the same methodology but, instead of using a polarizing beam splitter (to project two different polarization states) and two detectors, it uses only one focal plane array that is aligned with a polarizing grid [144], [145], making the system simpler, cheaper, less bulky and less complex to manufacture and calibrate [145].

- Single-Pulse Mueller Matrix LiDAR Polarimeter: Modelling and Demonstration

A new LiDAR polarimeter architecture, capable of determining a target Mueller Matrix in a single laser pulse, was introduced by the authors in reference [146]. Since Mueller polarimeters allow to measure polarimetric material properties, and thus, material detection, classification and analysis [139], [141], [147], there has been an attempt of integrating Mueller's principle into active sensing. Nevertheless, the measure of the Mueller matrix often results in a measurement duration of seconds to minutes depending on the polarimeter design [146]. For that reason, recent work has extended LiDARs to measuring the full Mueller matrix. The main idea is to measure the Mueller matrix of samples in one pulse, in order to implement Mueller polarimetry into moving remote sensing. The definition of the Mueller matrix, as well as its polarimetric measurement principle are described in chapter 6.

In reference [146], an incomplete Mueller polarimeter (able to measure Mueller matrix elements) combined with a LiDAR is presented. A pulsed laser is directly pointed to a polarization state generator (PSG), formed by a linear polarizer and an electrooptic crystal, that causes a variation in the polarization along with the temporal distribution of the emitted laser pulse (see Figure 25). As the pulse propagates inside the PSG, the electrooptic crystal varies its birefringence which induces a variation in the polarization along with the temporal distribution of the emitted laser pulse [146]. The temporal distribution of the polarization state is controlled by applying a time-varying voltage to a voltage controller of the electrooptic phase modulator [146]. The tested configuration was developed to only measure nine out of the sixteen Mueller matrix elements, and so, as for the transmitter, four light detectors were used, each one analysing a different polarization state [146]. A simplified experimental layout was drawn in Figure 25. The architecture proposed in reference [146] enables the whole processing in some nanoseconds with a ≤ 8% error.

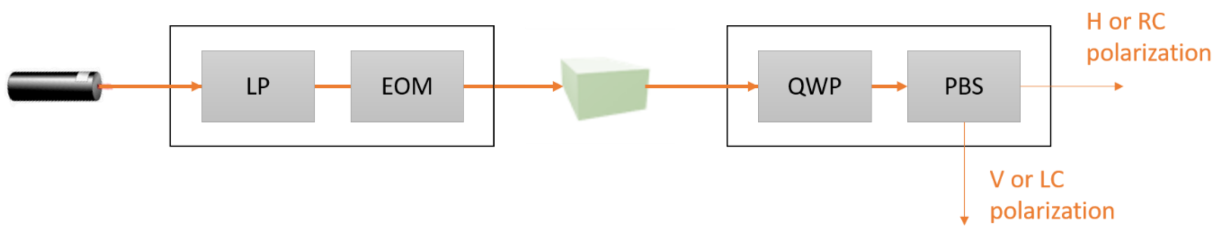

Figure 25. Tested demonstrator layout. LP- Linear polarizer, EOM- electro-optic modulator, QWP – quarter wave plate, PBS -polarizing beam splitter.

In this chapter, some of the most recent state-of-the-art was presented and, although lots of LiDARs are being produced to reach the automobile market, there is still no proposal of an automotive LiDAR including a material detection and classification via the use of the Mueller matrix elements. Moreover, the Stokes-Mueller formalism has been multiple times used in the sense of discriminating different materials (see references [139], [141], [147]).

Based on the idea that a polarimetric LiDAR, able to measure the Mueller matrix, can be used for autonomous driving, this master thesis is focus on characterizing the most relevant road scene objects and designing a polarimetric LiDAR, in order to bridge these elements. In addition, from the different applications discussed in this chapter, polarization has shown great results in remote sensing, enhancing the obtained results.

6. The Concept of Polarization

To understand the study of polarization and its interaction with matter, one must start to consider the wavelike properties of light. This will be the case where the electric and magnetic fields, that describe light, must obey the Maxwell's equations. The macroscopic Maxwell's equations in a homogeneous, isotropic, linear dielectric (non-conductor) material are [148]

$$\begin{cases} \nabla \cdot \tilde{E} = 0 \\ \nabla \cdot \tilde{B} = 0 \\ \nabla \times \tilde{E} = -\dfrac{\partial \tilde{B}}{\partial t} \\ \nabla \times \tilde{B} = \mu\varepsilon \dfrac{\partial \tilde{E}}{\partial t} \end{cases} \quad (5)$$

where $\tilde{E}$ and $\tilde{B}$ are the imaginary vector description of the electric and the magnetic fields, respectively; μ is the permeability tensor of the optical medium and ε is the electric permittivity tensor of the optical medium. Since usually, the source of light is an almost monochromatic source, a monochromatic plane wave propagating along a general direction is going to be considered. Its electric and magnetic field vectors can be expressed as

$$\begin{cases} \tilde{\boldsymbol{E}} = \tilde{E}_0 . e^{i(\tilde{\boldsymbol{k}} \cdot \boldsymbol{r} - \omega t + \varphi_E)} \\ \tilde{\boldsymbol{B}} = \tilde{B}_0 . e^{i(\tilde{\boldsymbol{k}} \cdot \boldsymbol{r} - \omega t + \varphi_B)} \end{cases} \quad (6)$$

where, $\tilde{E}_0$ and $\tilde{B}_0$ represent the complex amplitudes of the electric and magnetic fields, and φ_E and φ_B are their displacements, respectively. Also, $\tilde{\boldsymbol{k}}$ is the imaginary wavenumber vector, $\boldsymbol{r}$ is a specific position in space in a certain referential, ω is the angular frequency and t is a specific time moment.

Since the electric and the magnetic fields have a similar behaviour, Eq. (6), one can work only with the electric field and generalize its conclusions to the magnetic field. It should also be considered that the light propagation medium is air, so attenuation effects can be ignored and $\tilde{\boldsymbol{k}}$ becomes a real vector ($\boldsymbol{k}$). By doing these assumptions, a lot of constraints are imposed, and the electric field of a monochromatic collimated beam of light will be

$$\tilde{\boldsymbol{E}}(\vec{\boldsymbol{r}}, t) = \tilde{\boldsymbol{E}}_{\boldsymbol{0}} . e^{i(\boldsymbol{k} \cdot \boldsymbol{r} - \omega t + \varphi_E)} \quad (7)$$

Considering the cartesian z-axis as the light propagation axis, the Maxwell equations guarantee that there will be no magnetic nor electric field in the direction of the light propagation and, therefore, $\tilde{\boldsymbol{H}} = (\tilde{H}_x, \tilde{H}_y, 0)$

and $\widetilde{\boldsymbol{E}} = (\tilde{E}_x, \tilde{E}_y, 0)$. Now, taking into account only the part of the solution that has a physical meaning, i.e. the real part, one finally achieved the components of transverse electrical field [149]

$$\begin{cases} E_x(z,t) = E_{0x} \cdot cos(\tau + \delta_x) \\ E_y(z,t) = E_{0y} \cdot cos(\tau + \delta_y) \\ E_z = 0 \end{cases} \quad (8)$$

where E_{0x} and E_{0y} are the maximum amplitudes of the electric field in its cartesian components, x and y, respectively; δ_x and δ_y are arbitrary phases and $\tau = k \cdot z - \omega t$ is called the propagator. Note that the propagator is used only to simplify Eq. (7), since it is easier to consider a general change in the propagator than time and spatial variations.

6.1. Introduction to polarization

As the electromagnetic wave propagates, the electric field components will construct a pattern. Using simple trigonometric relations and attending that $\delta = \delta_y - \delta_x$, one can demonstrate that the sum of the square of Eq. (8) can be written as

$$\frac{{E_x}^2}{{E_{0x}}^2} + \frac{{E_y}^2}{{E_{0y}}^2} - 2\frac{E_x}{E_{0x}}\frac{E_y}{E_{0y}} cos\,\delta = sin^2\,\delta \quad (9)$$

Equation (9) is recognized as the equation of an ellipse, which means that at any instant of the propagation, the locus of points is described as an ellipse. For this reason, Eq. (9), known as the polarization ellipse equation, discriminates the polarization state.

Figure 26 shows multiple representations of the polarization ellipse for different relative phases, δ, assuming normalized and equal amplitudes ($E_{0x} = E_{0y}$). The polarization states in Figure 26 are: a) linearly polarized at +45° (LP+45°), $\delta = 0°$; b) right elliptically polarized, $\delta = \pi/4$; c) right circularly polarized (RCP), $\delta = \pi/2$; d) right elliptically polarized ($\delta = 3\pi/4$), e) linearly polarized at -45° (LP-45°), $\delta = \pi$; f) left elliptically polarized ($\delta = 5\pi/4$), g) left circularly polarized (LCP), $\delta = 3\pi/2$; and h) left elliptically polarized ($\delta = 7\pi/4$). It can be observed that the area of the polarization ellipse is zero for $\delta = 0$ and π, i.e. light is linearly polarized, and for $\delta = \pi/2$ and $3\,\pi/2$ the area is a maximum and the obtained state of polarization is circularly polarized.

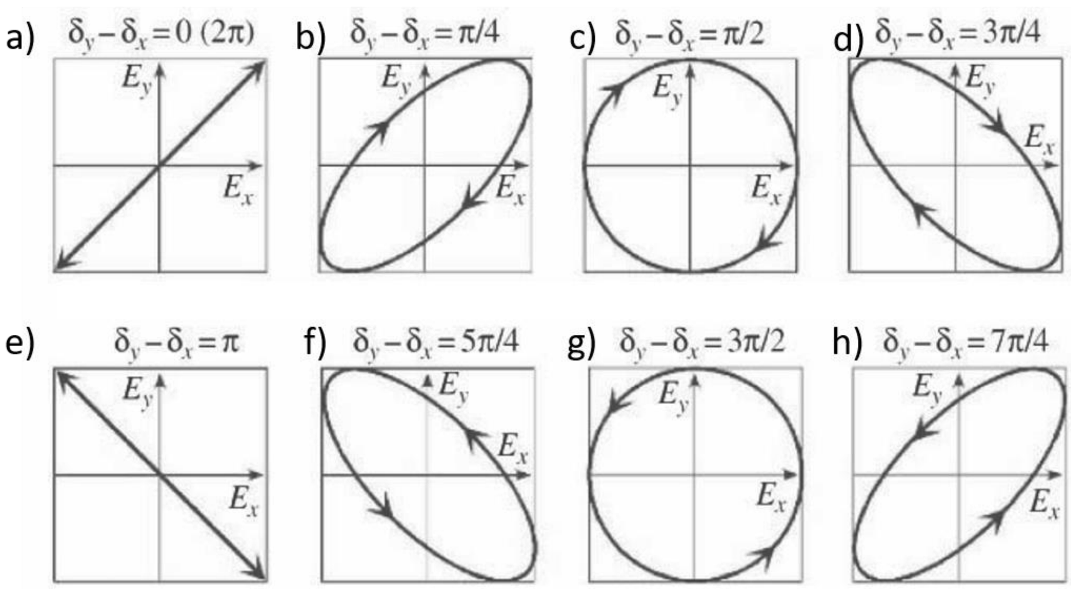

Figure 26. Polarization ellipses for different relative phases $\delta = \delta_y - \delta_x$. The electric field magnitudes are equal ($E_{0x} = E_{0y}$) and normalized. Arrows indicate polarization direction (adapted from Ref. [150]*).*

The latest formulation has a serious limitation, for only being able to describe completely polarized light. Nevertheless, a formalism able to describe not only completely polarized light is needed. Note that polarized beams interacting with real-world materials can result in completely unpolarized or partially polarized light. On the one hand, unpolarized light is described as the superposition of multiple waves randomly polarized, resulting in rapid and random changes in polarization. On the other hand, partially polarized light has a randomly changing polarization state but has a tendency toward a particular state of polarization. For this reason, in order to describe not only fully polarized light, a more suited formalism is needed.

6.2. Mueller-Stokes Formalism

There are different mathematical formalisms to describe polarization states of light beams and their interactions with matter. Based on different authors as Goldstein [149], Azzam [151] and Chipman [152], we have proposed to study polarization by using the Mueller-Stokes formalism. The main reason is because it is the most appropriate representation of polarization when considering not fully polarized light. Along this section, this formalism is presented.

6.2.1. Stokes Parameters

In literature, there are different ways of describing light and its polarization. As stated above, one particularly interesting method of representing light is the Stokes parameters.

The Stokes parameters are a method for characterizing the polarization properties of light beams. This method, presented itself as the most valuable in this study, not only represents polarized and unpolarized light but also represents them in terms of observables or measurable quantities. The Stokes parameters are four observables that can be obtained from the time average values of the squared optical field. Since the square of the electric field was already considered in the polarization ellipse equation (Eq. (9)) and, taking into account that for a monochromatic electromagnetic plane wave the amplitudes (E_{0x}, E_{0y}) and phase (δ) remain constant at all time, the time dependence can be written as

$$\frac{{E_x}^2(t)}{{E_{0x}}^2} + \frac{{E_y}^2(t)}{{E_{0y}}^2} - 2\frac{E_x(t)}{E_{0x}}\frac{E_y(t)}{E_{0y}}\cos\delta = \sin^2\delta \tag{10}$$

Taking the average value over time, Eq. (10) can be represented in terms of the optical observables as

$$\left({E_{0x}}^2 + {E_{0y}}^2\right)^2 - \left({E_{0x}}^2 - {E_{0y}}^2\right)^2 - \left(2E_{0x}E_{0y}\cos\delta\right)^2 = \left(2E_{0x}E_{0y}\sin\delta\right)^2 \tag{11}$$

The four observable quantities inside the parentheses in Eq. (11) are the Stokes parameters [149]

$$\begin{cases} S_0 = {E_{0x}}^2 + {E_{0y}}^2 \\ S_1 = {E_{0x}}^2 - {E_{0y}}^2 \\ S_2 = 2E_{0x}E_{0y}\cos\delta \\ S_3 = 2E_{0x}E_{0y}\sin\delta \end{cases} \tag{12}$$

that can completely describe any state of polarization. Note that Eq. (11) can be rewritten as ${S_0}^2 = {S_1}^2 + {S_2}^2 + {S_3}^2$. In addition, Eq. (12) can be redefined in terms of polarized flux measurements as [153]

$$\begin{cases} S_0 = P_0 + P_{90} \\ S_1 = P_0 - P_{90} \\ S_2 = P_{45} - P_{135} \\ S_3 = P_R - P_L \end{cases} \tag{13}$$

where P_α represents the polarized flux measurements whenever it is analysed the α polarization, being α either a number that characterises the azimuth of the linear polarizer light (0°, 45°, 90° and 135°), either a letter that represents the direction of the circularly polarized light, being clockwise, R, or counterclockwise,

L. Therefore, the first Stokes parameter, S_0, is the total intensity of the light beam; S_1 is a way of describing the amount of linear horizontal (0°) and vertical (90°) polarization; S_2 describes the amount of linear +45° or -45° polarization; and the parameter S_3 is the description of the amount of right (R) or left (L) circular polarization.

One might also understand that the derivation to obtain the Stokes parameters was made by using a case of totally polarized light, and so, in order to consider every single case (partially polarized and unpolarized light), Eq. (11) must be written by using the Schwarz's inequality [149]

$$ {S_0}^2 \geq {S_1}^2 + {S_2}^2 + {S_3}^2 \tag{14} $$

If the light beam is completely polarized, Eq. (14) will be an equality. However, for unpolarized light ${S_0}^2 > 0$ (there is no preference for any particular polarization state, i.e. $S_1 = S_2 = S_3 = 0$), and for partially polarized light "$\geq$" is replaced by "$>$" (i.e., ${S_0}^2 > {S_1}^2 + {S_2}^2 + {S_3}^2$).

Additionally, the Stokes parameters can be concatenated in a vector (known as Stokes vector). A simple way of generalizing it, to describe every state of polarization, is by separating the Stokes vector $(\boldsymbol{S})$ in two different vectors. These two vectors represent the completely polarized content $(\boldsymbol{S_p})$ and the fully unpolarized content $(\boldsymbol{S_u})$ of the light beam [152]

$$ \boldsymbol{S} = \boldsymbol{S_p} + \boldsymbol{S_u} \quad \Leftrightarrow \quad \begin{pmatrix} S_0 \\ S_1 \\ S_2 \\ S_3 \end{pmatrix} = \begin{pmatrix} \sqrt{{S_1}^2 + {S_2}^2 + {S_3}^2} \\ S_1 \\ S_2 \\ S_3 \end{pmatrix} + \left(S_0 - \sqrt{{S_1}^2 + {S_2}^2 + {S_3}^2} \right) \begin{pmatrix} 1 \\ 0 \\ 0 \\ 0 \end{pmatrix} \tag{15} $$

The degree of polarization (DoP) for any state of polarization is, by definition, the fraction of the intensities sum of the polarization components (I_{Pol}) by the total intensity of the beam (I_{tot}) [149],

$$ DoP = \frac{I_{Pol}}{I_{tot}} = \frac{\sqrt{{S_1}^2 + {S_2}^2 + {S_3}^2}}{S_0} \qquad 0 \leq DoP \leq 1 \tag{16} $$

If $DoP = 0$, the measured light is completely unpolarized and whenever $DoP = 1,$ the beam measured is fully polarized. The intermediate states, $0 < DoP < 1$, correspond to partially polarized light [149].

In order to describe not only polarized light but also depolarized or partially polarized light, Eq. (12) is generalized as

$$\boldsymbol{S} = \begin{pmatrix} S_0 \\ S_1 \\ S_2 \\ S_3 \end{pmatrix} = \begin{pmatrix} \langle E_p E_p^* + E_s E_s^* \rangle \\ \langle E_p E_p^* - E_s E_s^* \rangle \\ \langle E_p E_s^* + E_s E_p^* \rangle \\ i\langle E_p E_s^* - E_s E_p^* \rangle \end{pmatrix} \tag{17}$$

where the electric field subscripts, s and p, describe its perpendicular and parallel components with respect to the plane of incidence, respectively.

6.2.2. Poincaré Sphere

The Poincaré sphere is a concept that, using a unit sphere centred in the Cartesian coordinate system, and as orthogonal axis the three components of the Stokes vector (S_1, S_2, S_3), represents any state of polarization as a punctual site in this three-dimensional space (see Figure 27). To the concept is given this name because any normalized Stokes vector ($s_1 = \frac{S_1}{S_0}$, $s_2 = \frac{S_2}{S_0}$, $s_3 = \frac{S_3}{S_0}$) will be comprehended inside this sphere of radius 1. This representation helps us to quickly visualize any state of polarization. Figure 27 shows an example of an elliptical polarization state over the surface of the Poincaré Sphere. Note that any point over the surface of the Poincaré sphere corresponds to a fully state of polarization. More specifically, linear polarization states are represented along the equator, while north and south poles (S_3 axis) are the right and left circularly polarized states, respectively. In addition, the polarization state centred in the origin of the Poincaré sphere (0, 0, 0) is a totally depolarized state, meaning that any intermediate state between the origin and the Poincaré sphere's shell is a partially polarized state

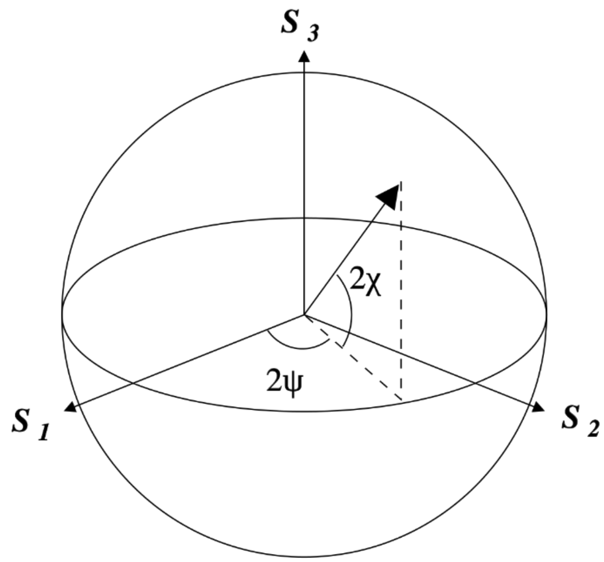

Figure 27. A polarization state represented in the Poincaré Sphere (adapted from reference *[154]*).

As can be seen in Figure 27, any state of polarization can be represented in terms of the components named ellipticity angle, χ, and the orientation angle, Ψ, given by

$$sin(2\chi) = \ s_3 \quad , \quad -\frac{\pi}{4} \leq \ \chi \leq \frac{\pi}{4} \tag{18}$$

$$tan(2\psi) = {}^{s_2}/_{s_1} \quad , \quad 0 \leq \Psi \leq \pi \tag{19}$$

Arranging equations (18) and (19), the Stokes vector can be written as

$$\boldsymbol{S} = S_0 \begin{pmatrix} 1 \\ cos\, 2\chi\, cos\, 2\Psi \\ cos\, 2\chi\, sin\, 2\Psi \\ sin\, 2\chi \end{pmatrix} \tag{20}$$

6.2.3. Mueller Matrices

The interaction of a light beam with a medium was described by Mueller in 1948. In this formulation, Mueller defined all polarizing properties of a sample (diattenuation, retardance and depolarization) in a four-by-four matrix, M, that allows a simple correlation between the incident $(\boldsymbol{S_{in}})$ and exiting $(\boldsymbol{S_{out}})$ Stokes vectors as [152]

$$S_{out} = \begin{pmatrix} M_{00} & M_{01} & M_{02} & M_{03} \\ M_{10} & M_{11} & M_{12} & M_{13} \\ M_{20} & M_{21} & M_{22} & M_{23} \\ M_{30} & M_{31} & M_{32} & M_{33} \end{pmatrix} \cdot S_{in} = M \cdot S_{in} \tag{21}$$

Figure 28 shows an incident beam interacting with a sample in transmission and in reflection. In addition, if a light beam goes through a series of polarization elements or interacts with multiple elements, these interactions are taken into account by the multiplication of each individual Mueller matrix M_q, where M_q is the q-th of the Q elements that interact with the light beam. In a mathematical way, this is placed as

$$M = M_Q \cdot M_{Q-1} \cdot \ldots \cdot M_q \cdot \ldots \cdot M_2 \cdot M_1 = \prod_{q=0}^{Q-1} M_{Q-q} \tag{22}$$

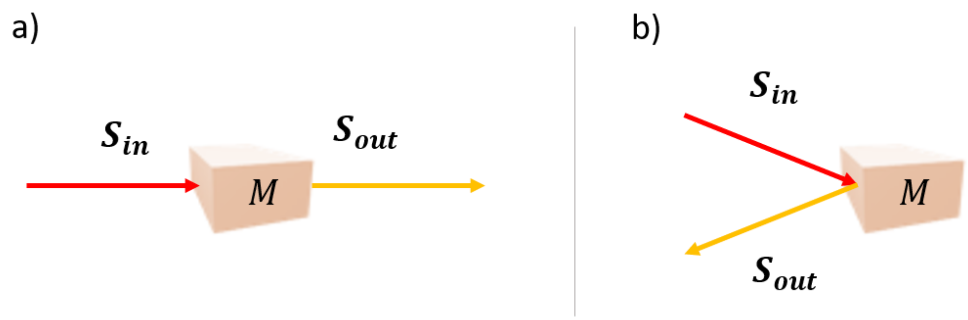

Figure 28. Schematic representation of different unique interactions light-matter: a) a light transmission over a sample, and b) a simple reflection, or scatter. S_{in} and S_{out} are the incident and exiting Stokes vectors, respectively, and M is the characteristic Mueller matrix of the sample.

It should be noted that, from a Mueller matrix, one can extract light properties such as how an interaction light-matter changes the light intensity (M_{00}) and the three fundamental polarization properties, which are diattenuation, retardance and depolarization [149].

M_{00}

The beam intensity changes once the light interacts with matter [155]. This happens due to the different properties of a present material, as for example, the material in study can absorb some part of the light, or it can also disperse the light in a way that the detector can not sensor it [155].

The M_{00} element of a Mueller Matrix is the element responsible to scale the output intensity with respect to the input intensity [155]. This component can also be seen as the transmittance or reflectance if the system is being analysed in transmission or reflection, respectively [155].

Diattenuation

Diattenuators are optical components that attenuate differently the amplitude of the orthogonal components of the electric field vector [149], [156]. In this sense, the diattenuation D is the change in the intensity transmittances T of the incident polarization state [149], [156],

$$D = \frac{T_{max} - T_{min}}{T_{max} + T_{min}} \qquad 0 \leq D \leq 1 \tag{23}$$

where the subscript max and min are mean maximum and minimum, respectively [149], [156]. Linear polarizers are diattenuators that extinguish one of the orthogonal components of the electric field vector ($T_{min} = 0$ and $D = 1$). Since the diattenuation causes different changes in the different polarization states, this characteristic is usually represented as a vector $\boldsymbol{D}$ that provides a complete description of the diattenuation properties. Its components are called horizontal, D_H, 45° linear, D_{45}, and circular, D_c, diattenuation [149], [156] and their direct relations with the Mueller matrix are [149]

$$\boldsymbol{D} = \begin{pmatrix} D_H \\ D_{45} \\ D_C \end{pmatrix} = \frac{1}{M_{00}} \begin{pmatrix} M_{01} \\ M_{02} \\ M_{03} \end{pmatrix} \tag{24}$$

Note that Eq. (23) is still valid and can be used to determinate each one of the $\boldsymbol{D}$ components, as a simple experimental determination method. In terms of the Poincaré sphere, perfect diattenuators act like a polarization filter that project different polarization states into a chosen one. A frequent kind of diattenuators used in optics are Linear Polarizers (LP).

Retardance

Retardance is the optical property that describes how the orthogonal electric field components are delayed once interacting with a retarder. These elements have a preferential path that is called the fast axis orientation, and a slow axis orientation where the electric field is delayed, i.e. retarded. Meaning that the retardance defines the relative phase change between the fast and slow axes. In this sense, retarders are mainly responsible for changing the ellipticity angle (χ) and the orientation angle (Ψ) of the light polarization state in the Poincaré sphere (see Figure 27). Two polarization components that show a behaviour like this are Quarter Wave Plates (QWP) and Half Wave Plates (HWP).

Depolarization

Depolarization indicates how a state of polarization is converted into unpolarized light, without changing the light intensity. Of all the mathematical formalisms that exist, Mueller's formalism is the only one that considers depolarization, being this the one that provides a complete description of polarized light.

In terms of the Poincaré sphere, these components are responsible for translating a perfect polarized state represented in the shell of the sphere to an internal site inside the Poincaré sphere.

6.2.4. Polarimetric measurement principle

The real matrix that completely describes the polarization properties in an interaction with a material is measured in Mueller matrix polarimetry [149], [152], [153], [157]. A Mueller matrix polarimeter is composed by a light source that illuminates the sample to be analysed, a polarization state generator (PSG) that controls the polarization of the illumination beam, a polarization state analyser (PSA) which analyses the light transmitted/reflected by the sample, and a detector acquiring the intensity exiting the PSA [149], [152], [153], [157] (see Figure 29).

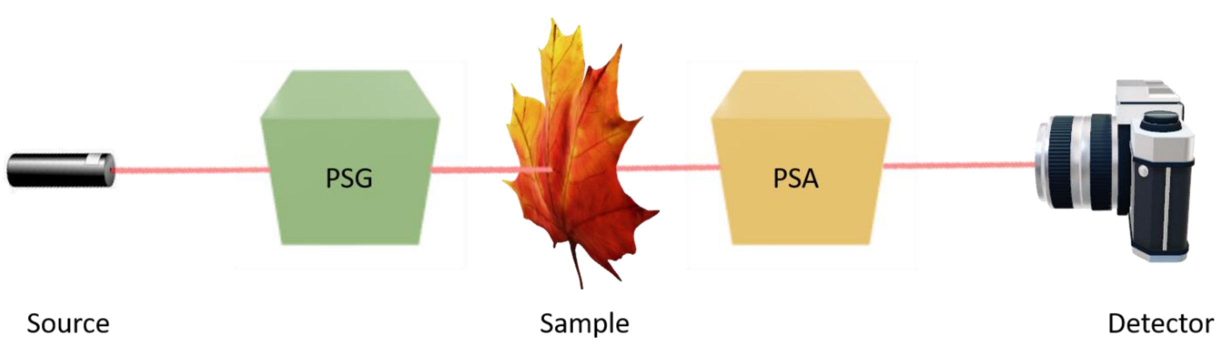

Figure 29. Conceptual illustration of a Mueller polarimeter in transmission. The light from the source, polarized by the PSG, interacts with the sample. The changes in polarization are then measured in the detector, by the amount of light intensity that goes through the PSA.

A Mueller matrix polarimeter takes Q intensity measurements. For the qth measurement, the PSG generates a light beam with a Stokes vector S_q that is analysed by the analyser vector A_q generated by the PSA. Thus, from Eqs. (21) and (22), the measured Intensity I_q from the detector is related to the sample Mueller matrix by [149], [152], [157]

$$I_q = {A_q}^T \cdot M \cdot S_q = \begin{pmatrix} a_{q0} & a_{q1} & a_{q2} & a_{q3} \end{pmatrix} \cdot \begin{pmatrix} M_{00} & M_{01} & M_{02} & M_{03} \\ M_{10} & M_{11} & M_{12} & M_{13} \\ M_{20} & M_{21} & M_{22} & M_{23} \\ M_{30} & M_{31} & M_{32} & M_{33} \end{pmatrix} \cdot \begin{pmatrix} S_{q0} \\ S_{q1} \\ S_{q2} \\ S_{q3} \end{pmatrix} \tag{25}$$

Note that $q = 0,1, \dots, Q-1$, and S_q is the product of the Stokes vector of the light source with the Mueller matrix of the PSG [149], [152], [157]. Also, it is only used the analyser vector A_q, that corresponds to the first row of the analyser Mueller matrix, instead of the whole analyser matrix (A), because in this formalism it is the only sequence that interferes with the change of intensity to be measured by the detector [152]. Equation (25) can be rearranged as a vector-vector dot product as [149], [152], [157]

$$I_q = \begin{pmatrix} a_{q0}S_{q0} \\ a_{q0}S_{q1} \\ a_{q0}S_{q2} \\ a_{q0}S_{q3} \\ a_{q1}S_{q0} \\ a_{q1}S_{q1} \\ \vdots \\ a_{q3}S_{q3} \end{pmatrix}^T \cdot \begin{pmatrix} M_{00} \\ M_{01} \\ M_{02} \\ M_{03} \\ M_{10} \\ M_{11} \\ \vdots \\ M_{33} \end{pmatrix} = {W_q}^T \cdot \vec{M} \tag{26}$$

where the Mueller matrix M is flattened into a 16×1 Mueller vector $\vec{M}$, and W_q is the 16×1 polarimetric measurement vector for the qth measurement with intensity I_q [149], [152], [157]. The full sequence of polarimetric measurements is described by the $Q \times 16$ matrix W, where the qth row is ${W_q}^T$, and by the measured intensity vector I, where the qth element is I_q, [149], [152], [157]

$$I = W \cdot \vec{M} \Leftrightarrow \begin{pmatrix} I_0 \\ I_1 \\ \vdots \\ I_q \\ \vdots \\ I_{Q-1} \end{pmatrix} = \begin{pmatrix} {W_0}^T \\ {W_1}^T \\ \vdots \\ {W_q}^T \\ \vdots \\ {W_{Q-1}}^T \end{pmatrix} \cdot \begin{pmatrix} M_{00} \\ M_{01} \\ \vdots \\ M_{33} \end{pmatrix} \tag{27}$$

Note that, if the matrix W has 16 linearly independent columns, the Mueller Matrix has a unique solution for all its 16 elements [149], [152], [157]. So, at least 16 values of I should be measured, with 16 linearly independent combinations of states generated by the PSG with states analysed by the PSA ($Q = 16$) [149], [152], [157].

In the particular case of using 4 PSG and 4 PSA polarization states ($Q = 16$), Eq. (27) is solved as [149], [152], [157]

$$\vec{M} = W^{-1} \cdot I \tag{28}$$

Often it is measured more than 16 arrangements ($Q > 16$), so that the extra measurements can correct possible problems as, for example, linearly dependent states. In this case $\vec{M}$ is overdetermined [149], [152], [157]. In this case, it is employed the optimal least-squares polarimetric data reduction, that uses the pseudoinverse of W [149], [152], [157]. The polarimetric data reduction equation $Q > 16$ is then described as [149], [152], [157]

$$\vec{M} = {W_P}^{-1} \cdot I = (W^T W)^{-1} W^T \cdot I \tag{29}$$

where ${W_P}^{-1}$ is the pseudoinverse of W and operates on a set of arrangements of the system to estimate the Mueller matrix of a sample [149], [152], [157].

If the engendered polarization states in the PSG and PSA are not well distributed in the Poincaré sphere or only some states are produced, the capabilities of the Mueller polarimeter may be compromised, in the sense that only some components can be achieved with great accuracy and precision. This type of polarimeter is usually called as incomplete Mueller polarimeter. Note that, for some applications, it is more interesting to only measure the incomplete Mueller matrix, as it is stated in references [146], [149], [157], [158].

6.2.5. Condition Number

The condition number (CN) of a square non-singular matrix indicates how well conditioned is a system [159]. In other words, it represents how much the presence of error sources influence the accuracy of the solution [159]. To minimize this error sources influence, one may choose the combination of PSG and PSA that diminishes the most the error presence. One way of doing this is by evaluating the CN of each individual PSG and PSA matrices. The CN should theoretically range from 1 to ∞, where a smaller value means a better conditioned system. In particular, for a Mueller polarimeter setup, it has been shown that the smallest CN possible is $\sqrt{3}$ [153], [160].

There are multiple metrics to determine the CN, and although they differ for a given matrix, they are all related to each other and so, provide the same knowledge [161]. One way of obtaining the CN is by singular value decomposition (SVD) of the matrix W. This technique consists in factorize the matrix W into two unitary matrices, U and V, with a diagonal matrix, $Diag$, as follow

$$W = U \cdot Diag \cdot V^T \tag{30}$$

The diagonal elements of $Diag$ are called the singular values of W. Note that the used condition number is based on the Euclidian length of the matrix rows and it is equal to the ratio of the largest to the smallest singular values [162].

6.2.6. Mueller Decomposition

As it was already said in section 6.2.3, Mueller matrices can integrate diattenuation, retardance and depolarization effects. In literature, there are multiple different ways of acquiring these three main properties out of an experimental normalized Mueller matrix, $\mathcal{M} = \frac{M}{\mathrm{M}_{00}}$. In this section, the Lu-Chipman decomposition [156] is explored.

The main advantage of the Lu-Chipman decomposition is that it always leads to a Mueller matrix with a physical meaning. In this description, a Mueller matrix can be written as the product of a pure depolarizer, a pure retarder and a pure diattenuator. The suggested decomposition is only attainable if it follows the decomposition order like the following [156]

$$\mathcal{M} = \frac{M}{M_{00}} = \begin{bmatrix} 1 & m_{01} & m_{02} & m_{03} \\ m_{10} & m_{11} & m_{12} & m_{13} \\ m_{20} & m_{21} & m_{22} & m_{23} \\ m_{30} & m_{31} & m_{32} & m_{33} \end{bmatrix} = M_{\Delta} \cdot M_R \cdot M_D \qquad (31)$$

where M_{Δ} is the pure depolarizer Mueller matrix, M_R represents the pure retarder Mueller matrix and M_D is the pure diattenuator Mueller matrix.

To decompose any experimental Mueller matrix into its respective Mueller matrices of a depolarizer, a retarder and a diattenuator, firstly, one has to consider the normalized Mueller matrix as [156]

$$\mathcal{M} = \begin{bmatrix} 1 & \boldsymbol{D}^T \\ \boldsymbol{P} & m \end{bmatrix} \qquad (32)$$

where $\boldsymbol{D}$ is the diattenuation vector defined in Eq. (24), $\boldsymbol{P} = \begin{pmatrix} m_{10} \\ m_{20} \\ m_{30} \end{pmatrix}$ is the polarizance vector, and m is a three-by-three submatrix. To proceed with the determination of each proposed matrix, let one consider the following quantities

$$a = \sqrt{1 - \boldsymbol{D}^T\boldsymbol{D}} \qquad (33)$$

and

$$b = \frac{1 - a}{\boldsymbol{D}^T\boldsymbol{D}} \qquad (34)$$

Now, one can determine the diattenuator matrix as

$$M_D = \begin{pmatrix} 1 & \boldsymbol{D}^T \\ \boldsymbol{D} & m_D \end{pmatrix} \qquad (35)$$

where

$$m_D = a \begin{bmatrix} 1 & 0 & 0 \\ 0 & 1 & 0 \\ 0 & 0 & 1 \end{bmatrix} + b(\boldsymbol{D} \times \boldsymbol{D}^T) \qquad (36)$$

and, also, compute the retarder matrix

$$M_R = \begin{pmatrix} 1 & 0^T \\ 0 & m_R \end{pmatrix} \qquad (37)$$

where

$$m_R = \frac{1}{a}\left(m - b(\boldsymbol{P} \cdot \boldsymbol{D}^T)\right) \quad (38)$$

At last, to determine the depolarizer matrix M_Δ, since $\mathcal{M}$ is a known Mueller matrix, one must recall Eq. (31) and solve it.

$$\mathrm{M}_\Delta = \mathrm{M} \cdot \mathrm{M_R}^{-1} \cdot \mathrm{M_D}^{-1} \quad (39)$$

In later sections, this decomposition is used to analyse the experimental Mueller matrices.

6.3. Experimental Set-Up

In this section, the two different setups that were used to determine the Mueller matrices of materials are presented: a mechanically rotating setup using LPs and QWPs, and a phase modulation setup using LPs and Liquid Crystal Variable Retarders (LCVRs).

6.3.1. Mueller Polarimeter with rotating QWPs and LPs

Firstly, it was considered the classical measurement method approach of the Stokes polarization parameters using mechanically rotating QWPs and LPs. The Figure 30 is a representation of the built setup. In this setup, light from a 1550 nm laser (*Thorlabs* [163], Model LDM1550) goes through the PSG, constituted by a rotating LP (*Thorlabs* [163], Model GTH10M) followed by a QWP (*Thorlabs* [163], Model WPQ10ME). A laser source is usually linearly polarized meaning that, once the PSG's LP starts changing the state generated, and according to the Malus' Law [152], the intensity of the generated state is also going to change [164]. To avoid intensity oscillations due to the polarization of the source, a QWP (*Thorlabs* [163], Model WPQ10ME) is placed after the laser source, i.e. before the PSG, in a way that the light exiting this QWP is circularly polarized.

After the PSG, polarized light interacts with samples, and then, light reflected by the sample passes through the PSA, founded by a rotating QWP (*Thorlabs* [163], Model WPQ10ME) followed by a rotating LP (*Thorlabs* [163], Model LPNIR100-MP2), being finally detected by a camera (*Allied Vision* [165], Model GoldEye G-033 TEC1-C) with a camera lens (*Kowa* [166], with a focal length of 35 *mm*, Model SWIR Lens - CBC-IP2-M3514) to form an image of the sample.

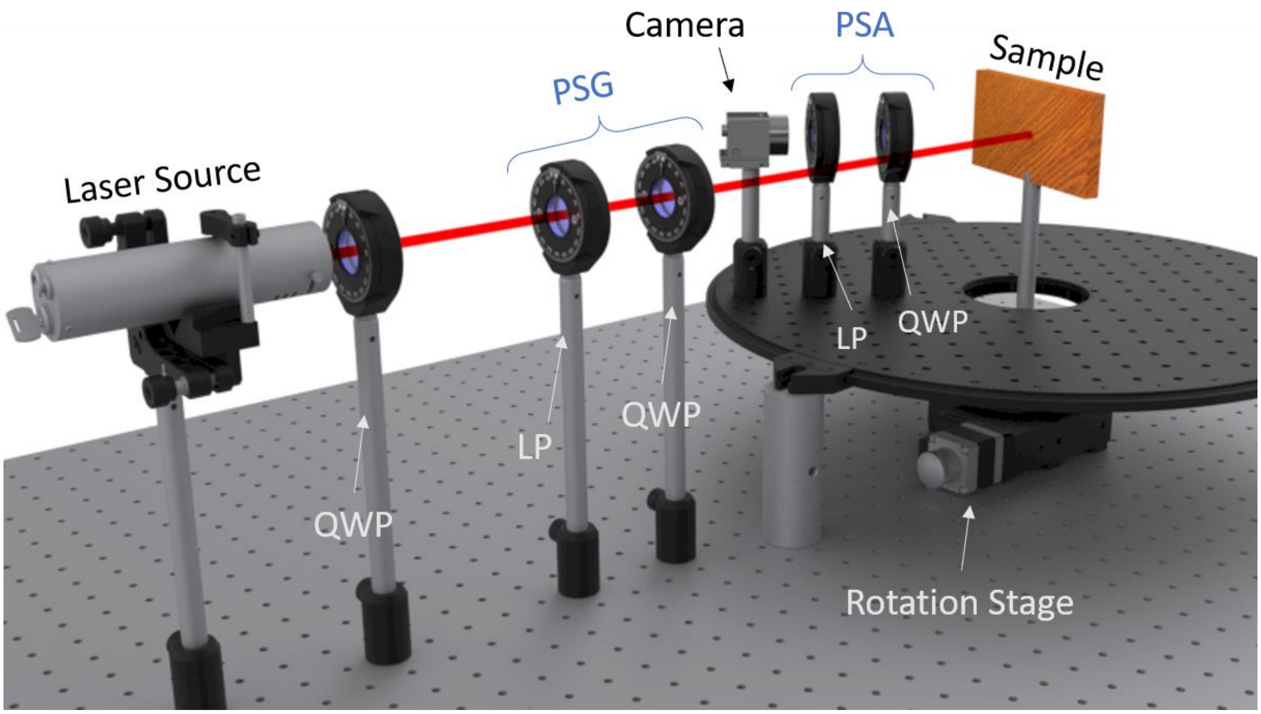

Figure 30. Laboratorial setup illustration of our Mueller Polarimeter with rotating QWPs and LPs.

In addition, the PSA and the detection system are placed over a rotation stage (*Thorlabs* [163], Model RBB450A/M) to allow measurements in transmission, to calibrate the system, and in reflection, to take the so needed measurements.

The setup also includes a motorized rotation stage (*Thorlabs* [163], Model HDR50/M) in order to change the sample rotation angle of the sample. This rotation stage allows to measure polarization properties of specular reflection and scattering light in relation to the Sample Rotation Angle (SRA) [167]. In this setup the laser and camera are maintained fixed as close as possible to each other. This was made in order to try to mimic a LiDAR's behaviour. Due to this constraint, the SRA is described as the angular offset from the specular light detected in the camera (see Figure 31), i.e. when SRA $= 0°$, the camera will detect the specular reflection. In our polarimeter, the light source and the detection arms have a bistatic angle, β in Figure 31, between them of $13.3°$ ($\beta = 13.3°$).

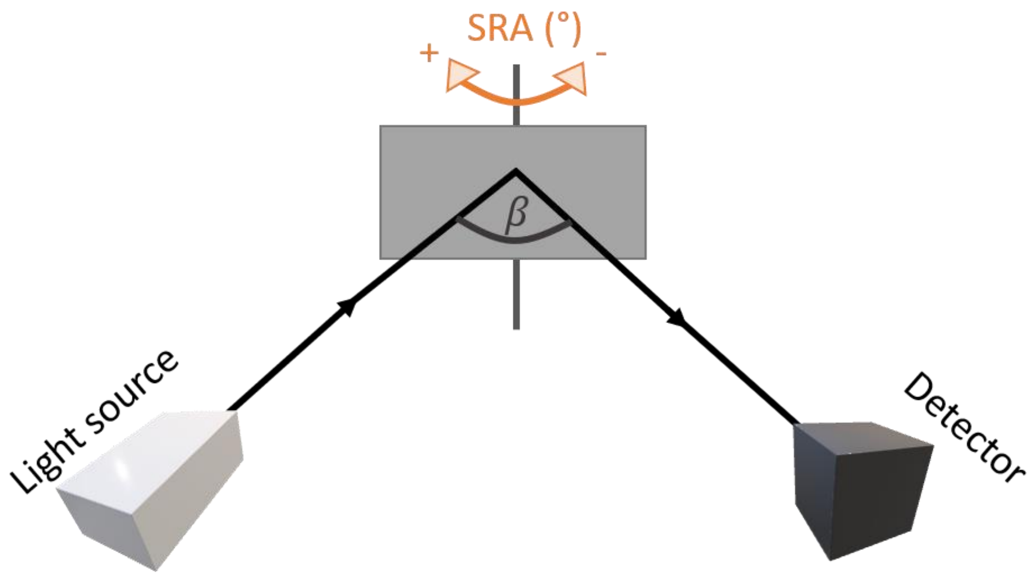

Figure 31. The sample rotation angle (SRA) is measured with respect to the specular reflection condition. The bistatic angle between the light source and the detection arm is $\beta = 13.3°$ *(adapted from reference* [167]*.*

In this sense, firstly it is needed to use a highly reflective sample to do an angle calibration, i.e. look for the angle where highest detected intensity was shown and mark it as the 0° of the system.

The referred Mueller polarimeter setup is shown in Figure 32. Its main components are labelled.

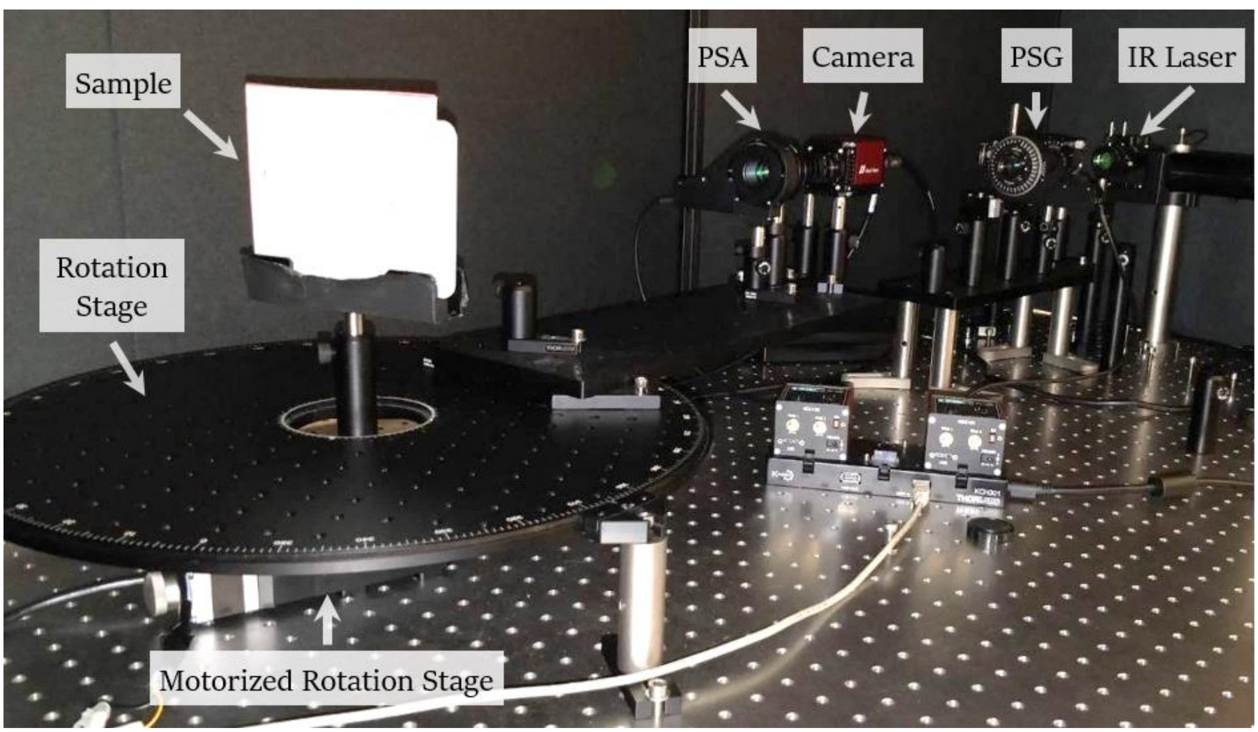

Figure 32. Experimental implementation of the Mueller polarimeter designed with QWP developed in the University of Minho (the main components are labeled).

6.3.2. Mueller Polarimeter based on liquid crystal variable retarders (LCVRs)

A downside in the setup presented in section 6.3.1, predicted in the literature [152], [153], [157], is that mechanically rotating elements setups cause beam wandering and positioning errors, due to the high dependency on the alignment, introducing errors in the calculated Mueller matrices. In addition, to rotate each optical element consumes a large amount of time. For these reasons, this setup was improved by using a static configuration for the PSG and the PSA. We have introduced variable retarders, liquid crystal variable retarders (LCVRs), depending on the applied voltage and the orientation on the fast axis, without requiring any mechanical movement [152], [153], [157].

Liquid Crystal (LC) retarder cells are used to dynamically change the polarization properties by imposing an external electric field to the cell being, in this sense, considered as static. Figure 33 shows a retardance versus voltage curve of a linear retardance modulator with axis along x and y. As the voltage changes, the transparent molecules are rotating in the x-z plane, but remaining nearly constant in y. Since it is considered that light is traveling in the z axis, the refractive index will cause a retardation in the x component in relation to the y component.

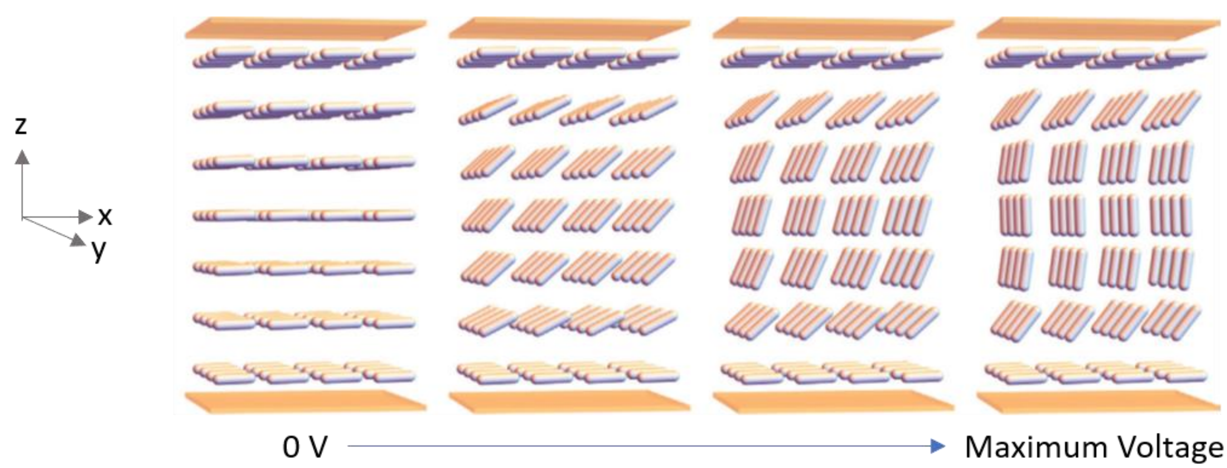

Figure 33. Schematic of the molecules' orientation on a nematic retardation modulator liquid crystal in accordance to the increasing applied, adapted from reference [157].

The representation of the referred setup is shown in Figure 34. In this setup, a 1550 nm laser light source that goes through the PSG, constituted by a static LP (*Thorlabs* [163], Model LPNIR100-MP2) followed by two LCVRs (*Meadowlark Optics* [168], LRC-300-IR3), is reflected by the sample. Then, it passes through the PSA, that contains two LCVRs (*Meadowlark Optics* [168], LRC-300-IR3) followed by a fixed LP (*Thorlabs* [163], Model LPNIR100-MP2), being finally detected by a camera (Allied Vision [165], Model GolEye G-033 TEC1-C) with a camera lens (*Kowa* [166], with a focal length of 35 *mm*, Model SWIR Lens - CBC-IP2-M3514) to image the sample.

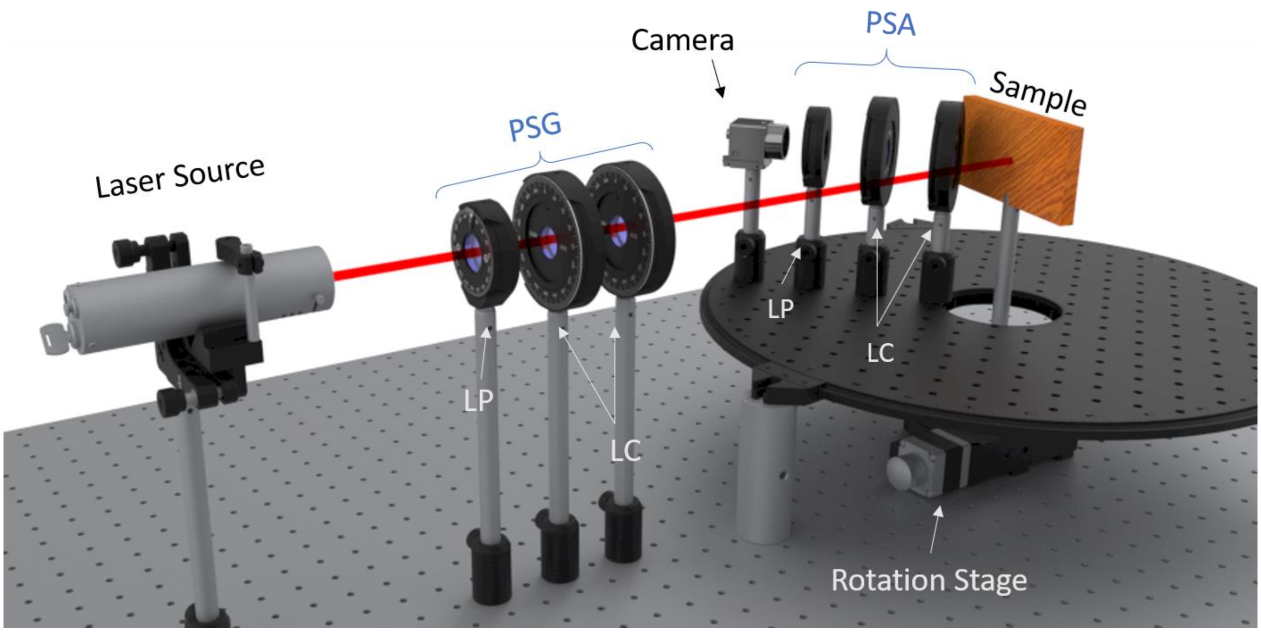

Figure 34. Laboratorial setup illustration of a Mueller Polarimeter with rotating liquid crystal variable retarders (LCVRs) and static LPs

As the setup in section 6.3.1, this setup includes a rotation stage that rotates each sample, in order to change the sample rotation (SRA). Note that the SRA is described as in the previous subsection (see section 6.3.1). In this type of setup, there is not verified beam wandering and this approach is considerably less time-consuming than the Mueller Polarimeter with rotating QWPs and LPs. However, LCs material have a dependency on temperature, approximately -0,4% per °C [169]. To maintain the systems behaviour constant and solve this possible problem, in the construction of the laboratorial setup, we have used full-wave LC retarders from *Meadowlark Optics* [168] and periodically we calibrate and test our Mueller polarimeter. The changes imposed by the temperature in the built setup were unnoticed. The final experimental setup is shown in Figure 35 and its main components are labelled.

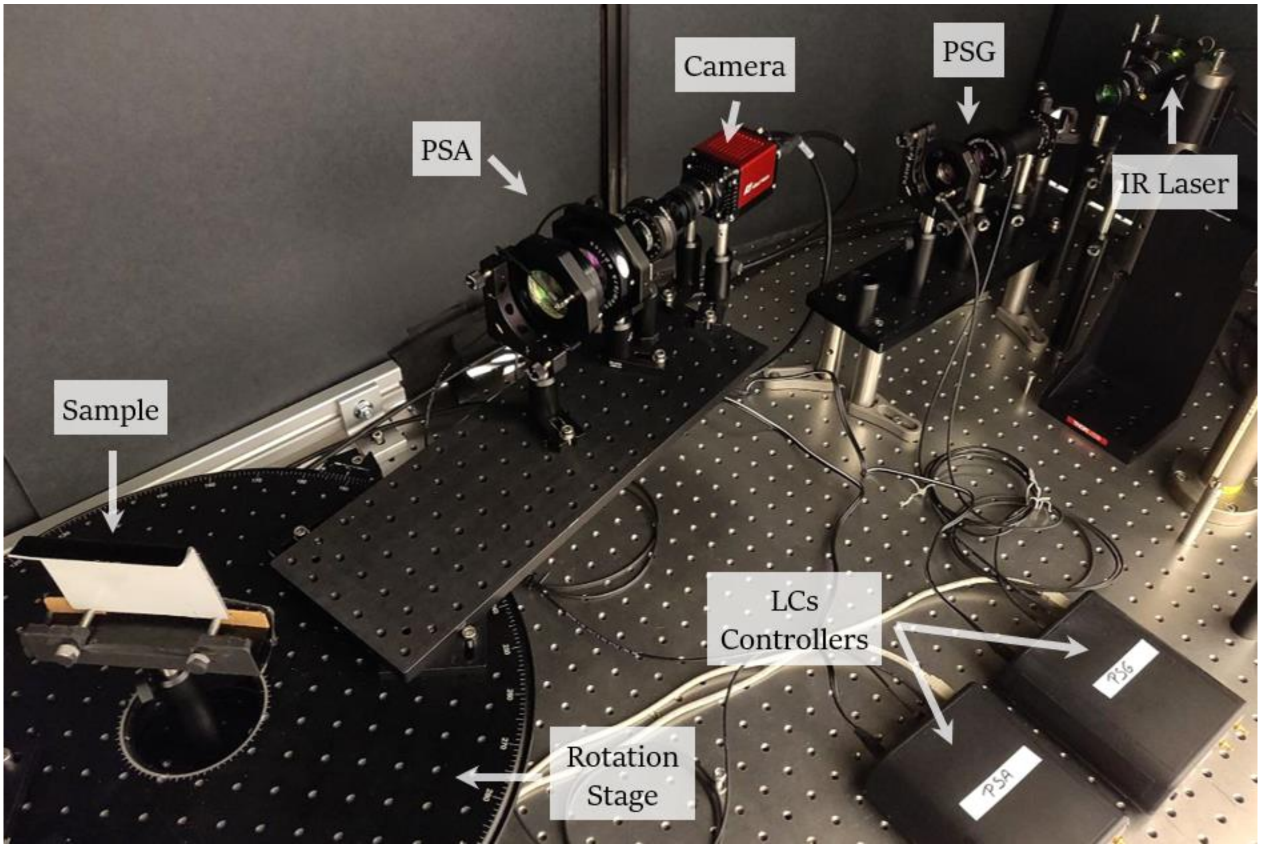

Figure 35. Experimental implementation of the Mueller polarimeter designed with liquid crystal variable retarders (LCVRs) developed in the University of Minho (the main components are labeled).

6.3.3. Setup Calibration

To have accurate polarimetric measurements, it is needed to calibrate the setup, that it is done by calibrating the PSG and the PSA individually. To perform accurate polarimetric measurements there is no need to have ideal polarization elements, but it is needed to know with great accuracy the states exiting the PSG and the states analysed by the PSA. If this requirement is met, systematic errors due to non-ideal components are removed during the data reduction process. To this end, a commercial polarimeter (PAX1000IR2/M [163] from *Thorlabs)* is used to accurately determine the PSG exiting states and the analysing PSA states. There are multiple ways of calibrating the PSG and PSA (see references [149], [151]–[153], [170]). Based on the mathematical formalism described in section 6.2.4, we decided to characterize the PSA in reverse to its usage, meaning that the light should be going through it in the opposite direction.

Although it is only need four linearly independent states of polarization generated by the PSG and analyzed by the PSA, with the purpose of generating easy to find polarization states and roam the entire Poincaré sphere, it was decided to use the 6 standard polarization states: HLP (horizontal linear polarization), VLP (vertical linear polarization), LP+45 (+45° linear polarization), LP-45 (-45° linear polarization), RCP (right circularly polarization) and LCP (left circularly polarization). The theoretical CN of this configuration is $\sqrt{3}$ (see section 6.2.5).

Calibration of the Mueller polarimeter with rotating QWPs and LPs in section 6.3.1.

In order to select the PSG and PSA states, a mathematical prediction is made. In ideal conditions, the PSA and PSG calibration Mueller matrix are the same

$$S_{out} = M_{PSG/PSA} \cdot S_{in} = M_{LR}(\theta_2, \delta) \cdot M_{LP}(\theta_1) S_{in} =$$

$$= \begin{bmatrix} 1 & 0 & 0 & 0 \\ 0 & cos^2(2\theta_2) + sin^2(2\theta_2)\, cos(\delta) & sin(2\theta_2)\, cos(2\theta_2)\,(1 - cos(\delta)) & -sin(2\theta_2)\, sin(\delta) \\ 0 & sin(2\theta_2)\, cos(2\theta_2)(1 - cos(\delta)) & sin^2(2\theta_2) + cos^2(2\theta_2)\, cos(\delta) & cos(2\theta_2)\, sin(\delta) \\ 0 & sin(2\theta_2)\, sin(\delta) & -cos(2\theta_2)\, sin(\delta) & cos(\delta) \end{bmatrix} \quad (40)$$

$$\cdot \frac{1}{2} \begin{bmatrix} 1 & cos(2\theta_1) & sin(2\theta_1) & 0 \\ cos(2\theta_1) & cos^2(2\theta_1) & 0.5\, sin(4\theta_1) & 0 \\ sin(2\theta_1) & 0.5\, sin(4\theta_1) & sin^2(2\theta_1) & 0 \\ 0 & 0 & 0 & 0 \end{bmatrix} \cdot S_{in}$$

where S_{in} and S_{out} are the Stokes vectors that represent the light before and after the PSG/PSA, respectively, and $M_{PSG/PSA}$ is the Mueller matrix corresponding to the PSG/PSA. M_{LR} is the Mueller matrix of a Linear Retarder, which in this case is a QWP, and M_{LP} is the Mueller matrix of a Linear Polarizer. θ_1 is the angle of the transmission axis of the Linear Polarizer, δ is the retardance of the Linear Retarder, which is $\delta = \frac{\pi}{2}$ for a QWP, and θ_2 is the angle of the fast axis of the QWP.

If we consider that the light from our source is completely right circularly polarized, due to the presence of the first QWP (see Figure 30), and normalized to its intensity, $S_{in} = (1 \quad 0 \quad 0 \quad 1)^T$, and Eq. (40) becomes

$$S_{out} = M_{PSG/PSA} \cdot \begin{pmatrix} 1 \\ 0 \\ 0 \\ 1 \end{pmatrix} \Leftrightarrow S_{out} = \frac{1}{2} \begin{bmatrix} 1 \\ \cos^2(2\theta_2)\cos(2\theta_1) + \frac{1}{2}\sin(4\theta_2)\sin(2\theta_1) \\ \sin(2\theta_2) \cdot \cos(2\theta_1 - 2\theta_2) \\ -\sin(2\theta_1 - 2\theta_2) \end{bmatrix} \quad (41)$$

In an ideal optical system, Table 4 shows some S_{out} values for a set of θ_1 and θ_2 as guidance to generate the desired calibration states.

Table 4. Calibration states summary for the Mueller polarimeter with rotating QWPs and LPs

HLP $\begin{pmatrix}1\\1\\0\\0\end{pmatrix}$	VLP $\begin{pmatrix}1\\-1\\0\\0\end{pmatrix}$	LP+45° $\begin{pmatrix}1\\0\\1\\0\end{pmatrix}$	LP-45° $\begin{pmatrix}1\\0\\-1\\0\end{pmatrix}$	RCP $\begin{pmatrix}1\\0\\0\\1\end{pmatrix}$	LCP $\begin{pmatrix}1\\0\\0\\-1\end{pmatrix}$
$\theta_1 = 0$ $\theta_2 = 0$	$\theta_1 = \frac{\pi}{2}$ $\theta_2 = \frac{\pi}{2}$	$\theta_1 = \frac{\pi}{4}$ $\theta_2 = \frac{\pi}{4}$	$\theta_1 = -\frac{\pi}{4}$ $\theta_2 = -\frac{\pi}{4}$	$\theta_1 = \frac{\pi}{4}$ $\theta_2 = \frac{\pi}{2}$	$\theta_1 = -\frac{\pi}{4}$ $\theta_2 = \frac{\pi}{2}$

Due to the need of introducing the less mistakes possible while rotating the polarization elements, an automatic setup using motorized precision rotation stage was sought. Owing to automating the system and only having available two Motorized Precision Rotation Stages (PRM1/MZ8 from *Thorlabs* [163]*)*, it is not possible to generate and analyses the 6 desired states. For this reason, it was decided to generate and analyses 11 polarizations states of each. The Mueller polarimeter shown in Figure 30 is calibrated with the obtain the states of polarization illustrated in the Poincaré Sphere in Figure 36.

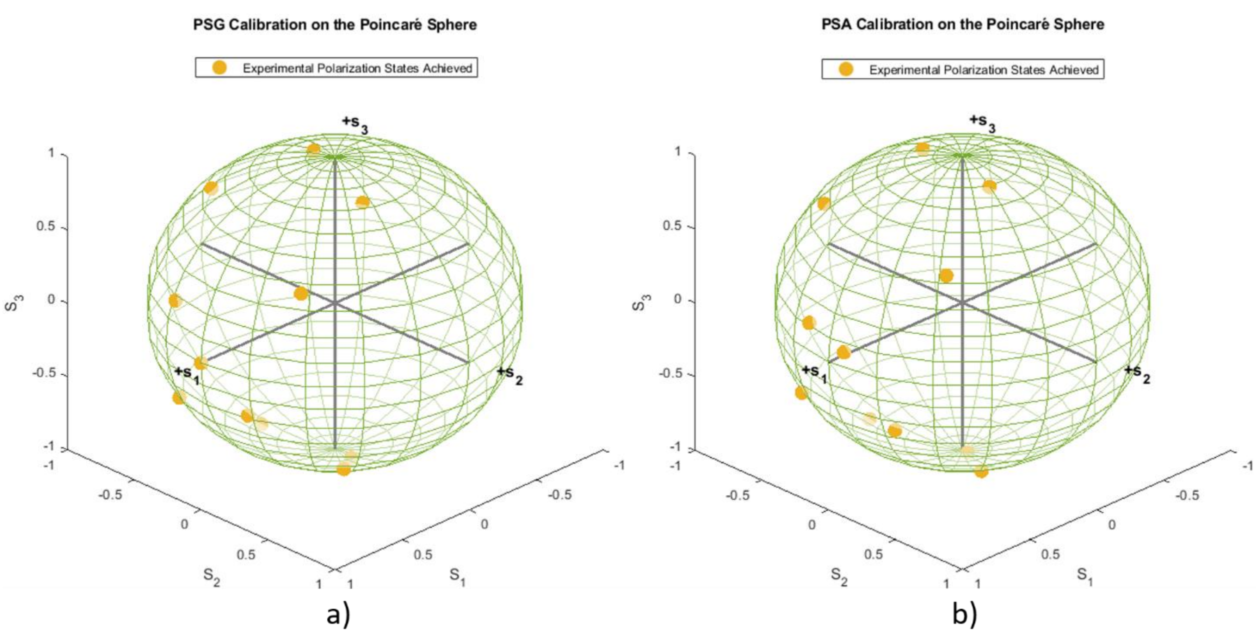

Figure 36.Illustration of the a) PGS and b) PSA experimentally achieved polarization states (yellow), represented in the Poincaré sphere, of the QWP Mueller setup.

The PSG's and PSA's calculated CN is 3.6123. The experimental CNs of this Mueller polarimeter are not close to the best theoretical CN of $\sqrt{3}$ (see section 6.2.5), therefore, we can conclude that this Mueller polarimeter is lacking some precision.

<u>Calibration of Mueller Polarimeter based on LCVRs retarders in section 6.3.1.</u>

In this setup, the incident light beam passes through a LP followed by two LCVRs. As it has been shown in reference [171], the optimal arrangement to generate or analyse any state of polarization is by having the fast axis of the LCVRs displaced at 45° and 0° from the LP's transmission axis, sequentially (see Figure 37). Since LCVRs are, as QWP, also linear retarders, the Mueller matrices associated to these two optical components are $M_{LR}(\theta + 45°, \delta_1)$ and $M_{LR}(\theta + 0°, \delta_2)$, where δ_1 and δ_2 represent their retardances and $\theta + 45°$ and $\theta + 0°$ represent the angle of their fast axis.

Here, to predict and select the PSG and PSA states, a mathematical prediction is made regarding this setup. In ideal conditions, the PSA and PSG calibration Mueller matrix are the same

$$S_{out} = M_{PSG/PSA} \cdot S_{in} = M_{LR}(\theta, \delta_2) \cdot M_{LR}(\theta + 45°, \delta_1) \cdot M_{LP}(\theta) \cdot S_{in} \quad (42)$$

where M_{LP} represents the Mueller matrix of the LP and θ is its transmission angle axis. To simplify the mathematical prediction, θ was placed at 0°.

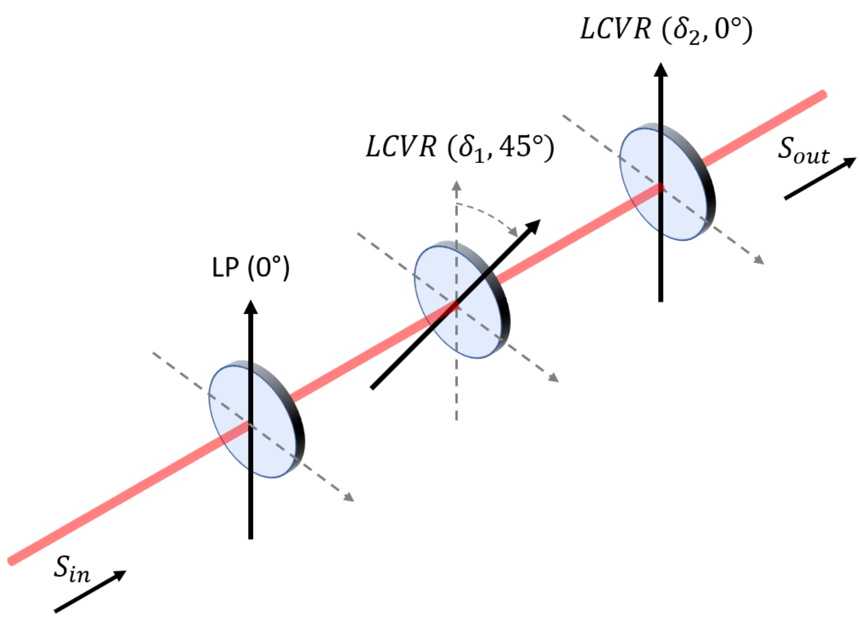

Figure 37. Scheme of a PSG constituted by a linear polarizer (LP) with the transmission axis at 0° followed by two liquid crystal variable retarders (LCVRs) with the fast axis at 45° and 0°, consecutively. δ_1 and δ_2 represent the retardance of both LCVRs.

Then,

$$S_{out} = \begin{bmatrix} 1 & 0 & 0 & 0 \\ 0 & 1 & 0 & 0 \\ 0 & 0 & \cos\delta_2 & \sin\delta_2 \\ 0 & 0 & -\sin\delta_2 & \cos\delta_2 \end{bmatrix} \cdot \begin{bmatrix} 1 & 0 & 0 & 0 \\ 0 & \cos\delta_1 & 0 & -\sin\delta_1 \\ 0 & 0 & 1 & 0 \\ 0 & \sin\delta_1 & 0 & \cos\delta_1 \end{bmatrix} \cdot \frac{1}{2} \begin{bmatrix} 1 & 1 & 0 & 0 \\ 1 & 1 & 0 & 0 \\ 0 & 0 & 0 & 0 \\ 0 & 0 & 0 & 0 \end{bmatrix} S_{in} \Leftrightarrow$$

$$\Leftrightarrow S_{out} = \frac{1}{2} \begin{pmatrix} S_{in,0} \\ S_{in,1}\cos\delta_1 \\ S_{in,1}\sin\delta_1\sin\delta_2 \\ S_{in,1}\sin\delta_1\cos\delta_2 \end{pmatrix} \tag{43}$$

In theory, if the input state of polarization is normalized, $S_{in} = (1 \quad 1 \quad 0 \quad 0)^T$, Eq. (43) is rewritten as

$$S_{out} = \frac{1}{2} \begin{pmatrix} 1 \\ \cos\delta_1 \\ \sin\delta_1\sin\delta_2 \\ \sin\delta_1\cos\delta_2 \end{pmatrix} \tag{44}$$

This means that to generate the desired calibration states in an ideal optical system, one can look at the Table 5 as a screenplay.

Table 5. Calibration states summary for the Mueller polarimeter using LCVR and LPs. The values were obtained from Eq. (44).

HLP $\begin{pmatrix} 1 \\ 1 \\ 0 \\ 0 \end{pmatrix}$	VLP $\begin{pmatrix} 1 \\ -1 \\ 0 \\ 0 \end{pmatrix}$	LP+45° $\begin{pmatrix} 1 \\ 0 \\ 1 \\ 0 \end{pmatrix}$	LP-45° $\begin{pmatrix} 1 \\ 0 \\ -1 \\ 0 \end{pmatrix}$	RCP $\begin{pmatrix} 1 \\ 0 \\ 0 \\ 1 \end{pmatrix}$	LCP $\begin{pmatrix} 1 \\ 0 \\ 0 \\ -1 \end{pmatrix}$
$\delta_1 = 0$ $\delta_2 = 0$	$\delta_1 = \frac{\pi}{2}$ $\delta_2 = \frac{\pi}{2}$	$\delta_1 = \frac{\pi}{4}$ $\delta_2 = \frac{\pi}{4}$	$\delta_1 = -\frac{\pi}{4}$ $\delta_2 = -\frac{\pi}{4}$	$\delta_1 = \frac{\pi}{4}$ $\delta_2 = \frac{\pi}{2}$	$\delta_1 = -\frac{\pi}{4}$ $\delta_2 = \frac{\pi}{2}$

After analysing the best theoretical PSG and PSA polarization states, the Mueller polarimeter shown in Figure 34 is calibrated to obtain the states of polarization presented in Table 5.

Due to the LCVRs supplier does not provide a prediction of the retardance versus voltage to the wavelength in use, firstly a huge series of combinations of different applied voltages in the LCVRs was detected with the *Thorlabs* [163] polarimeter to choose the polarization states that best represent the desired ones (see Table 5). The chosen states are indicated in

Table 6 and illustrated in the Poincaré Sphere in Figure 38. The PSG's calculated CN is 1.7507 and the PSA's CN is 1.8179. As stated above, the best theoretical CN is $\sqrt{3} \approx 1.7321$ (see section 6.2.5), i.e., our experimental CNs are close to the theoretically expected. Therefore, we can conclude that our Mueller polarimeter is precise and accurate.

Table 6. PSG and PSA calibration states for the Mueller Polarimeter based on LCVRs retarders. The colours range from blue to red to describe the changes in the electric field with the propagator.

Calibration Theoretical Polarization State	**Calibration Experimental Polarization States**		**Polarization Ellipse**	
	PSG	**PSA**	**PSG**	**PSA**
HLP $\begin{pmatrix} 1 \\ 1 \\ 0 \\ 0 \end{pmatrix}$	$\begin{pmatrix} 1.0000 \\ 0.9997 \\ 0.0254 \\ 0.0013 \end{pmatrix}$	$\begin{pmatrix} 1.0000 \\ 0.9998 \\ -0.0201 \\ 0.0009 \end{pmatrix}$	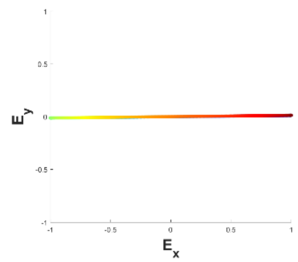	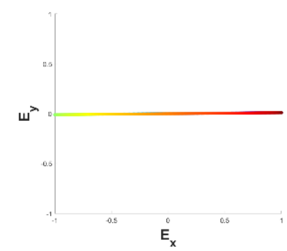
VLP $\begin{pmatrix} 1 \\ -1 \\ 0 \\ 0 \end{pmatrix}$	$\begin{pmatrix} 1.0000 \\ -0.9999 \\ -0.0108 \\ 0.0028 \end{pmatrix}$	$\begin{pmatrix} 1.0000 \\ -0.9880 \\ -0.1526 \\ 0.0238 \end{pmatrix}$	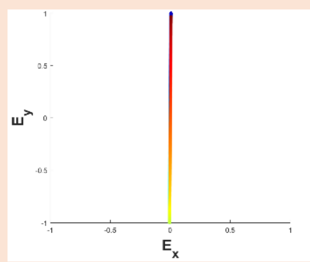	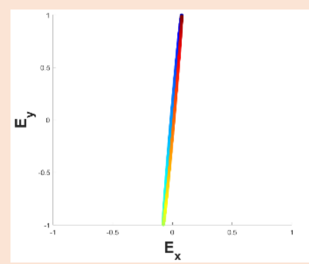
LP+45 $\begin{pmatrix} 1 \\ 0 \\ 1 \\ 0 \end{pmatrix}$	$\begin{pmatrix} 1.0000 \\ -0.0021 \\ 1.0000 \\ 0.0040 \end{pmatrix}$	$\begin{pmatrix} 1.0000 \\ 0.0044 \\ 1.0000 \\ -0.0008 \end{pmatrix}$	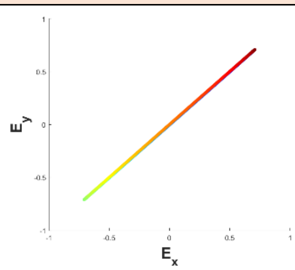	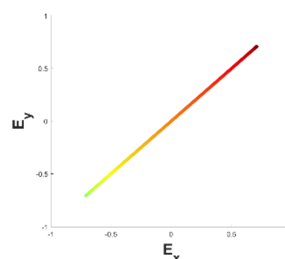
LP-45 $\begin{pmatrix} 1 \\ 0 \\ -1 \\ 0 \end{pmatrix}$	$\begin{pmatrix} 1.0000 \\ -0.0040 \\ -1.0000 \\ -0.0081 \end{pmatrix}$	$\begin{pmatrix} 1.0000 \\ 0.0018 \\ -1.0000 \\ 0.0039 \end{pmatrix}$	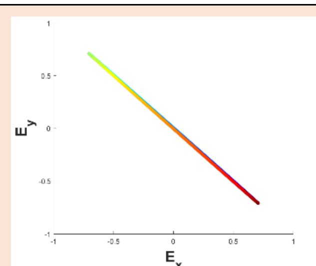	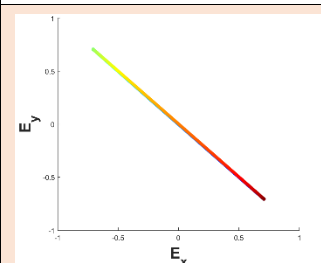

Calibration Theoretical Polarization State	Calibration Experimental Polarization States		Polarization Ellipse	
	PSG	**PSA**	**PSG**	**PSA**
RCP $\begin{pmatrix} \mathbf{1} \\ \mathbf{0} \\ \mathbf{0} \\ \mathbf{1} \end{pmatrix}$	$\begin{pmatrix} 1.0000 \\ -0.0009 \\ 0.0019 \\ 1.0000 \end{pmatrix}$	$\begin{pmatrix} 1.0000 \\ -0.0101 \\ 0.0088 \\ 0.9999 \end{pmatrix}$	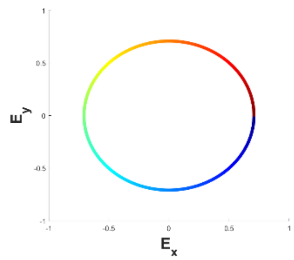	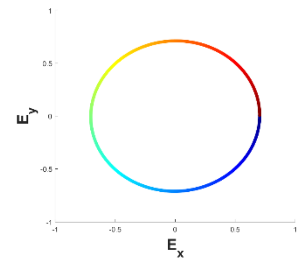
LCP $\begin{pmatrix} \mathbf{1} \\ \mathbf{0} \\ \mathbf{0} \\ \mathbf{-1} \end{pmatrix}$	$\begin{pmatrix} 1.0000 \\ 0.0025 \\ 0.0004 \\ -1.0000 \end{pmatrix}$	$\begin{pmatrix} 1.0000 \\ 0.0097 \\ -0.0766 \\ -0.9970 \end{pmatrix}$	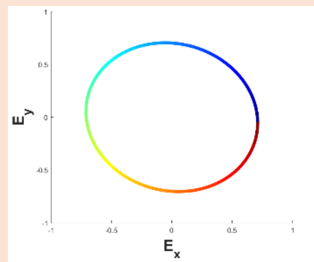	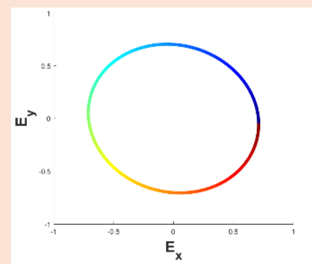

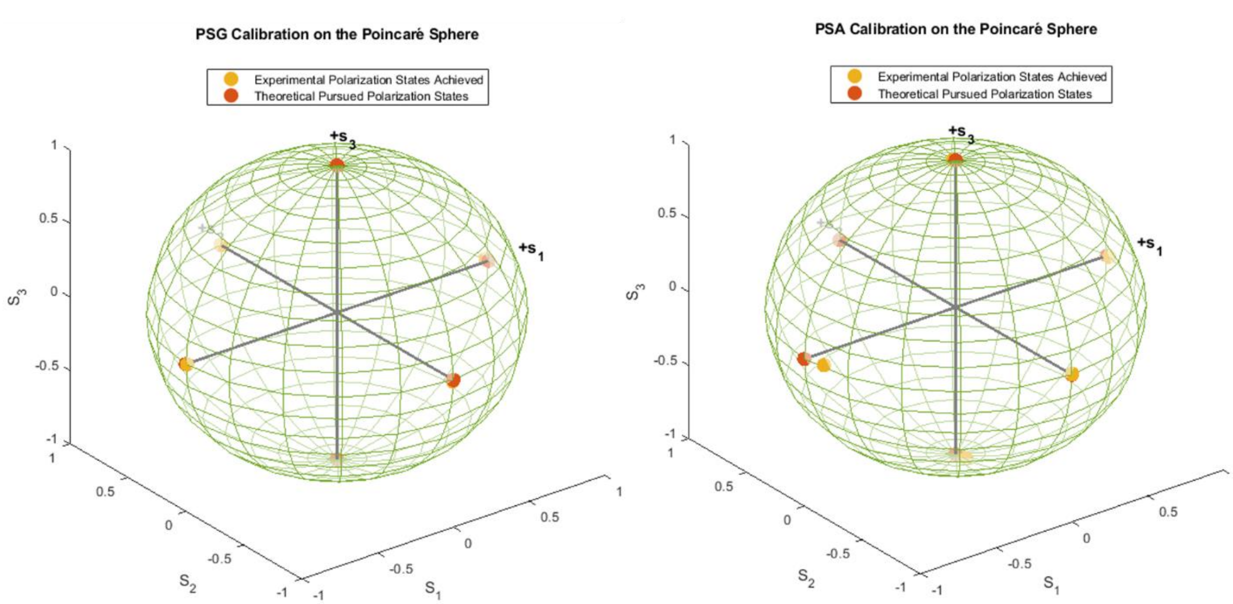

a) b)

Figure 38. Illustration of the a) PGS and b) PSA theoretically pursued (orange) and experimentally achieved (yellow) polarization states, represented in the Poincaré sphere, , with the LCVR Mueller setup.

Although this system presents a smaller influence on systematic errors, it is a system that needs to be calibrated daily. To this end, the calibrated system is used in transmission to measure air, a LP or a QWP.

This measurement is remade every day, so that the overnight changes in the system are determined and corrected by comparing the current measurement with the first one made.

6.4. Experimental measurements

After calibrating the Mueller polarimeter, the present setup was designed to analyse the possibilities of using polarized light to distinguish different materials. For this purpose, materials like wood, metallic and non-metallic car paints, traffic signals with and without retroreflectors, leaves and clothing fabrics were targets of evaluation of the experimental systems. As different materials have different reflectance, the camera's exposure time to each sample was adapted so that enough light data was detected but also ensure that the pixel detectors did not saturated. Each pixel detector is detecting an approximated area of 0,05 x 0,05 cm. One sample of each referred material was selected and its RGB picture is represented in Figure 39, and the experimental Mueller matrices of these samples are represented from Figure 40 to Figure 47.

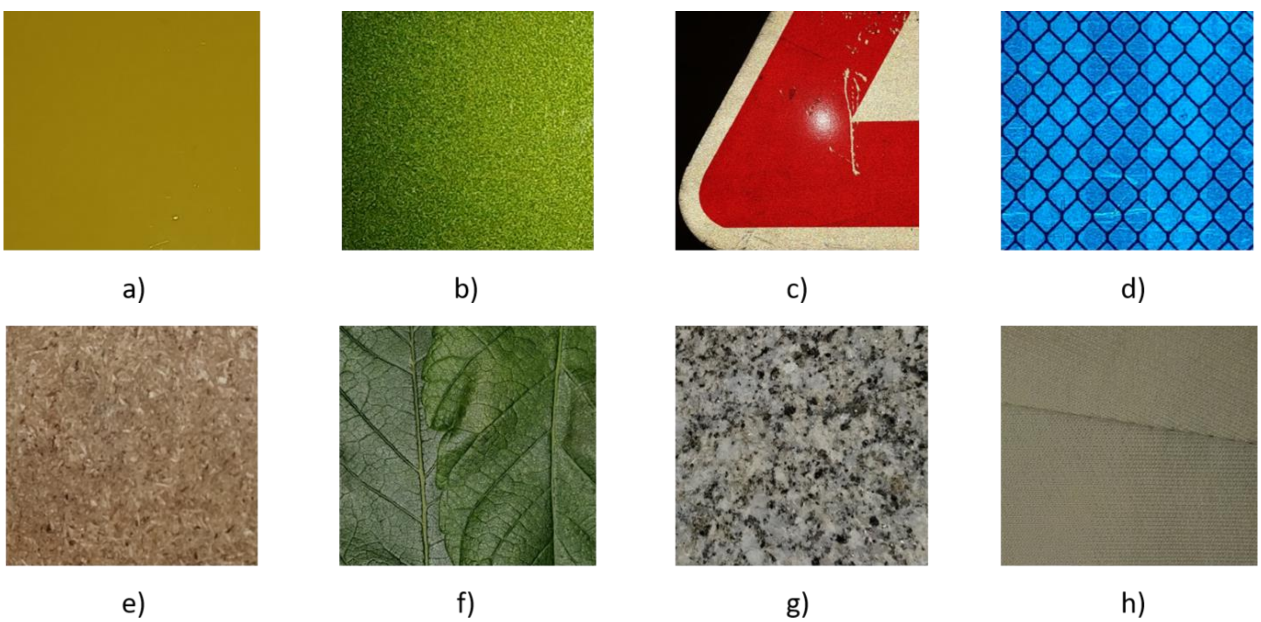

Figure 39. RBG pictures of the polarimetric characterized samples: a) non-metallic car paint, b) metallic car paint, c) traffic signal, d) retroreflector traffic signal, e) agglomerated wood, f) leaves, g) rock (granite) and h) clothing fabric (cotton).

Several measurements were made by using the rotating and variable retarder Mueller polarimeters (described in sections 6.3.1 and 6.3.2, respectively). As we have a great amount of measurements with the setup using QWPs, it was decided that the study was going to be proceed with the results acquired from it. However, some measurements acquired from the LCVR setup measurements were also shown in this chapter due to its greater accuracy and precision. Nevertheless, the already Mueller matrices determined by the both polarimeters are being used in present and future works in the project where this thesis is involved.

Following the polarimetric measurement principle described in section 6.2.4, the Mueller matrix of each sample shown in Figure 39 is calculated from a set of intensity images obtained from different combinations of the PSG and PSA. The experimental Mueller matrices are shown in Figure 40 - Figure 47. The illuminated area of each sample is $40\ mm\ \times 40\ mm$ and the SRA is $20°$. Note that the SRA is the angle made by the detector and specular reflection (see section 6.3.1).

The elements of each experimental Mueller matrix are normalized by the same pixel of the M_{00} element (see Eq.(31)), which represents the light intensity variation on the sample (pixelwise normalization). Doing this normalization, all 16 elements of the Mueller matrix vary from -1 to 1 allowing qualitative comparisons only considering changes in polarization, excluding the exposure time dependency, i.e., reflectivity influence. Nevertheless, the element M_{00} was the only element that was only normalized by its own maximum pixel value, so that we can compare the intensity distribution of each sample.

As one can observe from Figure 40 - Figure 47, different materials present different polarimetric responses. In addition, as expected, retro-reflective and non-retro-reflective same coloured traffic signals do not have a similar polarimetric response.

More than that, Figure 48 also allows deducing that differently coloured samples (in the visible spectrum) of the same material, that present different reflectance in the infra-red spectrum (1550 nm), might present an identical polarimetric response. The reflectance variations between samples were compensated by changing the exposure time of the InGaAS camera.

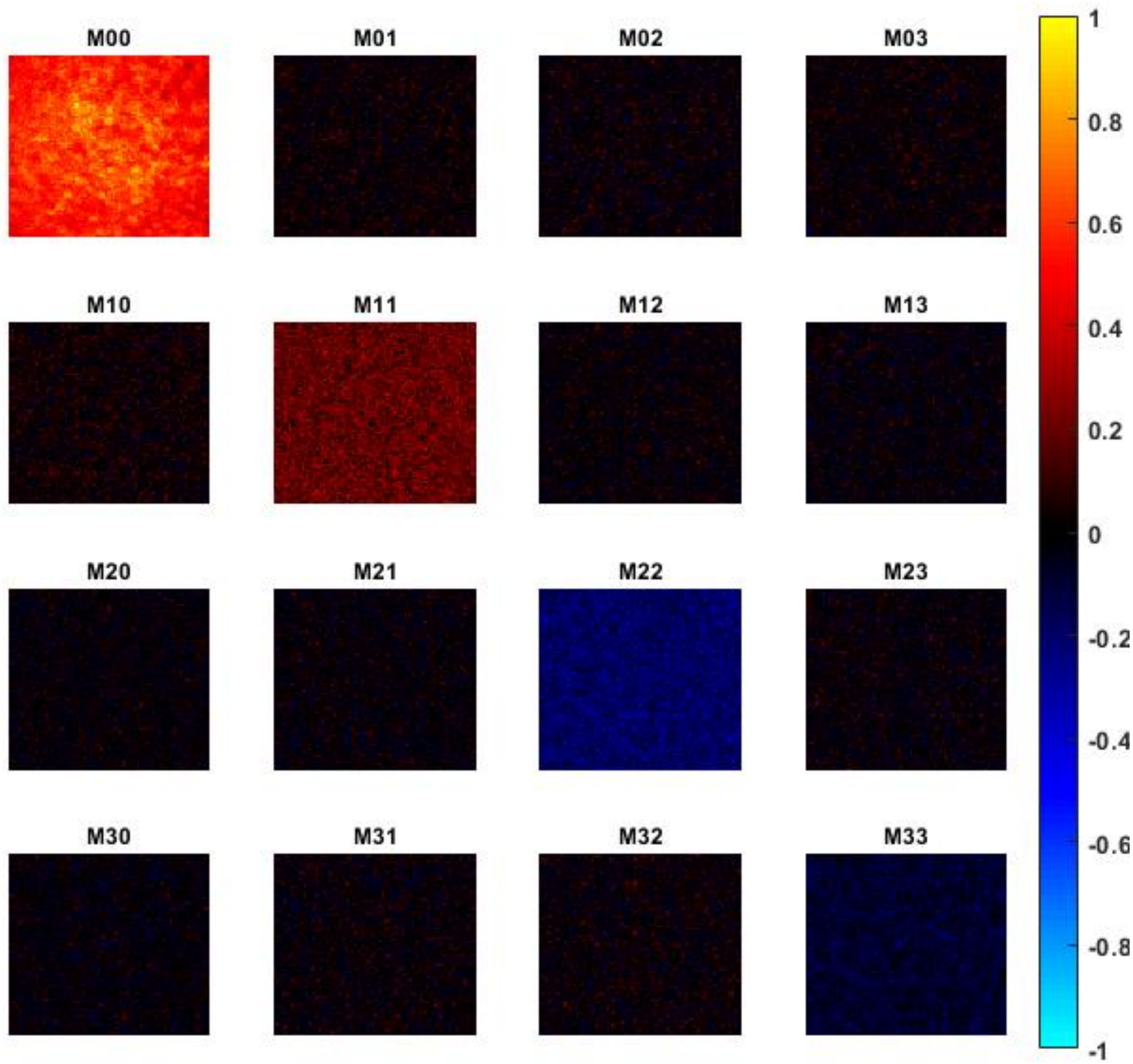

Figure 40. Normalized Mueller matrix image at 20° of SRA for 1550 nm of a non-metallic car paint (SUNNY MELON), determined with the LCVRs Mueller setup.

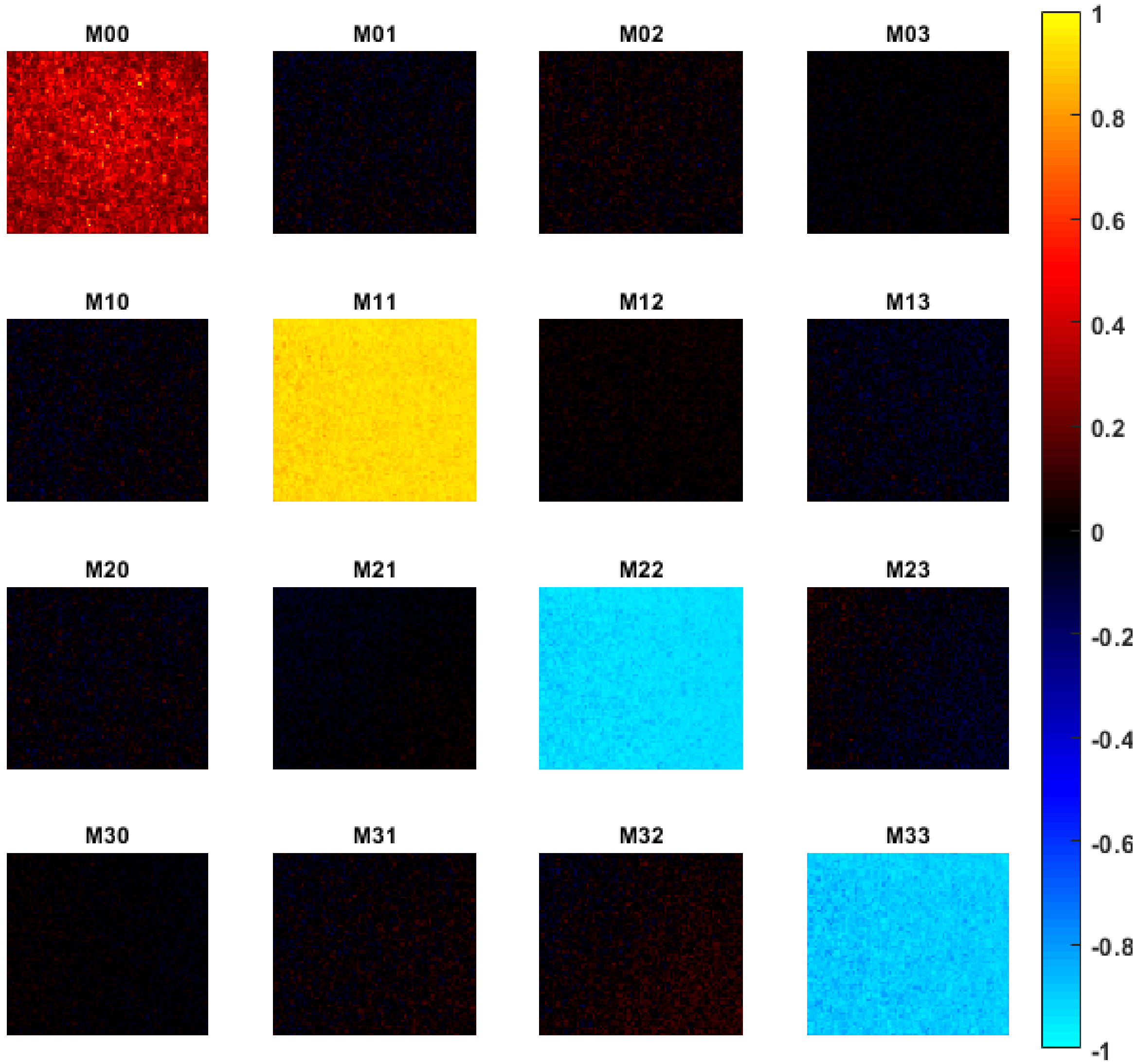

Figure 41. Normalized Mueller matrix image at 20° of SRA for 1550 nm of a metallic car paint (LEMONGRASS-MET) , determined with the LCVRs Mueller setup.

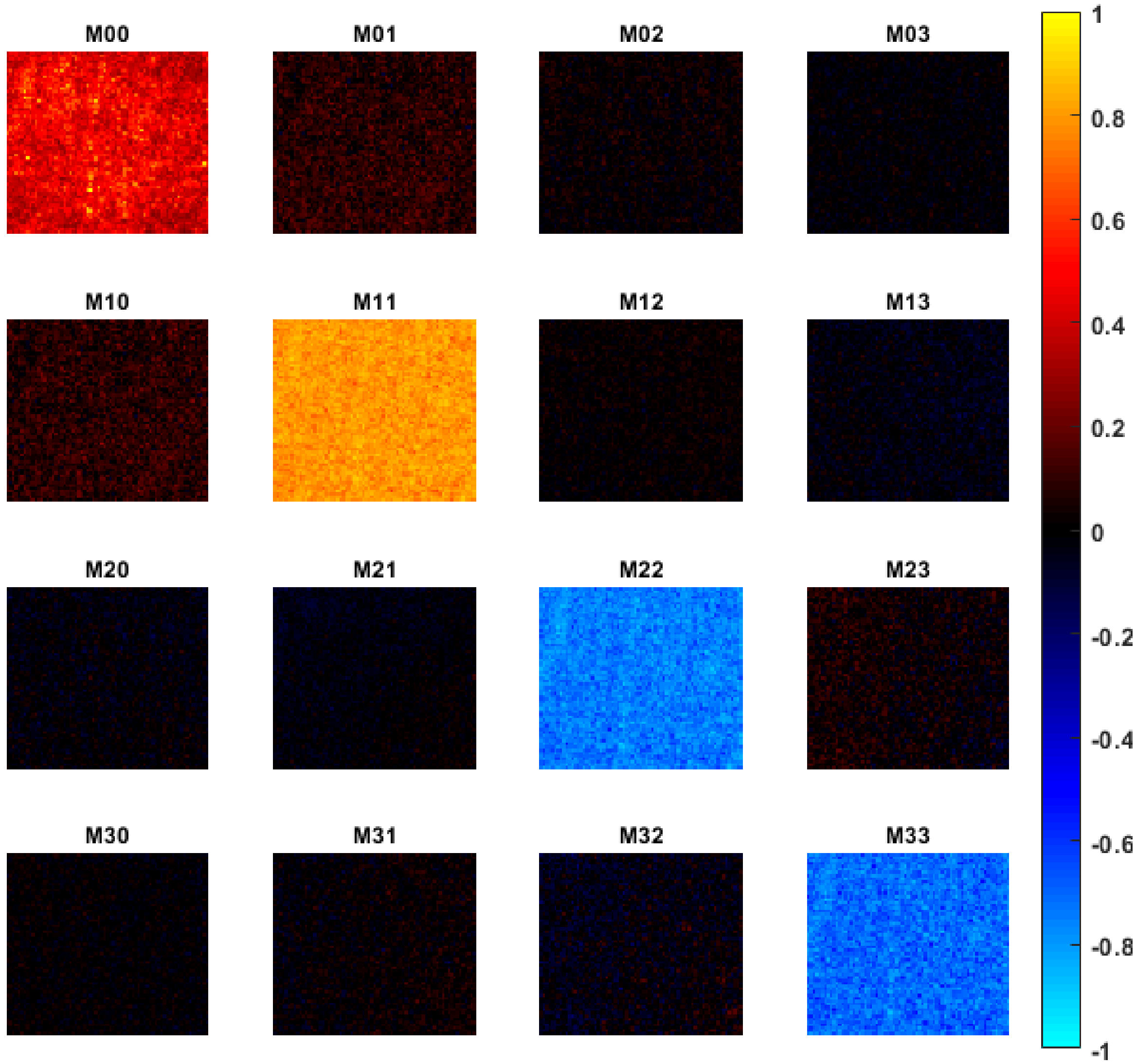

Figure 42. Normalized Mueller matrix image at 20° of SRA for 1550 nm of a regular traffic signal, determined with the LCVRs Mueller setup.

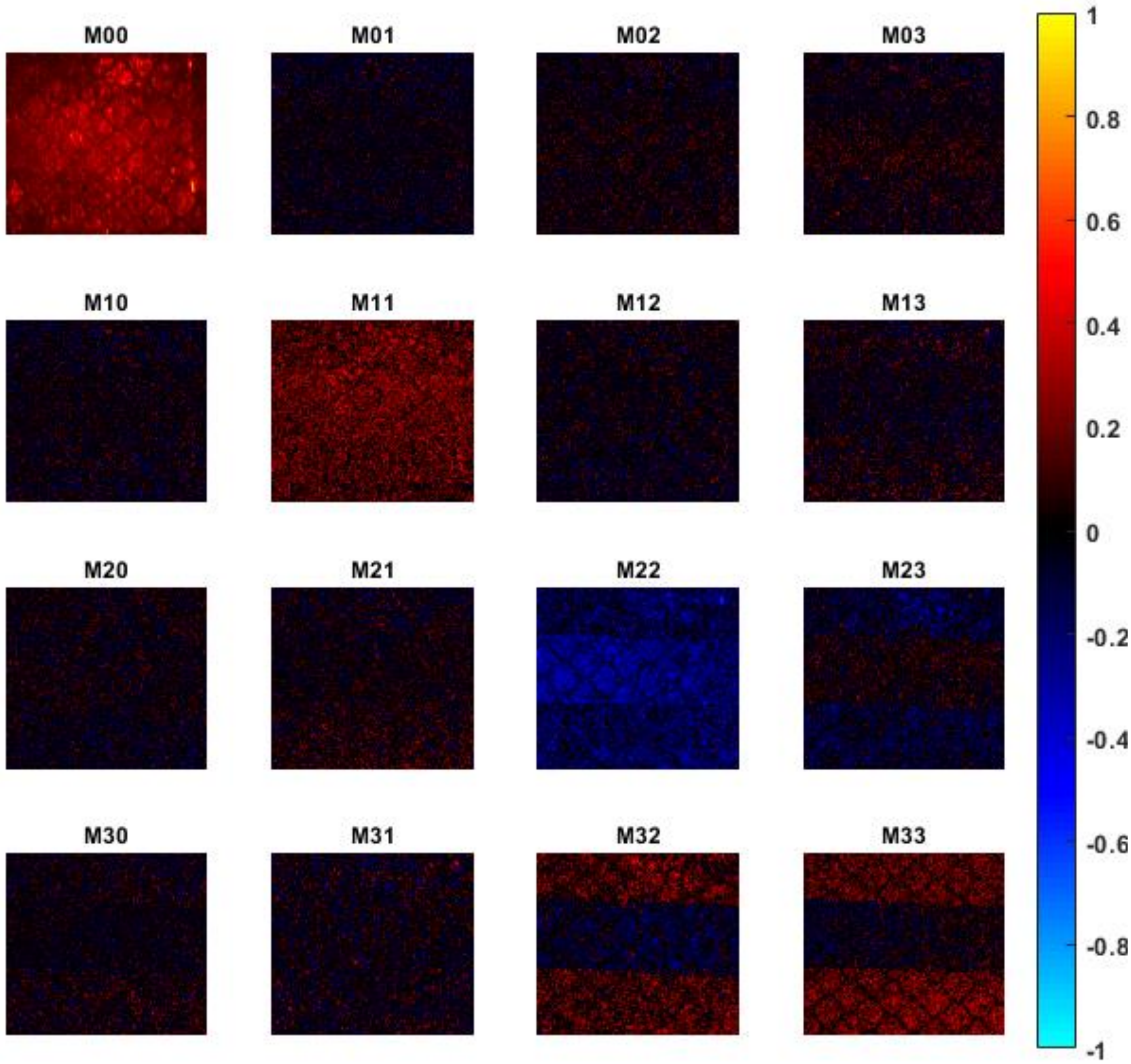

Figure 43. Normalized Mueller matrix image at 20° of SRA for 1550 nm of a retro-reflector traffic signal, determined with the LCVRs Mueller setup.

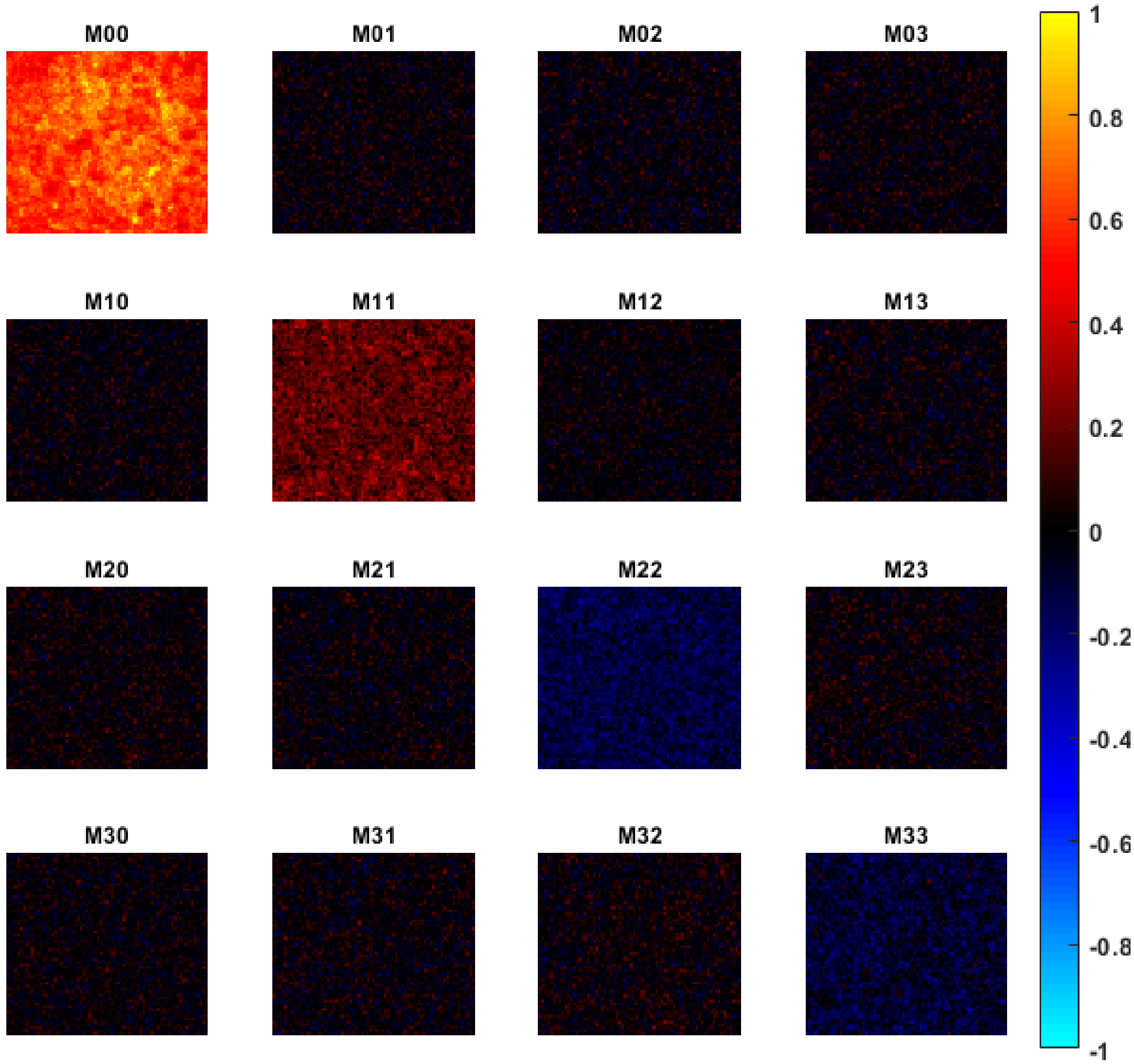

Figure 44. Normalized Mueller matrix image at 20° of SRA for 1550 nm of agglomerated wood, determined with the LCVRs Mueller setup.

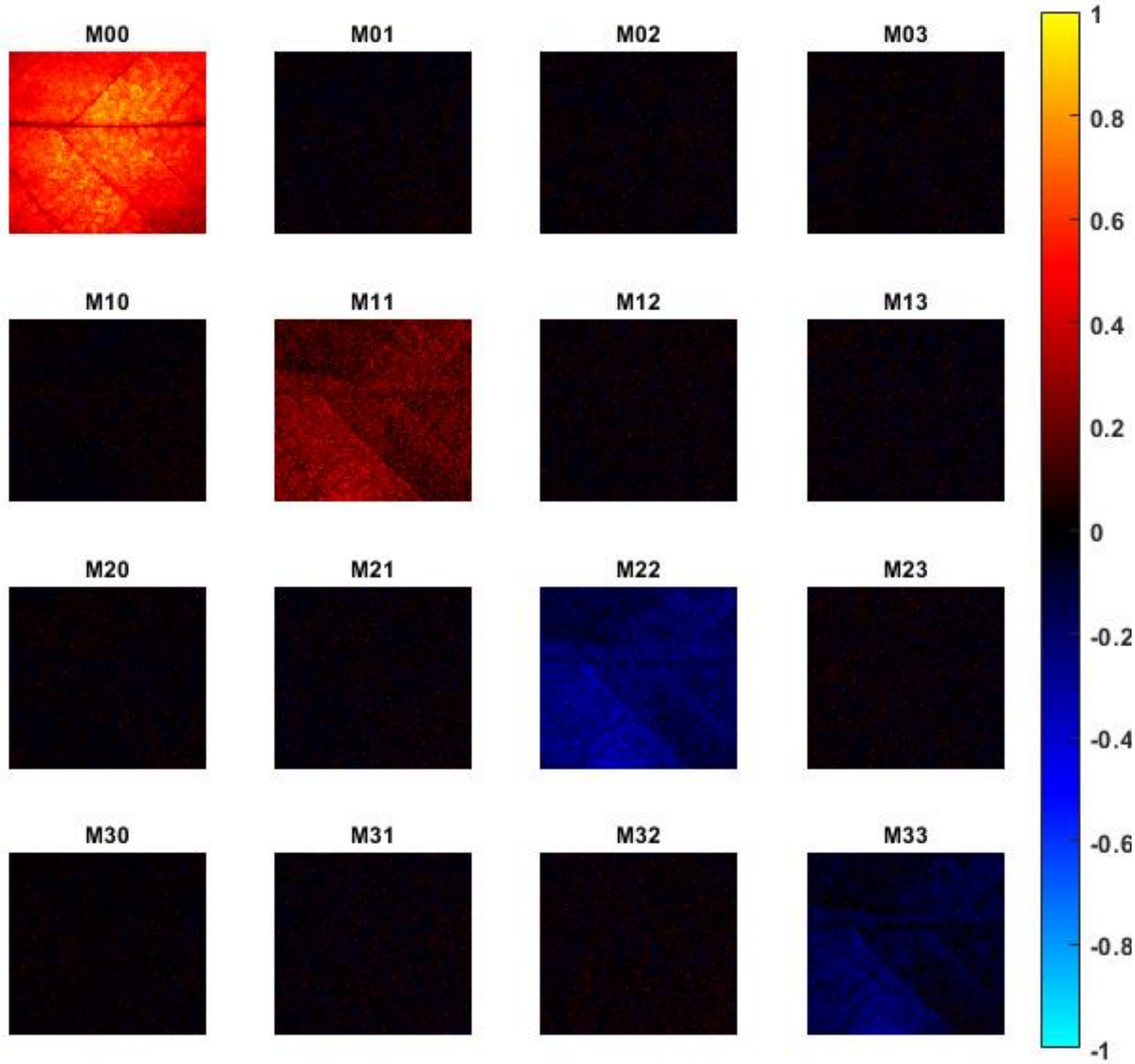

Figure 45. Normalized Mueller matrix image at 20° of SRA for 1550 nm of leaves, determined with the LCVRs Mueller setup.

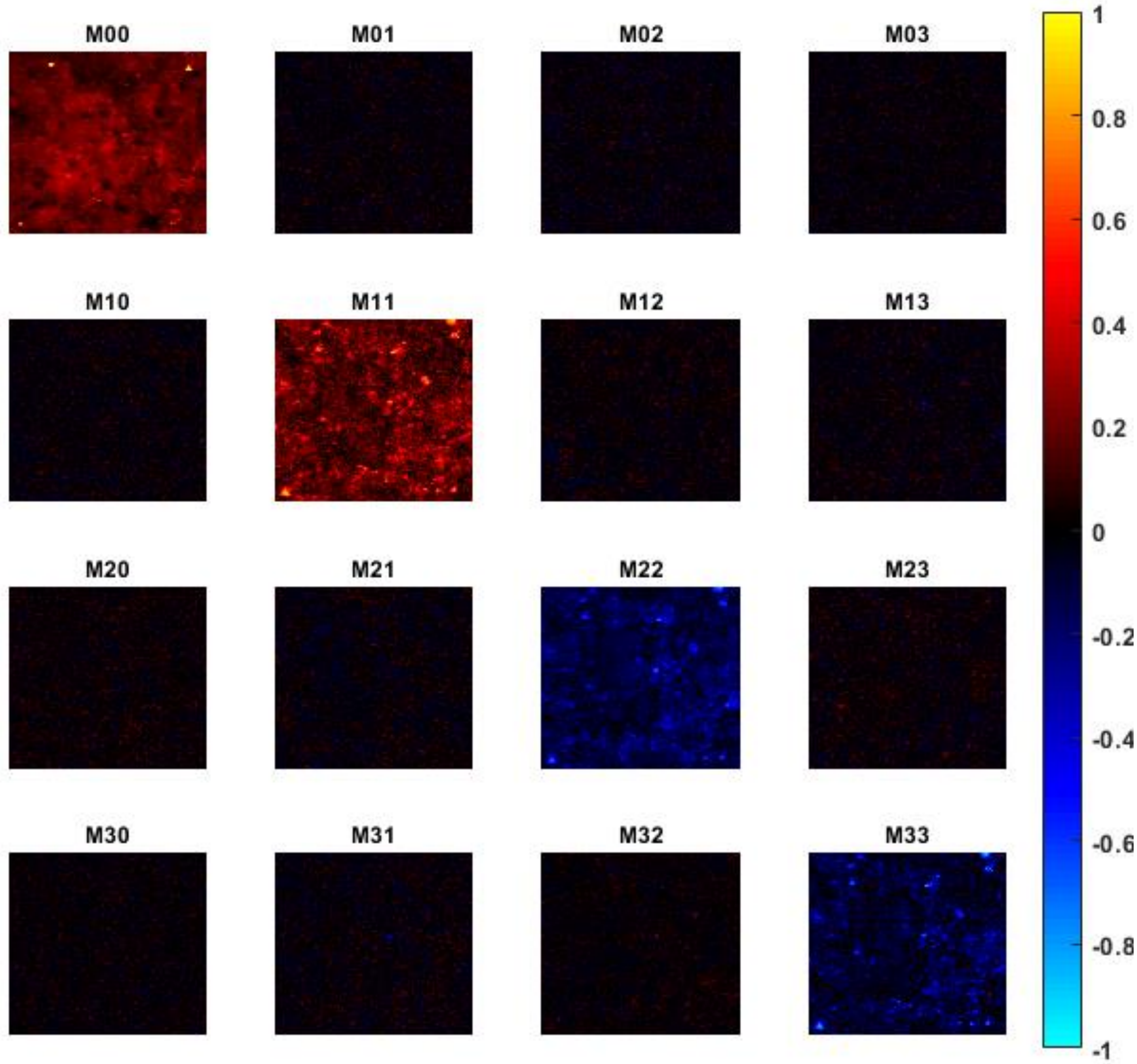

Figure 46.Normalized Mueller matrix image at 20° of SRA for 1550 nm of a rock (granite) , determined with the LCVRs Mueller setup.

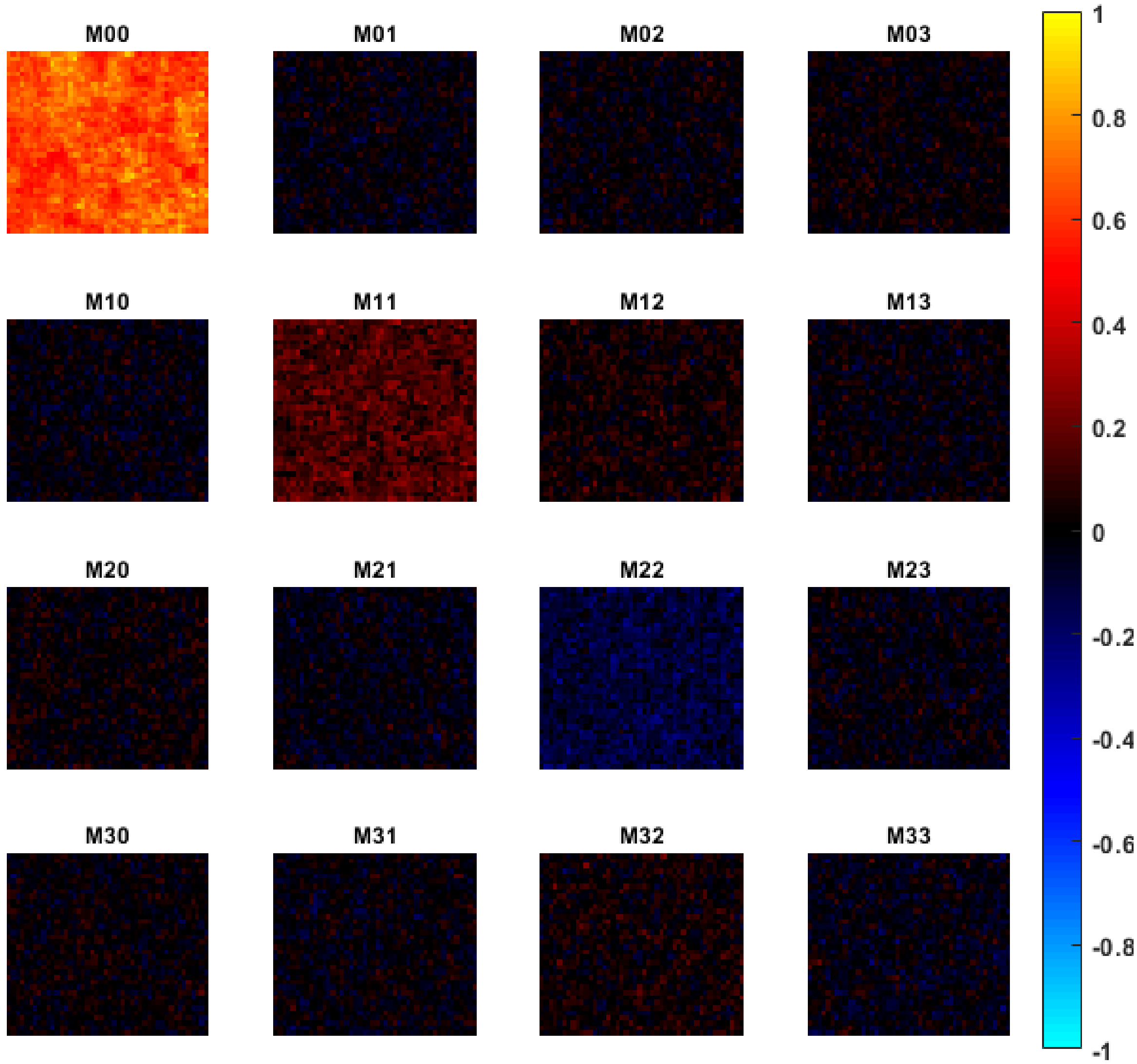

Figure 47. Normalized Mueller matrix image at 20° of SRA for 1550 nm of clothing fabric (cotton) , determined with the LCVRs Mueller setup.

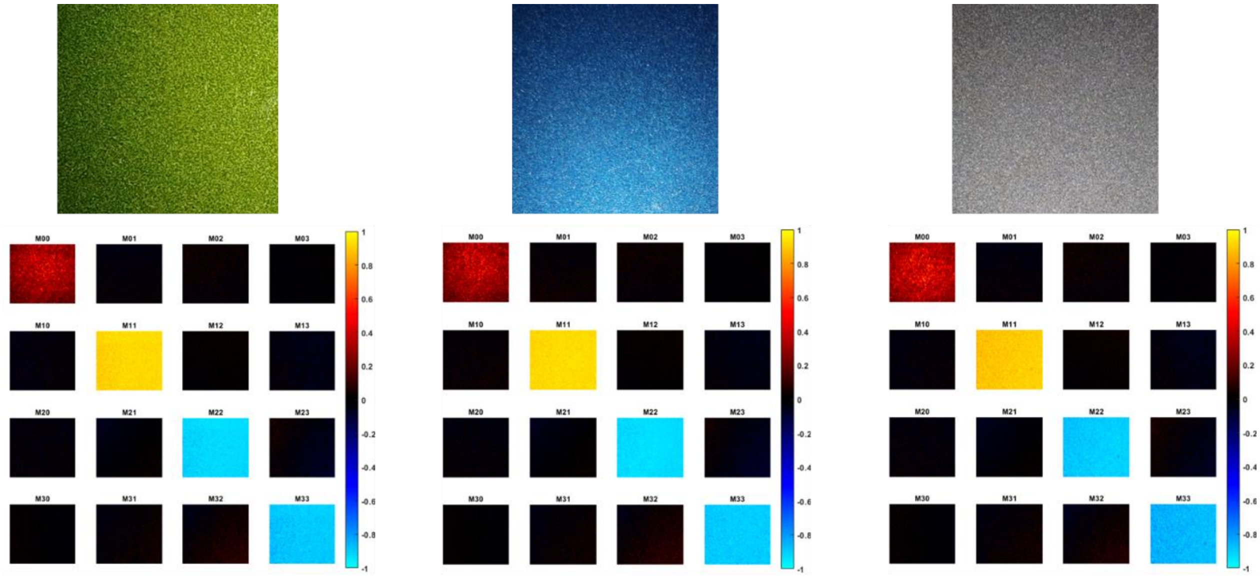

a) b) c)

Figure 48. RGB picture and normalized Mueller matrix image at 20° of SRA for 1550 nm of a) LEMONGRASS-MET., b) BLUEHIT and c) REFLEXSILBER metallic car paints, determined with the LCVRs Mueller setup.

Now that polarimetric differences were acknowledge, the dependence of the Mueller matrix on the SRA was studied. To this purpose, a LiDAR-like behaviour was considered. As referred in section 4.1.4, LiDARs rely on detectors and, in order to mimic its technology restrains and providing more accurate data, the images' pixels were averaged. It was studied that the spot-size of different LiDARs (from Velodyne [172], LeddarTech [173], Quanergy [174], Valeo [175], Ouster [176],...) variates as a function of the distance due to the beams divergence (the spot-size area can change from $10 \times 10\ \mathrm{mm}^2$ to $300 \times 200\ \mathrm{mm}^2$), for this reason, as a preliminary stage, we decided to use a pixel window of $40 \times 40\ \mathrm{mm}^2$, which is comprised between the expected illuminating area. The single Mueller matrix of each sample was determined by averaging the entire illuminated area. The Mueller matrices of multiple samples were measured at 11 different angles of incidence, equally spaced 10 by 10 degrees, varying from –50° to +50° (in the clock-wise direction). The obtained averaged results are presented in Figure 49.

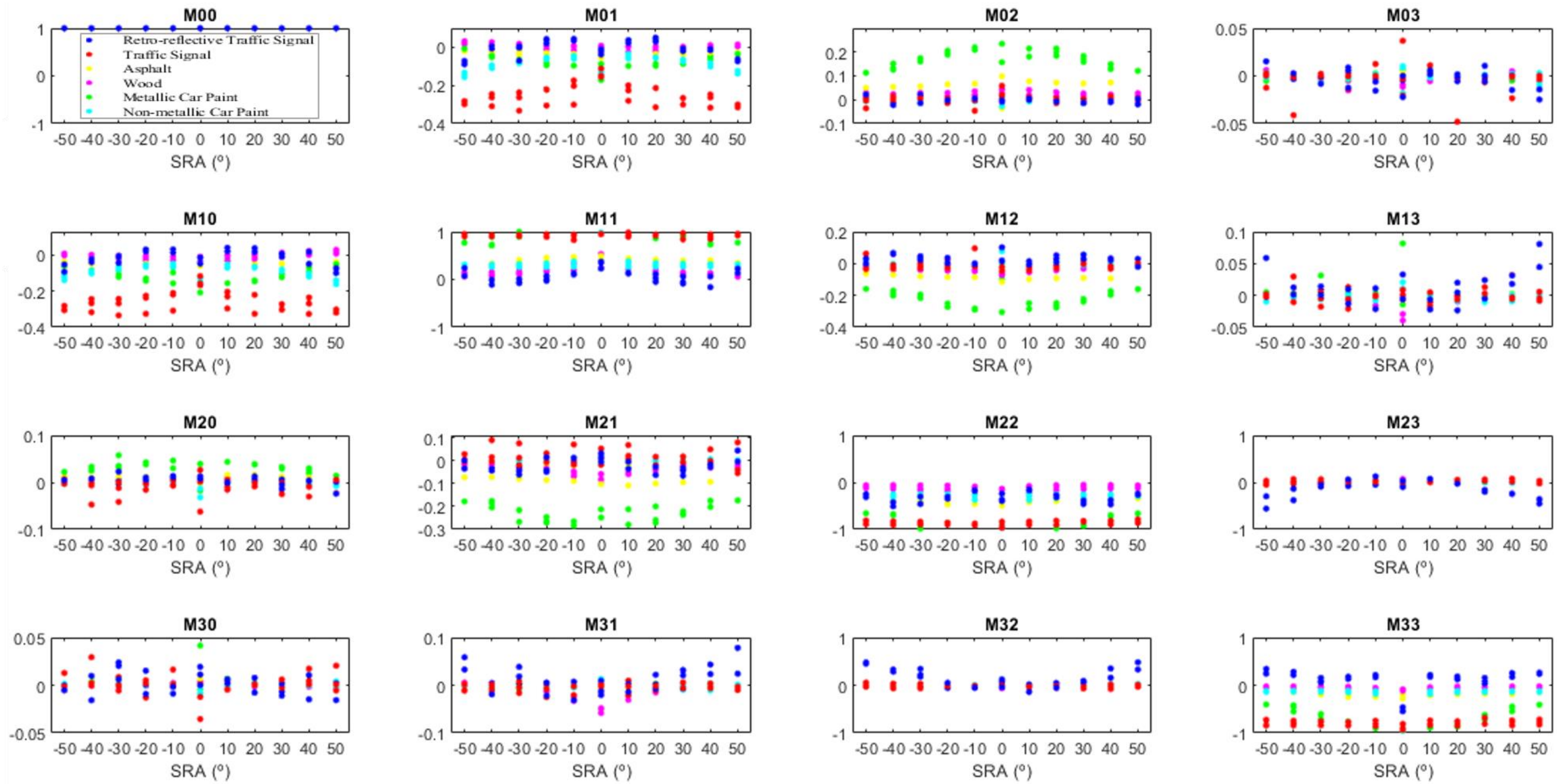

Figure 49. SRA (°) dependence on the normalized averaged Mueller matrix at 1550 nm for multiple samples of each materials: retro-reflective traffic signals (blue), traffic signals without retro-reflectance properties (red), Asphalt (yellow), Wood (magenta), metallic and non-metallic car paints (green and cyan, respectively), determined with the QWP Mueller setup.

From Figure 49, it is deduced that not only the polarization properties have a dependence on the SRA, but also that similar materials have similar quantitative responses. Figure 49 also allows understanding that some Mueller matrix elements are more important than others to distinguish different materials, as for example the diagonal elements M_{11}, M_{22} and M_{33}. After concluding that there are Mueller elements more suitable to distinguish materials, some combinations of three Mueller matrix components were plotted in different three-dimensional spaces (see Figure 50).

From the representations in Figure 50, it is deducible that small changes in only one Mueller element can represent a significant change in a three-dimensional space of Mueller elements coordinates, allowing a better material discrimination. Although materials discrimination is clearly possible using only three Mueller elements, some Mueller components, as referred before, are more suitable than others to this end. By Figure 50, one can clearly understand that the angle dependency does not add relevant distinction for material classification (Figure 50 a) and b)), likewise the selected elements represented in Figure 50 c) and d) does not provide as good classification as Figure 50 e) and f), since, in the last, materials are distanced from each other. For that reason, one has to choose the elements that maximize the distance between different material groups. From our preliminary conclusions, it is plausible that the diagonal matrix elements have a greater importance (see Figure 49). Due to the potential of polarimetry observed from the measured samples, this study has not come to an end, meaning that more samples are being measured daily and some Mueller parameters might become relevant. The idea is to analyse more samples, in order to deepen more on the best Mueller coefficients. Nevertheless, from the obtained results, we can clearly differentiate between the measured materials, by using the proposed 3D spaces in Figure 50.

One might also extrapolate that material discrimination might enhance by using more than three Mueller matrix coefficients. Note that, in Figure 50, greater differences between materials are observed even without representing the SRA. Figure 50 allows deducing that, although the polarization properties depend on the SRA, the knowledge of the SRA might be unnecessary.

After realizing that some elements show a greater relevance to material classification, a study was made to determine the dependence of the relevant elements on the M_D, M_R and M_Δ matrices, and on criteria as diattenuation $|D|$ and polarizance $|P|$ (see chapter 6.2.6). Note that, the decomposition of the Mueller matrix allows a further and simple discussion of the type of polarimetric response.

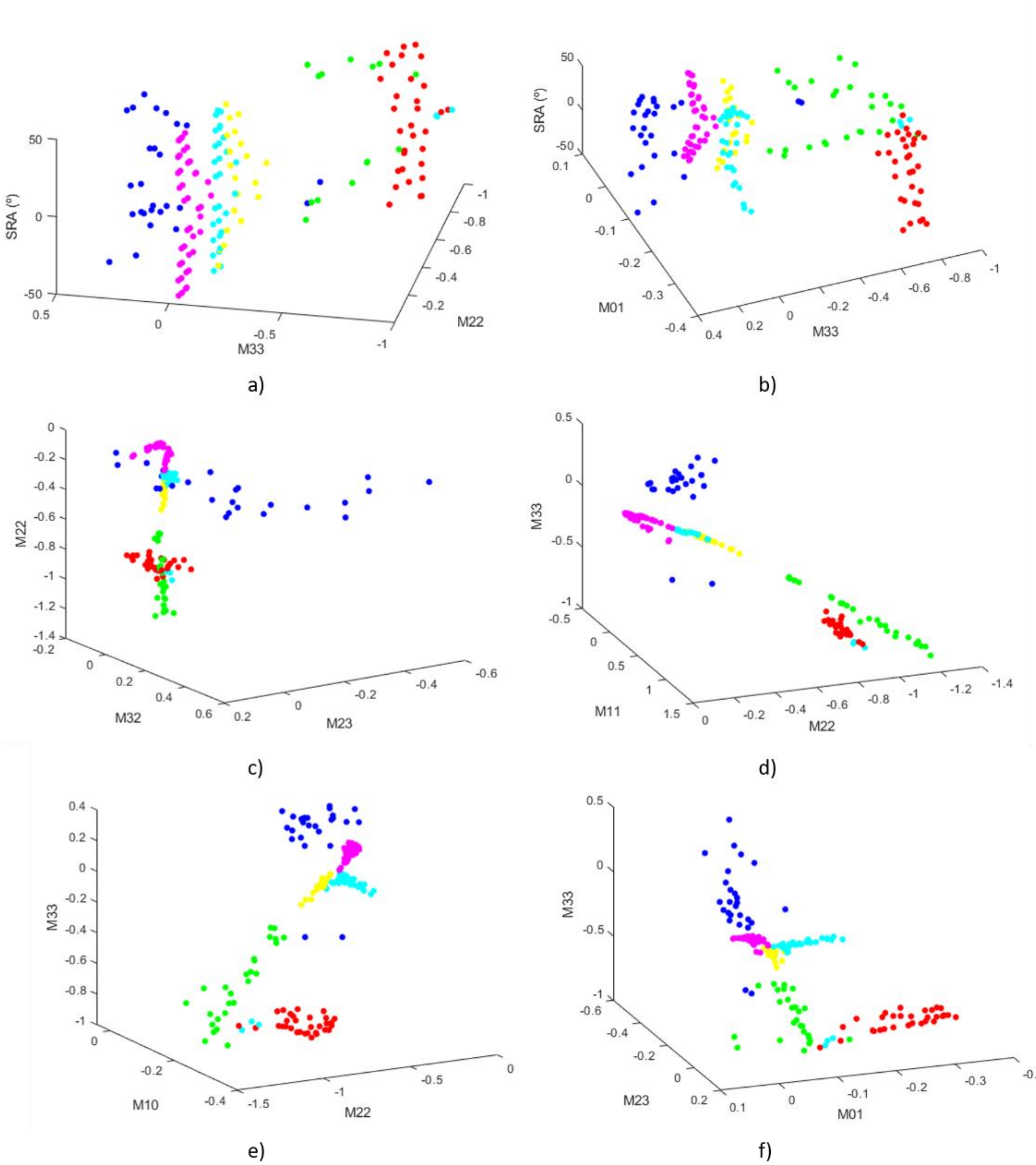

Figure 50. Chosen Mueller matrix components and sample rotation angle, SRA (°), represented in a three-dimensional space of multiple samples of each material: retro-reflective traffic signals (blue), traffic signals without retro-reflectance properties (red), asphalt (yellow), wood (magenta), metallic and non-metallic car paints (green and cyan, respectively). The Mueller components were determined with the QWP Mueller setup.

Firstly, the diattenuation and the polarizance were calculated, and then, they were plotted in Figure 51. As expected, due to the Mueller matrix having a quite symmetric behaviour [155], their diattenuation and polarizance have to be quite similar too.

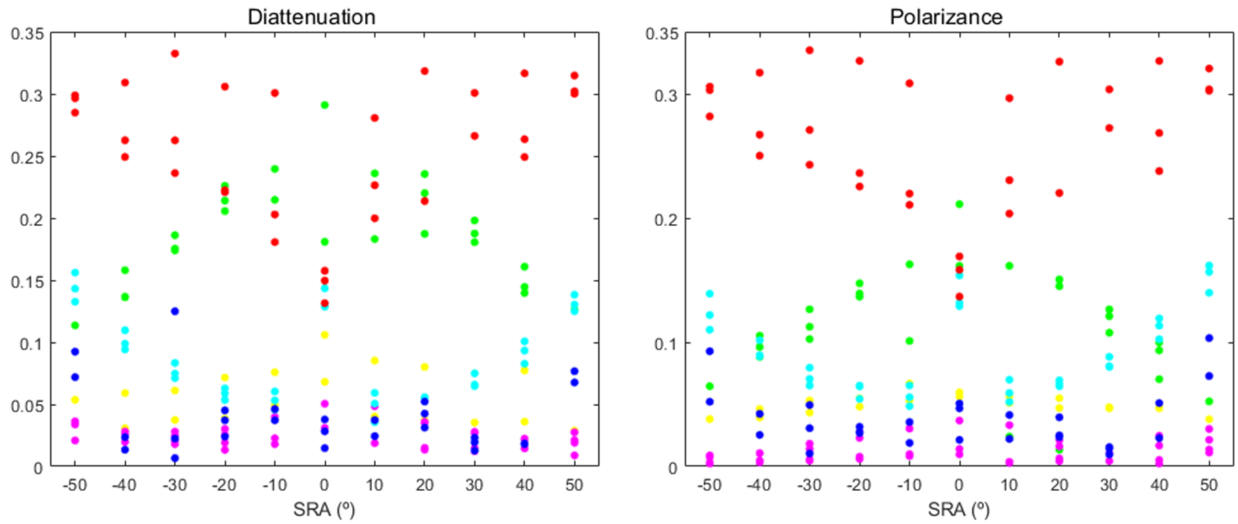

(a) (b)

Figure 51. Diattenuation (a) and polarizance (b) norm dependence on the SRA for the Mueller matrices shown in Figure 49: retro-reflective traffic signals (blue), traffic signals without retro-reflectance properties (red), Asphalt (yellow), Wood (magenta), metallic and non-metallic car paints (green and cyan, respectively). The components were determined with the QWP Mueller setup.

Now, a qualitatively study was then made to better understand the polarization changes that every group of materials presents, i.e. depolarization, retardance and diattenuation. The results are shown in Figure 52, where the decomposition of the Mueller matrix image of several samples at an SRA of $20°$ are presented.

By pure observation of Figure 52, one can conclude that in terms of the depolarization matrix, M_{Δ}, some materials significantly depolarize more than others, being metallic car paint and solid traffic signals the ones that depolarize the less. In addition, the retro-reflective traffic signal presents a considerable displacement from the other groups of materials in terms of its retarder matrix M_R. In terms of the diattenuation matrix, the material groups that apparently show some dependence on M_D are solid traffic signal and metallic car paint.

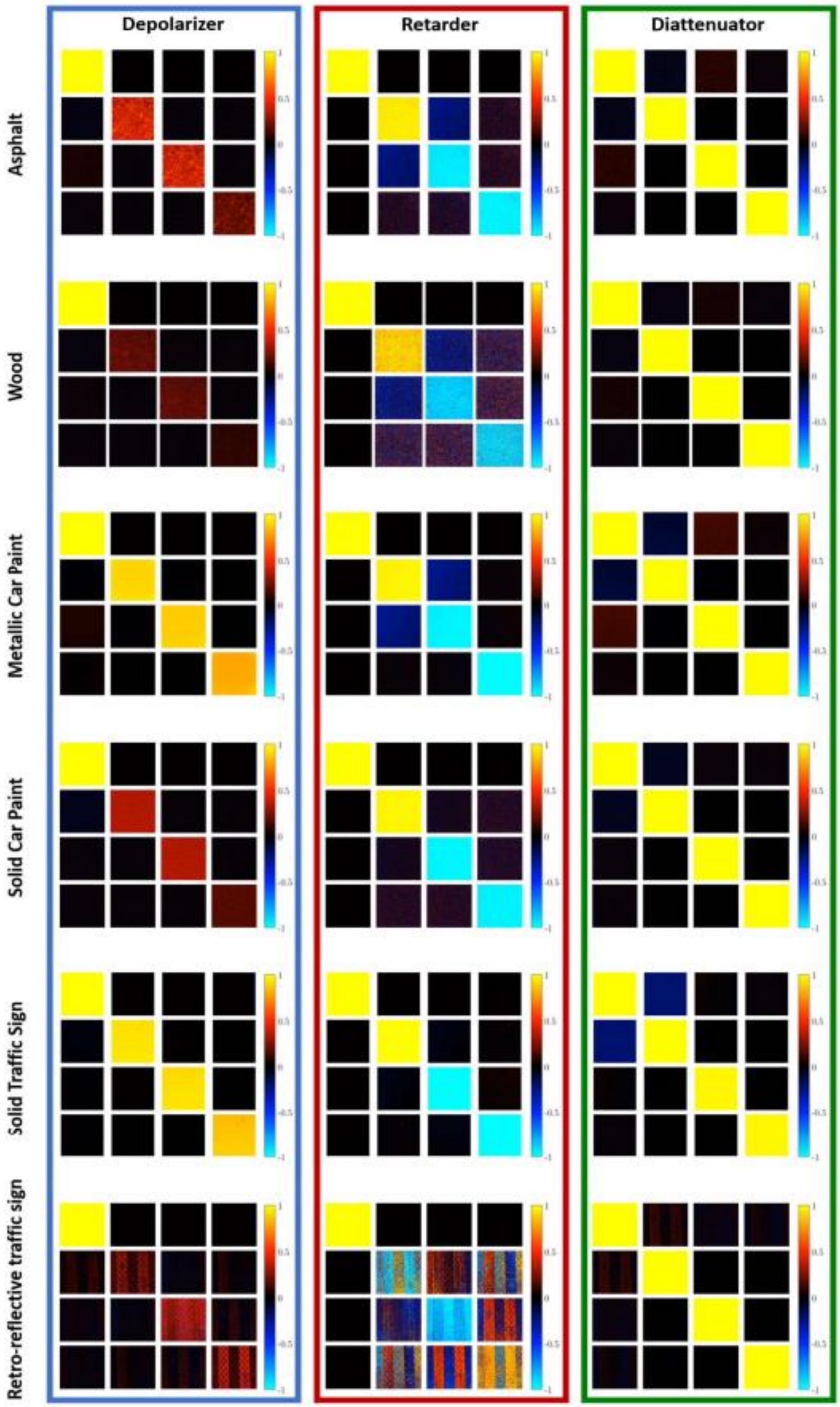

Figure 52. M_Δ, M_R and M_D resulting from the decomposition of the Mueller matrix at 1550 nm at an SRA of 20° of one sample of each group of materials. The Mueller decomposition matrices were determined with the QWP Mueller setup.

A quantitative study of the dependence on the SRA of the matrices resulted from the decomposition of the Mueller matrices, of the complete spectrum of samples, were afterwards plotted in Figure 53, Figure 54, and Figure 55. As in the Mueller matrix case, the Mueller matrices in Figure 53, Figure 54, and Figure 55 were normalized and the images' pixels were averaged in order to analyse the polarization, removing reflectance.

As expected from the predictions, the depolarization seems to be the factor that differentiate more significantly materials. Note that the main depolarization effects affect the diagonal elements of the experimental Mueller matrices, as it can be observed in Figure 49. In terms of retardation, materials like wood and retro-reflective traffic signal are suggestively more differentiated. The diattenuation allows clear distinction of solid traffic signal and metallic car paint from the rest of the samples.

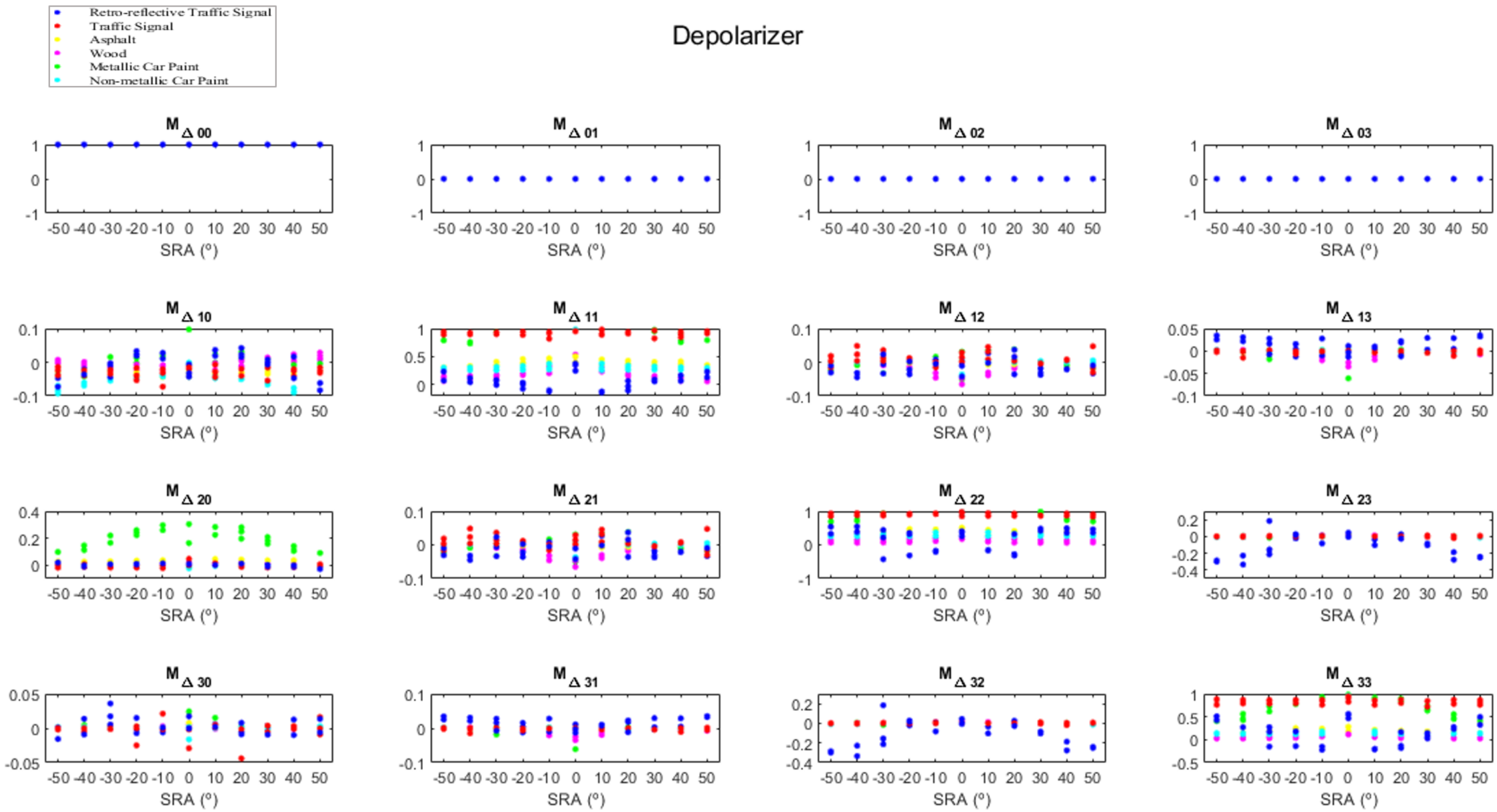

Figure 53. Depolarizer matrix, M_{Δ}, as a function of the SRA (°), resulting from the decomposition of the Mueller matrix at 1550 nm, for multiple samples of each material: retro-reflective traffic signals (blue), traffic signals without retro-reflectance properties (red), Asphalt (yellow), Wood (magenta), metallic and non-metallic car paints (green and cyan, respectively), determined with the QWP Mueller setup.

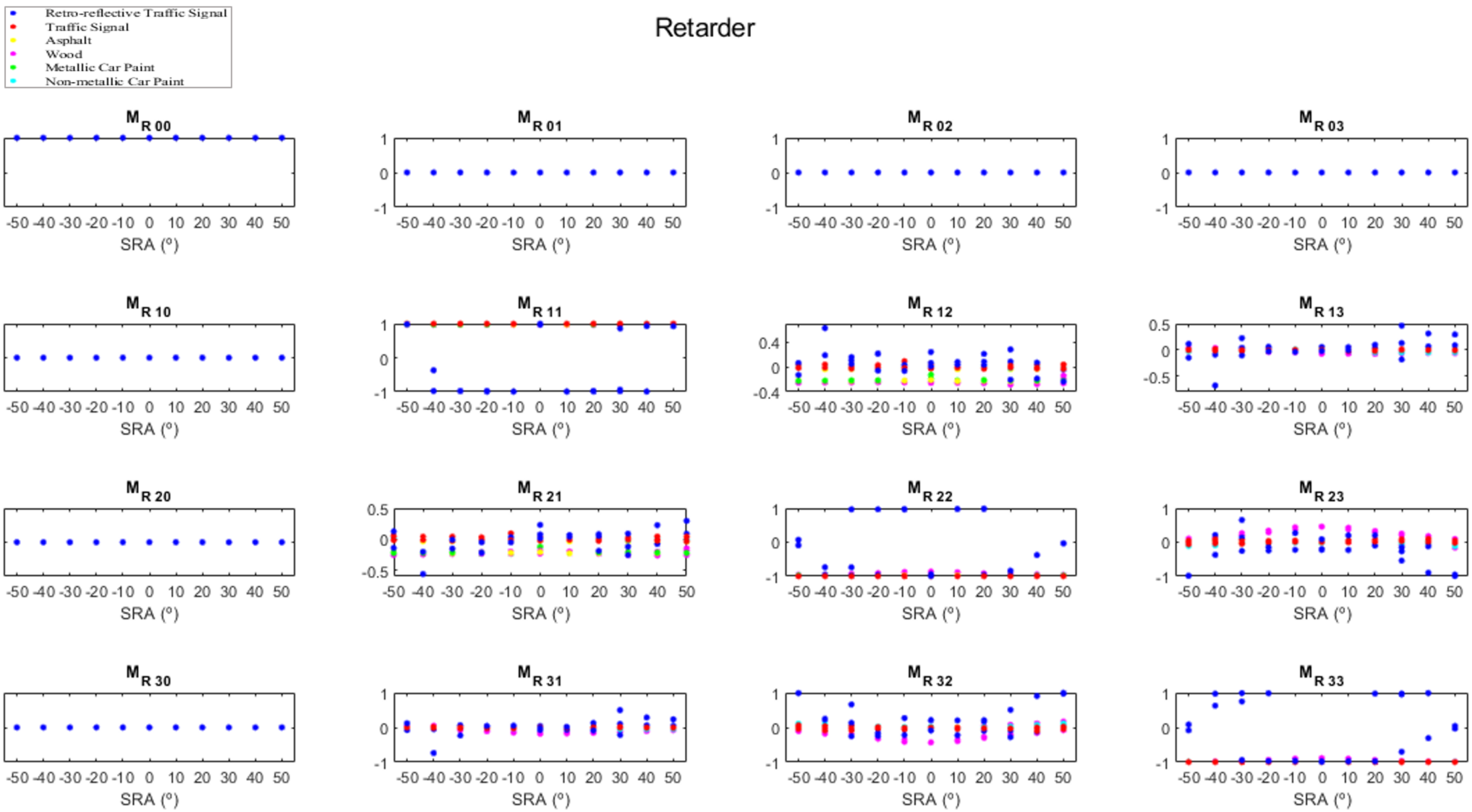

Figure 54. Retardance matrix, M_R, as a function of the SRA (°), resulting from the decomposition of the Mueller matrix at 1550 nm, for multiple samples of each materials: retro-reflective traffic signals (blue), traffic signals without retro-reflectance properties (red), Asphalt (yellow), Wood (magenta), metallic and non-metallic car paints (green and cyan, respectively) , determined with the QWP Mueller setup.

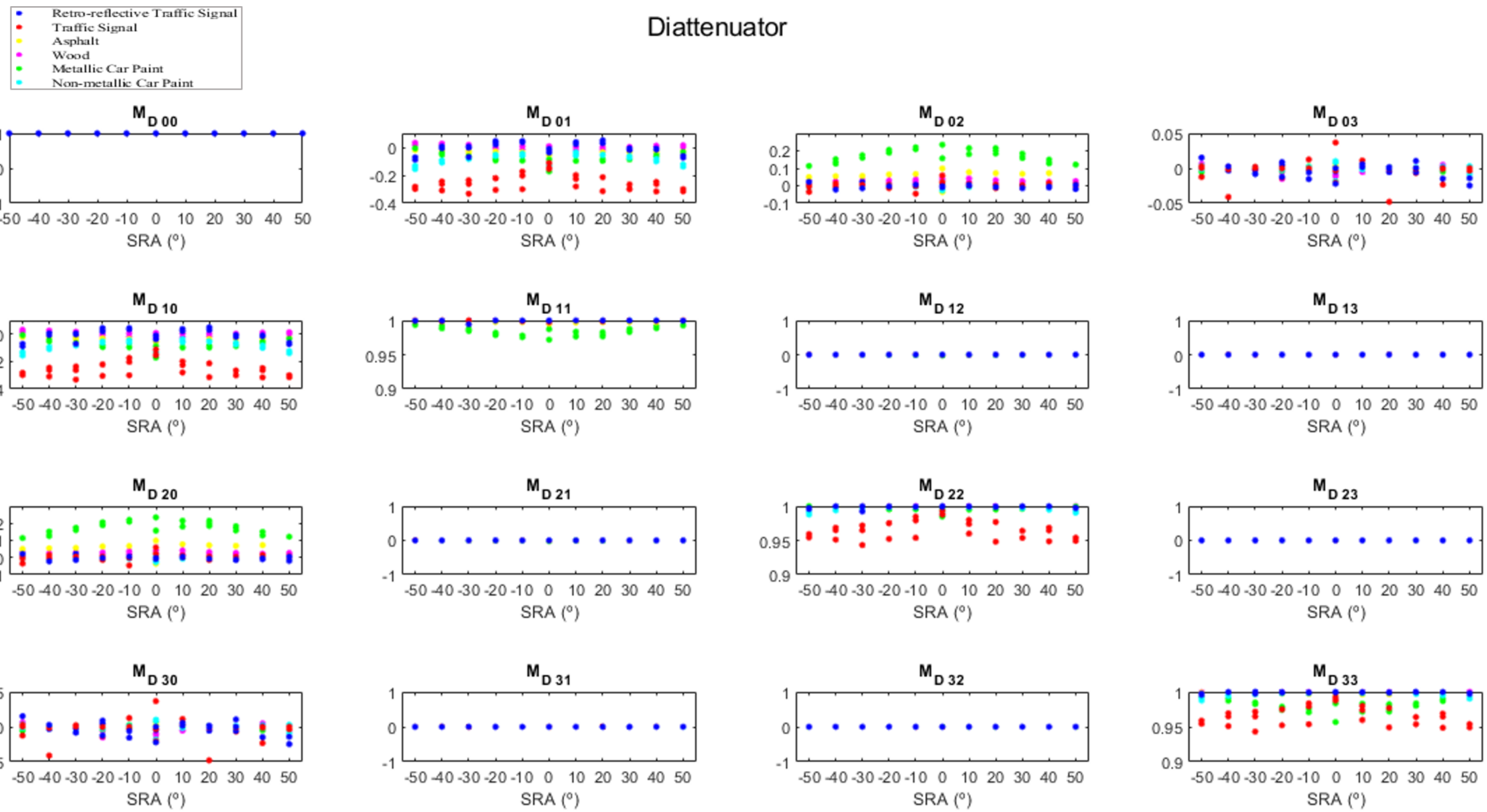

Figure 55. Diattenuator matrix, M_D, as a function of the SRA (°), resulting from the decomposition of the Mueller matrix at 1550 nm, for multiple samples of each materials: retro-reflective traffic signals (blue), traffic signals without retro-reflectance properties (red), Asphalt (yellow), Wood (magenta), metallic and non-metallic car paints (green and cyan, respectively), determined with the QWP Mueller setup.

6.5. Discussion of the Polarimetric Results

The presented Mueller polarimeter was idealized to realise the possibilities of differentiating different groups of materials by means of light polarization at 1550 nm of wavelength. As it was expected and it was evidenced, different materials, effectively, have different polarimetric responses allowing material discrimination. In addition, it was shown that same materials (such as car paints) have identical polarimetric responses.

As it was perceived, some Mueller matrix elements have a greater relevance to distinguish between different materials (the diagonal elements of the Mueller matrix). The graphical representations in Figure 50 allow clear distinction of materials and let extrapolate that material discrimination might be enhanced by using more than three Mueller matrix coefficients. This first study let infer that a polarimetric 1550 nm LiDAR is capable of distinguishing between at least some materials. This concept shows having great importance in autonomous vehicle safety, adding information that allows the vehicle to make a more trustworthy decision, and possible obstacle avoidance with fewer data processing. For this reason, the next chapter of this dissertation is focus on the design and implementation of a 1D LiDAR, in order to combine distance and polarimetric measurements.

Another important conclusion of this study is that the Mueller matrix elements, by itself, present enough information and of greater importance than specific properties of the Mueller matrix as: diattenuation, polarizance or the matrices resulted from the Mueller decomposition (diattenuator, retarder and depolarizer). That is to say, due to the determination of specific properties of the Mueller matrix is time consuming and the autonomous vehicle need of a real time response, we consider that the Mueller matrix elements differences are enough to discriminate the measured materials.

Therefore, we propose, for future work, to create a robust data basis containing the Mueller matrix of a huge variety of road scene objects and to train a machine learning algorithm to material recognition. The proposed method is largely applied in autonomous car applications [177] due to its fast response. The intensification in the number of samples of the studied materials and the increase of different materials is needed in future works to enhance the plausibility of this study.

7. 1D LiDAR

7.1. Experimental configuration of the one-point LiDAR prototype

The starting point of developing the polarization LiDAR proposed in this project is the implementation of a pulsed ToF LiDAR system in one spatial dimension. The conception of this architecture consists of a laser, two high-speed APDs, electronics behind that allows us to control the laser and to make the acquisition of the time of flight, and the optical components responsible to collimate the laser light beam and to focus the reflected light into the detectors' detection area. The high-speed APD were used instead of single photon detectors (see section 4.1.4), because the automotive market is searching for less expensive LiDAR solutions so that it is viable to implement in vehicles. Nevertheless, a linear analog detector, like a high-speed APD, will provide amplitude signals which depend linearly on the optical power.

The systems architecture can be observed in Figure 56. The setup was built thinking about the implementation of the next steps, i. e., to implement the scanning technology and to achieve a 3D LiDAR.

Firstly, one should focus its mind on the setup part consisting on a pulsed laser "PEFL-K08-LP-015-005-010-1550-T1-ET0-PK26D-C1" from *Keopsys* [178] (λ = 1550 nm) and the two InGaAs APD detectors "APD310" (bandwidth 850-1650 nm) from *MenloSystems* [179]. The laser emits linearly polarized pulsed light beams at a 10-20 kHz frequency, so that a START signal is recorded by one of the ADPs and the STOP signal is recorded by the second ADP. The time interval between the START and STOP signal gives the needed information to determine the distance of an obstacle in the direction of the outcoming laser beam. Due to electronic constrains, the timing electronics are used in the reverse mode (see section 4.1.3), meaning that the input STOP signal is our reference from the laser and the input START signal is the signal incident in the obstacle.

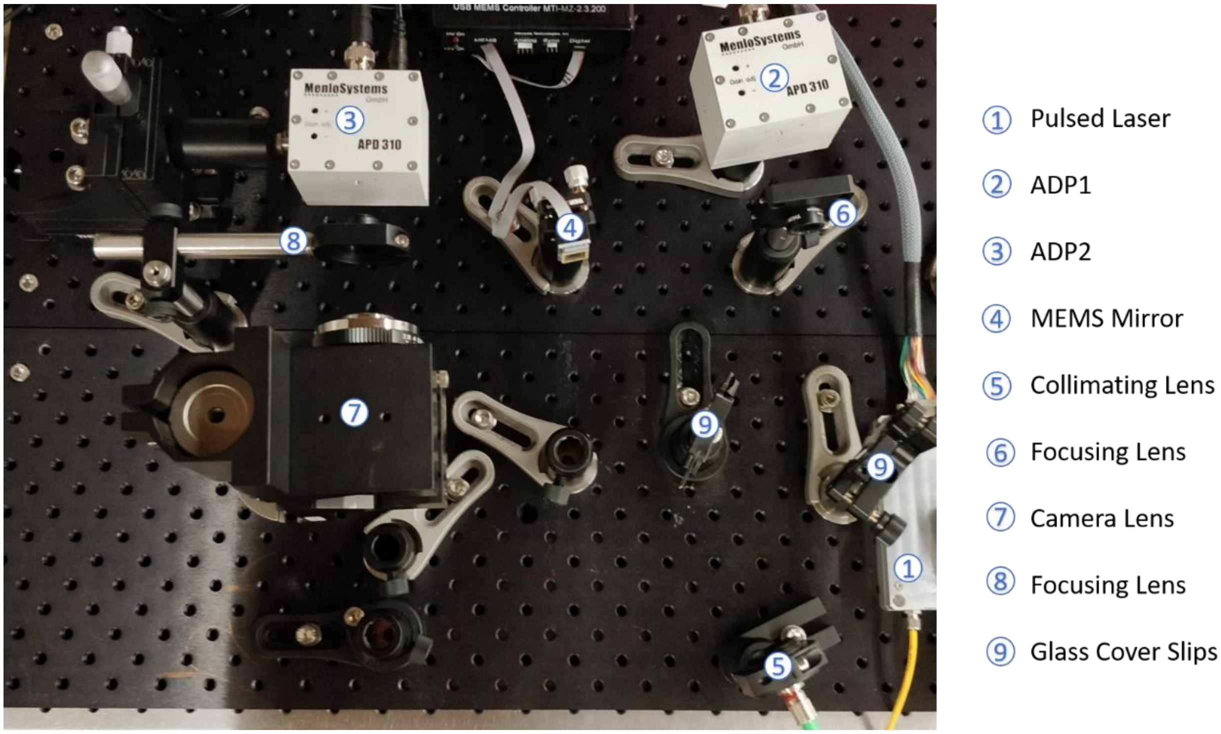

Figure 56. Experimental one-point LiDAR setup. The pulsed laser (1) generates a linearly polarized pulse that is collimated by the collimating lens (5). The existing pulse is divided by two glass cover slips (9) in order to reduce the intensity of the existing beam. One part of the beam is focused by a focusing lens (6) on the ADP1 (2). The portion of the laser beam with higher intensity, by the first glass cover slips, is directed to the target by a MEMS Mirror (4). The backscattered light is focused by a camera lens (7) and a focusing lens (8), to be detected by the ADP2 (3).

The ADP responsible for recording the reference signal is the ADP1 in Figure 56. Since the maximum power of the light pulse prevenient from the laser source is greater than the maximum power that the ADP can detect, without getting permanently damaged, two microscope glass cover slips were used to reflect a small percentage of light, into the ADP1. This principal is theoretically expected by Fresnel equations, for polarized light [149]. Having this in mind, to guarantee that the APD1 detects a significantly small light intensity, the laser was positioned so that it emits HLP in the lab referential. Also, the fibre laser source has a F240APC-1550 [180] collimating lens, from *Thorlabs*, in its output placed and marked by the supplier to ensure and to help the user find the best collimation of the fibre laser.

The ADP2 is responsible for detecting the incoming light from the reflection in the obstacle and, since the obstacle might absorb some light intensity and, more importantly, the ADPs transimpedance gain was adjusted so that, in the specular reflection, the detector was never close to its breakdown limit.

High-speed APDs, in order to have a fast response, have a very small detection area (detector's diameter of 0.03 mm [179]). Therefore, before each ADP, a lens is placed to focus the incoming light into the detection area of the detector. Prior to ADP1, the placed lens is a LA1289-B-ML [181]. Nevertheless, before the ADP2, an optical system formed by a TEC-M55 lens [182] and a LA1540-B-ML lens [181] is placed.

7.2. Monitoring and Laser Control

The proposed LiDAR uses a pulsed fiber laser "PEFL-K08-LP-015-005-010-1550-T1-ET0-PK26D-C1" from *Keopsys* [178] that needs to be controlled and electrically fed by an interface platform [178]. In the development of this project, the used interface is a "INTF-PK26D" from *Keopsys* [178] with a "Sub-D25/Micro Sub-D25" connector cable and a supplied voltage of $25\ V$ (see Figure 57). The interface has a pulse distributed feedback trigger input connected, via a BNC connector, to an external signal generator. The last is required to generate an input TTL signal characterized as: a square wave with a $V_{CC} = 5\ V$, a frequency of $10\ KHz$ and a duty cycle of 20%. Finally, the interface platform is connected to a computer, via a Sub-D9/USB cable, which is in charge of the control of the laser light source via a software named "Kontrol" [178], provided by the interface supplier. This software allows us to turn the laser on and off, set the current supplied to the laser and monitoring parameters, such as the current supplied to laser preamplifier and its booster, the distributed feedback frequency and the laser temperature.

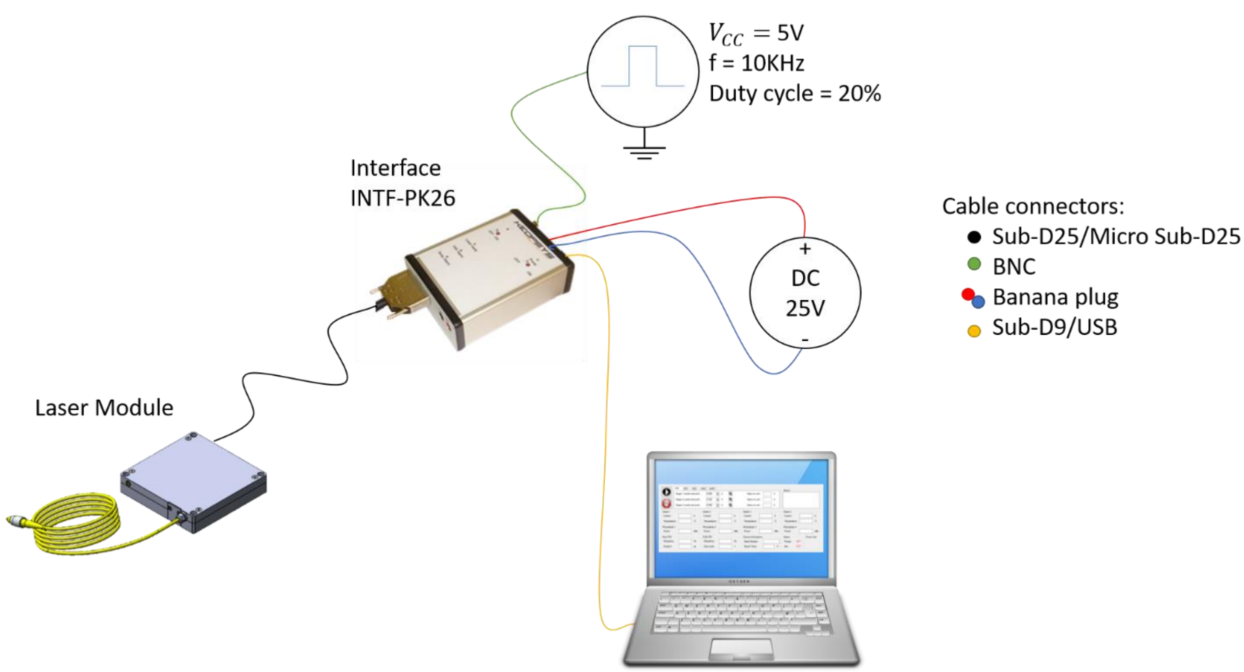

Figure 57. Electrical scheme of the laser module "PEFL-K08-LP-015-005-010-1550-T1-ET0-PK26D-C1".

7.3. Photodetection electronics

The ADP is a user-friendly complex sensor that integrates its own internal circuitry that comprises a temperature compensation circuit and an integrated amplifier with a continuously adjustable gain setting [179]. The ADPs have an included power supply with a country specific wall plug adapter that only needs to be directly plugged into the mains electricity network [179]. These sensors also have an output BNC connector that returns the sensors electrical response from the detected light.

7.4. Signal Characterization

To understand and predict the systems behaviour, a signal characterization was pursued. Firstly, the signals from the ADP1 and ADP2 were analysed in the oscilloscope (model "HDO4034A" from Teledyne LeCroy [183]). The measured signals of specular and diffuse retroreflection are represented in Figure 58. The current intensity supplied to the laser was adjusted to guarantee that a measurable signal was detected but also it did not saturated nor damaged the detectors.

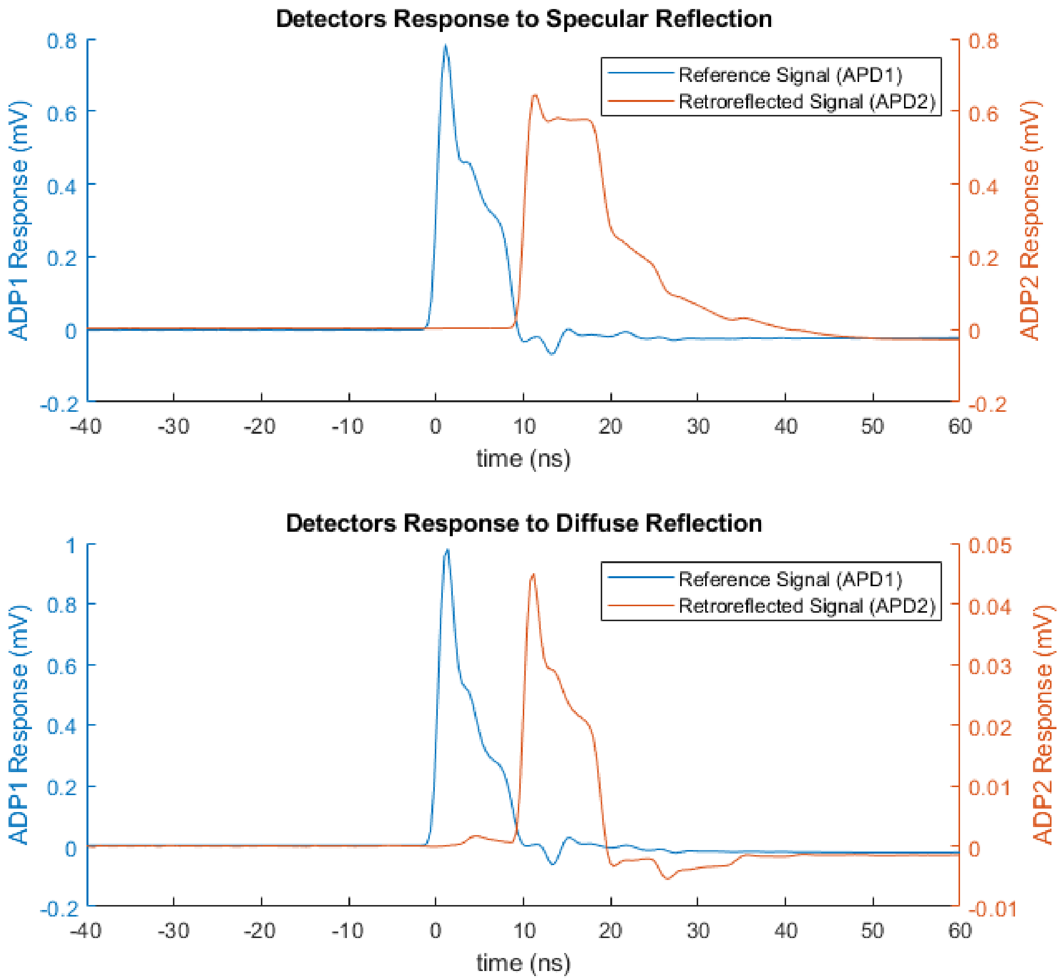

Figure 58. Reference (blue) and Retroreflected (red) signals of specular and diffuse reflections. The 1550 nm pulse laser was fed at 1.3 mW (specular refection) and 2 mW (difusse reflection).

The recorded reference pulses (shown in Figure 58) have a waveform similar to the one provided by the laser manufacturer (see Figure 59). To understand the represented electrical behaviour, one must consider that the electrical response in Figure 58 is the convolution of the optical pulse with the ADP's instrument response function [184].

Note that, after the high amplitude pulse, there is an extension of the response time. This response duration is extended due to the high avalanche gain of the detector [184]. Furthermore, during the response duration, the waveforms exhibit ringing due to signal line reflections (for more technical information read reference [184]). In addition, the waveforms in Figure 58 also present a non-expected behaviour, since it does not reach negative values in manufacturer report (see Figure 59). Regardless, this ringing type of behaviour is predicted in the literature whenever the stability of the APD system is compromised to increase the photoreceiver speed and sensitivity [184].

After the electrical signal reaches the ground state, there is an oscillator behaviour [179] caused by the APD feedback system electronics [185], responsible for carrying the sensor back to the ground state level, as quick as possible [185]. Also, the specular retroreflected signal has a slower transit time due to a lower transimpedance gain selected, in order to measure the specular signal without damaging the APD.

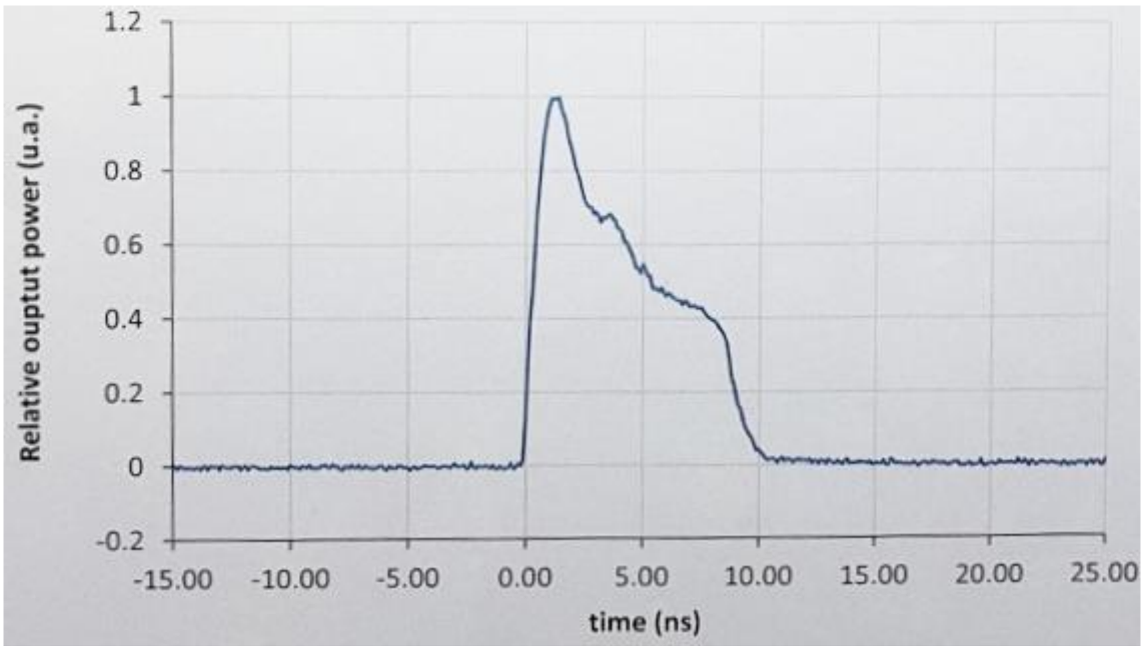

Figure 59. The "PEFL-K08-LP-015-005-010-1550-T1-ET0-PK26D-C1" time dependence of the relative output power, from the Test Report made by Keopsys [178].

After the first evaluation of the obtained signal, 1000 pulses were recorded. The mean of the waveform and its standard deviation (STD) were produce in Figure 60.

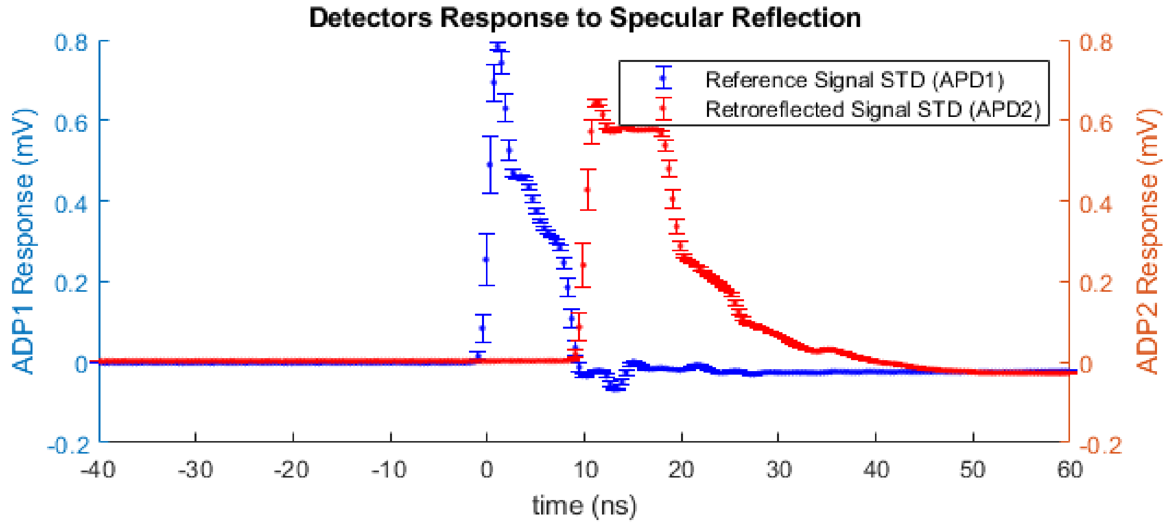

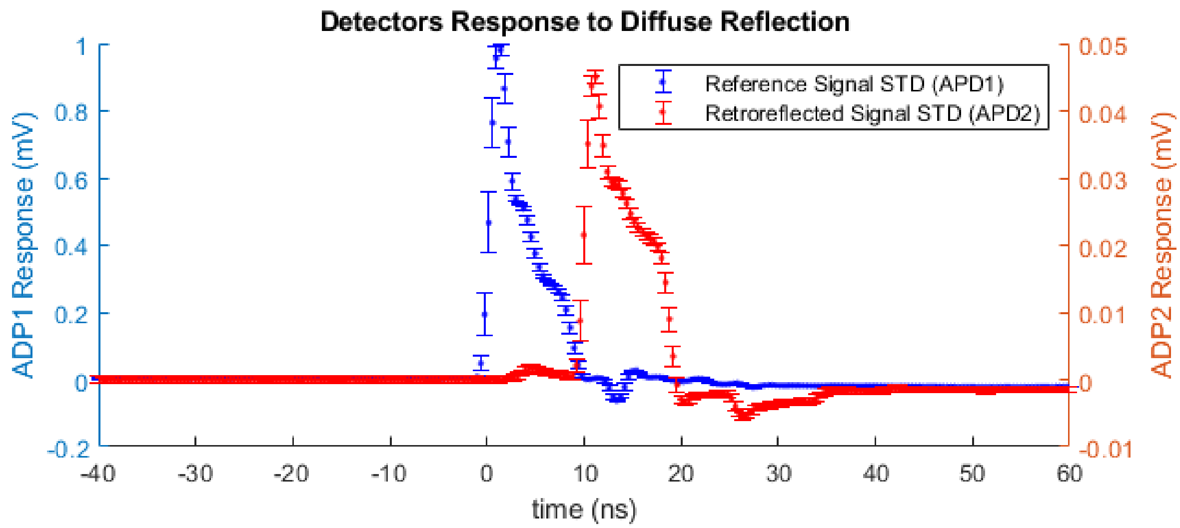

Figure 60. Standard deviation of 1000 measured pulses of the Reference (blue) and Retroreflected (red) signals of specular and diffuse reflections, the laser was electrically fed at 1.3 mW and 2 mW, respectively.

The timing electronics used to the time-tag recording is the "SPC-160" and the "Delay-Box-32N" from *Becker & Hickl GmbH* [186]. The chosen system requires that the input pulses have a negative polarity. To achieve this condition, the TCSPC supplier recommend the use of the passive differential pulse inverter "A-PPI-D" [187]. Therefore, an "A-PPI-D" is connected to each of the APDs output. Hence, the electric signals resulting from the inversion of the specular signals descripted in Figure 58, by the "A-PPI-D" passive differential pulse inverter, are presented in Figure 61.

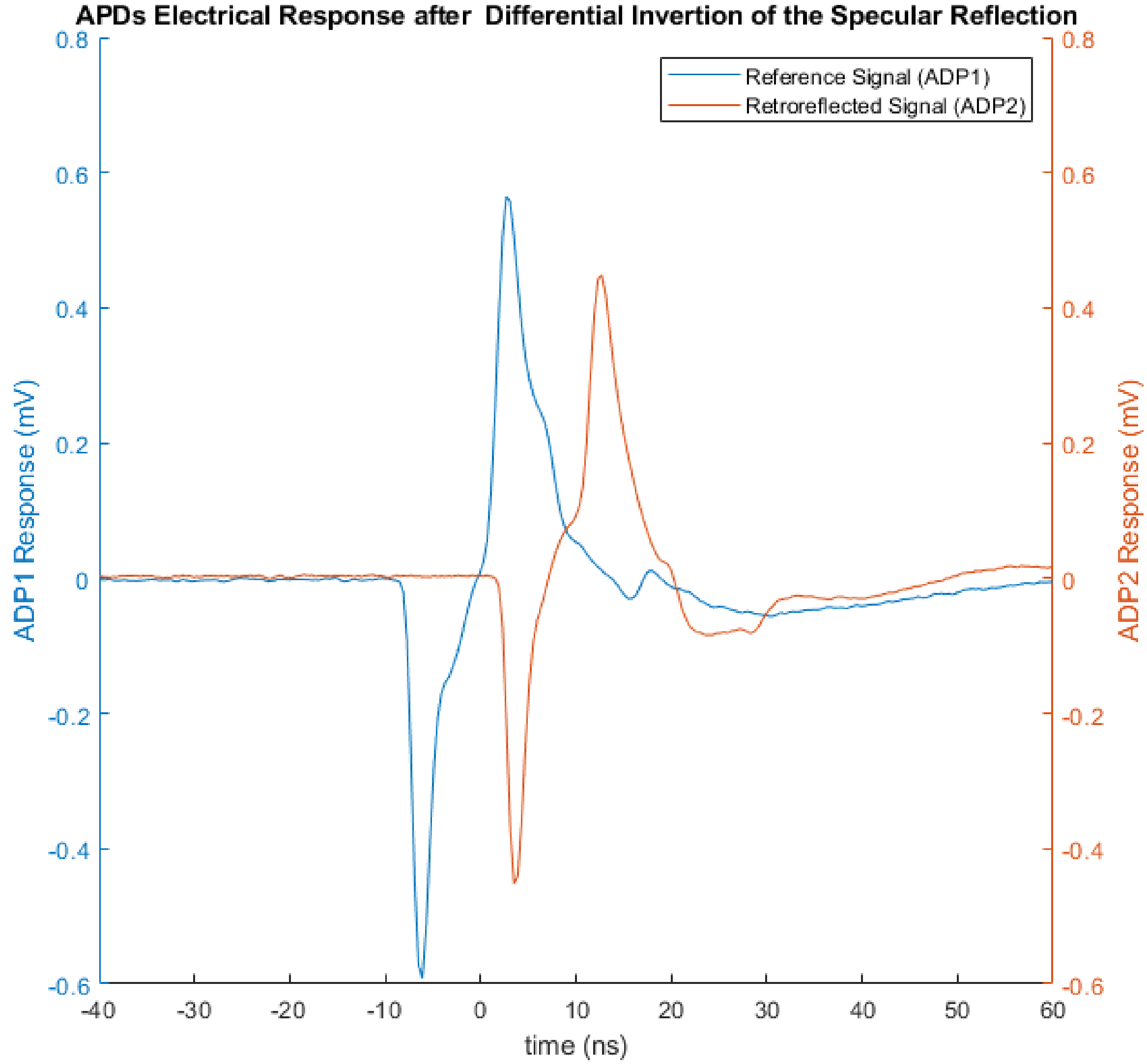

Figure 61. The electrical response to Specular Reflection (of the reference APD (blue) and the Retroreflected signal measured by the APD2 (red) to a Specular Reflection after passively suffering a differential inversion.

7.5. LiDARs Spatial Calibration

As one can predict, there are multiple factors that can influence the systems accuracy. On the one hand, there is an uncharted difference in the optical path between the path length travelled by the reference signal and the path travelled by the emitted light pulse (including the optical paths by traversing the lens). The optical path in the LiDAR setup can be observed in Figure 62. On the other hand, there is also an uncharted difference between the transit time of the two electrical signals due to, not only the delay imposed by the delay box, but also the cable length difference between the two ADPs. Therefore, the system is in need of correcting the systematic spatial displacement, thereupon a distance calibration was sought.

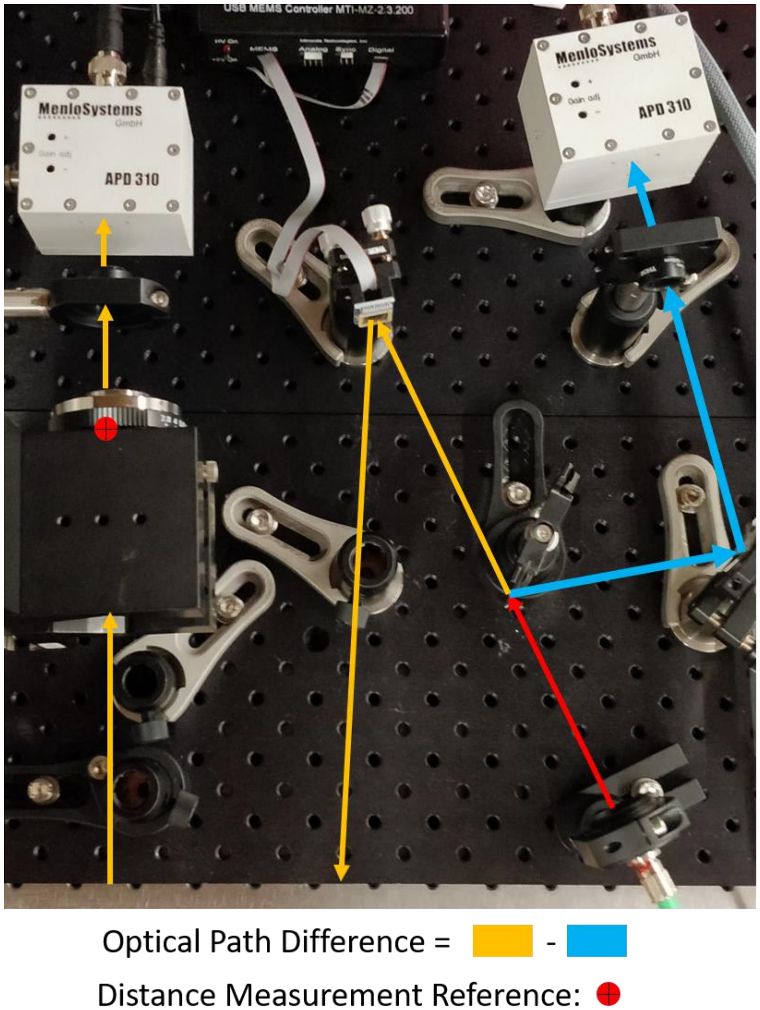

Figure 62. Schematic representation of the optical path inside the experimental one-point LiDAR setup and the reference for distance measurement.

Afterwards, the timing system was implemented, and the calibration of the LiDAR prototype was performed by measuring the recorded ToF for multiple target positions, between $1.0612\ \mathrm{m}$ and $5.5750\ \mathrm{m}$, in a way that the specular reflection light was detected.

There are two different ways of measuring the time difference between two pulses: either using a time-to-digital converter (TDC), either by using and analog-to-digital converter (ADC).

TAC/ADC implementations use a Time-To-Amplitude converter (TAC), and the output is an amplitude proportional to the interval between two detected events, which is sampled in a digital format by the ADC.

The architectures by TDCs use a start-stop system, similar to a TCSPC system, where the electronic system starts and stops a timer whenever it detects an incoming signal. In this type of system, more than one ion arriving at the detector generates the same response as a single ion or ions that arrive slightly later in time.

The two different implementations have some limitations in terms of the accuracy and precision of the ToF measured. The TAC/ADC architecture range of detection is determined by minimum and maximum available TAC amplitude, and its accuracy precision are limited by the resolution of the ADC's discretization (TAC/ADC cannot time intervals smaller than the ADCs' resolution) [188]. Besides that, TDC's architectures calculated the ToF via will be limited by the range, accuracy and precision of their clocks. Moreover TDC's systems are simpler and straightforward to determine the ToF [189].

The time difference between the detection of the two pulses was recorded with a SPC-160 electronic board that makes use of an ADC implementation (TAC-Biased Amplifier-ADC), and the results were presented by the *Becker & Hickl GmbH* software [190].

Since the system is in reverse measuring mode, one should expect that the measured ToF ($ToF_{\ TCSPC}$) depends on the selected time range and on the total delay of the reference signal in the system [89]. This relation is given by

$$\begin{gathered} ToF = (time\ range + total\ delay) - ToF_{\ TCSPC} \iff \\ \iff ToF = (50\ \text{ns} + total\ delay) - ToF_{\ TCSPC} \end{gathered} \tag{45}$$

As referred in the beginning of this chapter, there is an uncharted difference in the reference and emitted light pulses optical path. In addition, due to the use of a delay box, it became quite difficult to forecast the influence of the cable length and of the delay box system itself without the right tools. For those reasons, one should consider all of these delay parameters as one, called total delay. The recommendation is that the total delay introduced in the system is one order of magnitude less than the selected time range [89].

For these reasons, the search for a distance calibration system was solely made by relating the measured ToF, converted into a distance (see section 1.1.2), and comparing it to a reference position (see Figure 62) for measuring all distances. The referred distance was measured by a calibrated "Bosch Range Finder GLM 250 VF Professional" with a precision of 0.1 mm. The current intensity of the laser was adjusted, so that the APD2 measures specular light pulses with the highest intensity possible and compatible with the linear response in the APD2 output signal. The collected data is exhibited in Table 7.

Table 7. Comparison of the ToFs measured in the setup with the range finder measured distance. The measured ToF (left column) precision was considered to be the greatest time difference between two consecutive recorded times, and due to the handling of the range finder, its precision was estimated to be 4 times the range finder precision.

$\boldsymbol{ToF}_{\boldsymbol{TCSPC}}$ **(ns)**	***Range Finder Measured Distance*** $(\boldsymbol{m})$
$\mathbf{45.587 \pm 0.001}$	1.0612 ± 0.0004
$\mathbf{45.038 \pm 0.001}$	1.1345 ± 0.0004
$\mathbf{43.853 \pm 0.001}$	1.3098 ± 0.0004
$\mathbf{42.277 \pm 0.001}$	1.5404 ± 0.0004
$\mathbf{41.336 \pm 0.001}$	1.6853 ± 0.0004
$\mathbf{39.309 \pm 0.001}$	1.9921 ± 0.0004
$\mathbf{37.293 \pm 0.001}$	2.2909 ± 0.0004
$\mathbf{35.265 \pm 0.001}$	2.5956 ± 0.0004
$\mathbf{32.810 \pm 0.001}$	2.9697 ± 0.0004
$\mathbf{30.428 \pm 0.001}$	3.3327 ± 0.0004
$\mathbf{27.802 \pm 0.001}$	3.7322 ± 0.0004
$\mathbf{25.237 \pm 0.001}$	4.1241 ± 0.0004
$\mathbf{22.293 \pm 0.001}$	4.5626 ± 0.0004
$\mathbf{19.166 \pm 0.001}$	5.0391 ± 0.0004
$\mathbf{15.62 \pm 0.001}$	5.5750 ± 0.0004

One should expect a linear association between the $ToF_{\ TCSPC}$ and the measured distance d, expressed as

$$d = ToF \cdot \frac{c}{2} \Leftrightarrow \frac{2d}{c} = \big(50 \text{ ns} + total\ delay\ (\text{ns})\big) - ToF_{\ TCSPC} \Leftrightarrow \qquad (46)$$

$$\Leftrightarrow ToF_{\ TCSPC} = \left(50 \text{ ns} + total\ delay\ (\text{ns})\right) - 6.6713\ (\text{ns/m})\ \cdot d$$

where c represents the light speed and $Const$ is a constant of one order of magnitude lower than 50 ns. One should also expect variations in the slope attributable to the APDs response time and due to the wire length difference of the two ADPs. With the obtained data, a plot forecast was made (see Figure 63) to understand and calibrate the setup accuracy.

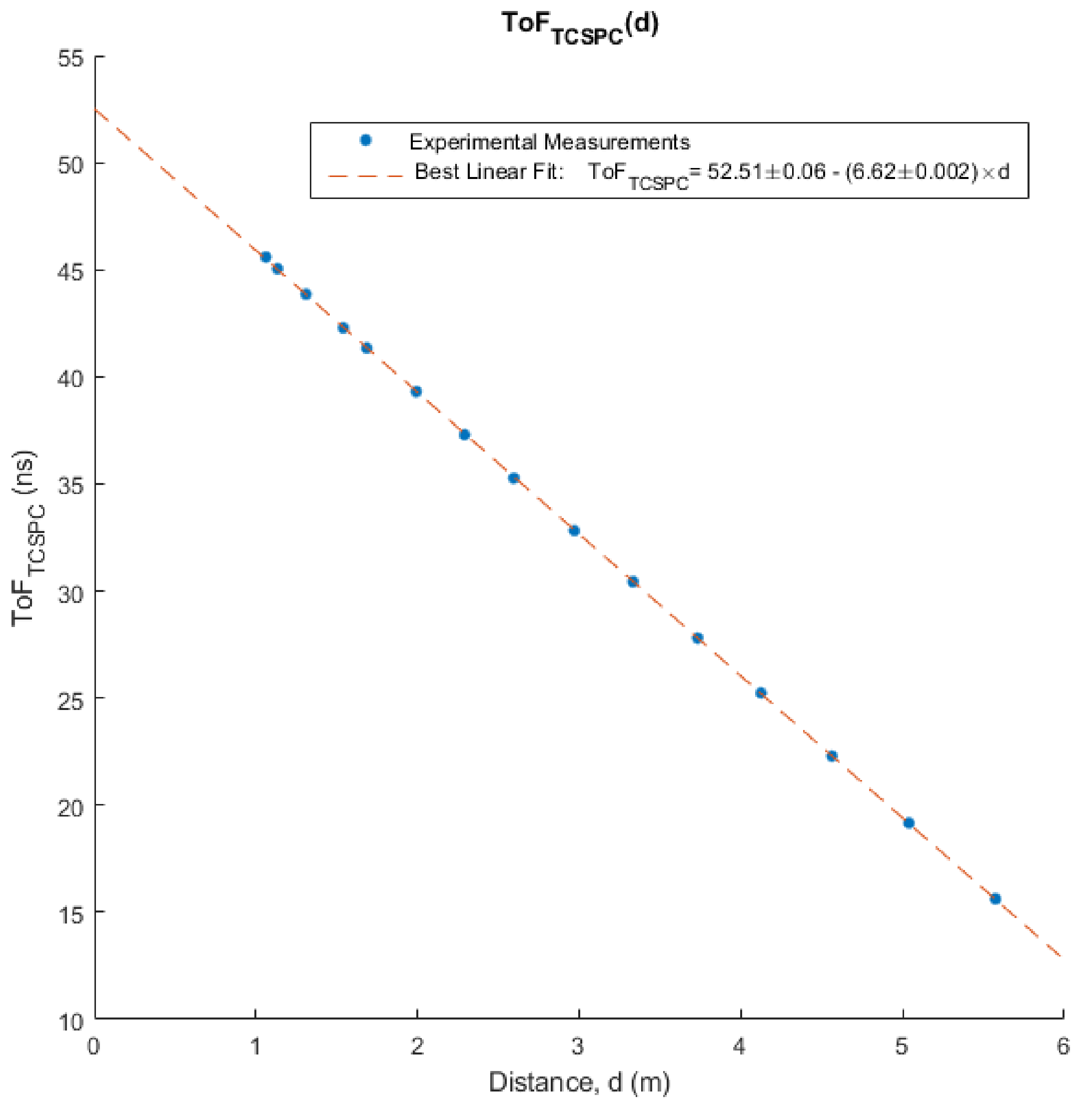

Figure 63. Sample's distance in terms of the ToF measured in: the TCSPC system (blue points) and its best linear fit (orange dashed line).

Analysing the linear regression and comparing it with Eq. (46), one concludes that the total delay is around 2.51 ns, which is in accordance with the recommendation of around 1 order of magnitude less than the selected time range. The slope of the linear fit shown in Figure 63 is not what one would expect through Eq.

(46)). The reason behind it is that Eq.(46)) does not predict the influence of all the elements such as the APDs response time and the wire length difference of the two ADPs.

7.6.System Precision

Once the accuracy calibration is set, the LiDAR precision was studied in relation to the range that was chosen to measure. On the one hand, the accuracy of a system consists on how close a measurement result is from the true value. On the other hand, the precision of a system is the degree to which reproducible measurements under unchanged conditions show the same result [191] (see Figure 64).

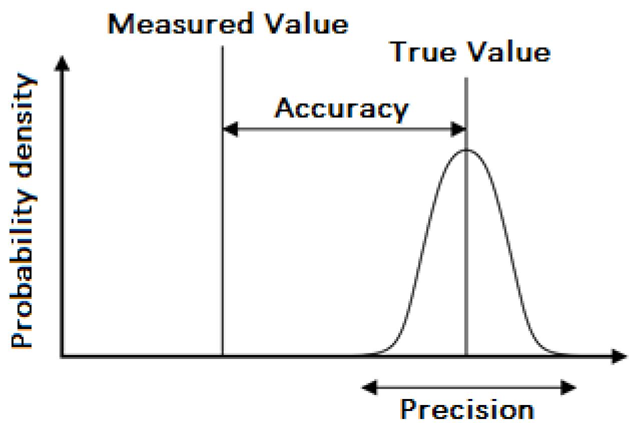

Figure 64. Graphical representation of the distinction between accuracy and precision (adapted from reference [192]*).*

In a real case, a system precision is not zero, so the result of multiple measurements tends to be described as a Gaussian probability density distribution. Therefore, the precision is correlated with the variance of the measurements, σ^2. The larger the variance, the less precise the system is. Due to the distances measured in our laboratory did not reach the six meters, and the laser not being eye-safe, the considered solution was to place the target always at the same distance (1.257 meters from the distance measurement reference in Figure 62), and to change the range of distances measured by the timing system.

A precision study was made to correlate the system's precision with a selected distance range. In Annex A

Table 11. Normalized Evaluation of the 1D Lidar precision as a function of the distance range (Range (m)). Experimental Results Distributions and their best Gaussian fits.

, the distributions of the experimental results and the best Gaussian fit normalized to its area of each one of them and its correspondent variance are presented.

Multiple measured results from the referred experimental procedure, the system's standard deviation, σ, and the discretization resolution, in accordance with the selected range are shown in Table 8. Subsequently, these results are represented in Figure 65.

Table 8. Set of experimental measurements in relation with the LiDAR selected range, and its Gaussian fits according to the determined mean value (Range (m)) and the estimated Standard Deviation (σ (m)).

Time Range (ns)	***Maximum distance*** (m)	***Discretization Resolution*** (m)	***Estimated Standard Deviation,*** σ (m)
3.334757	0.499867	0.000122	0.000869
5.002136	0.749801	0.000183	0.0009430
10.004272	1.499603	0.000366	0.0011384
25.010679	3.749006	0.000916	0.0020980
50.021359	7.498013	0.001831	0.0039678
79.919185	11.97958	0.002925	0.0059685
99.803379	14.96015	0.003653	0.0073541
150.064072	22.49404	0.005493	0.0112161
199.606759	29.92030	0.007307	0.0148452
259.924085	38.96164	0.009515	0.0188812
300.128144	44.98808	0.010986	0.0212937
399.213518	59.84060	0.014613	0.0282931
500.213564	74.98013	0.018310	0.0352837
601.121233	90.10581	0.022004	0.0423351
690.692319	103.5322	0.025283	0.0484208

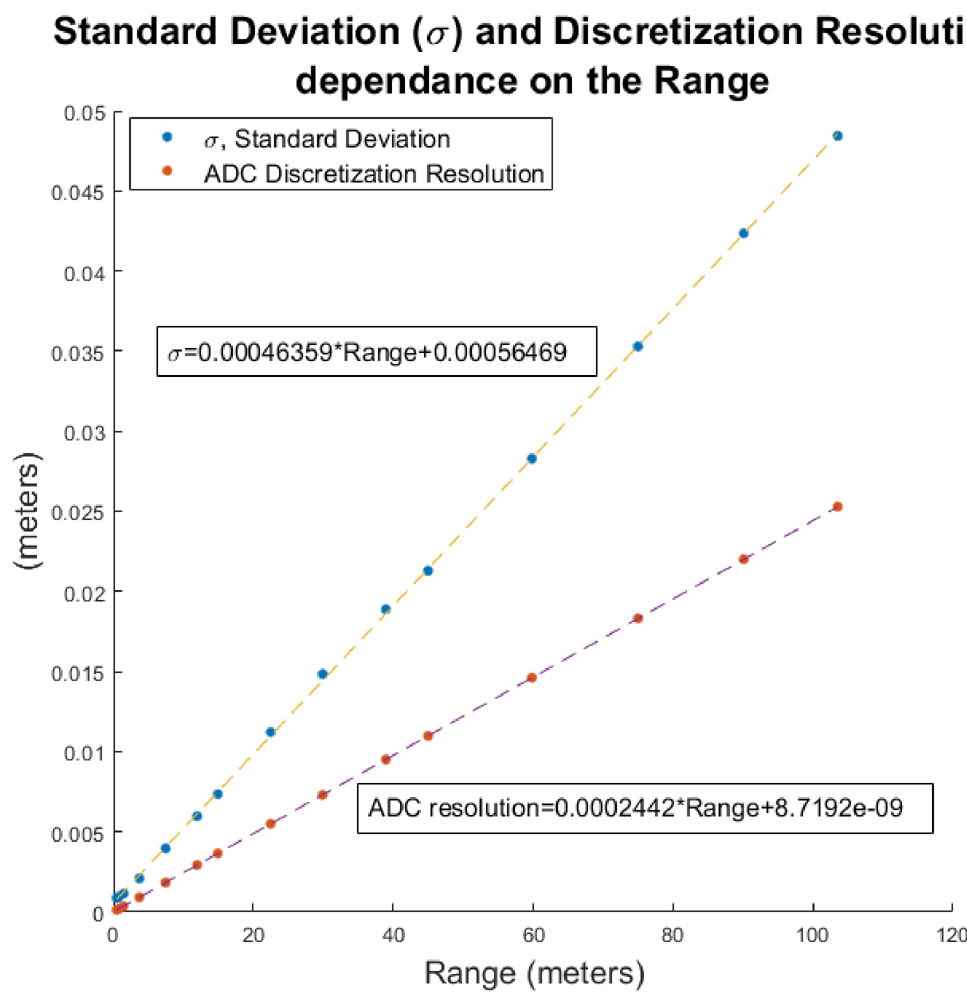

Figure 65. The developed 1D Lidar's: standard deviation, σ (m), *(blue) of the Gaussian distribution at 1.257 m and the ADC discretization resolution (orange) as a function of the measurable distance range (in m).*

From Table 8 and Figure 65, as it was expected due to its dependence on the ADC resolution, the system standard deviation has a greater influence in the systems precision. Since, in any measured case, the standard deviations are of the same order of magnitude of the ADC's discretization resolution, we can say that the limiting performance factor was found (ADC).

Although it is understandable that the standard deviation increases with the distance range increasement, meaning that the system becomes less precise by increasing the distance range, one should also realise that even in the worst studied case scenario, 103.53 m, the variance is five orders of magnitude smaller than the measurement. This behaviour reflects an outstanding Signal-to-Noise ratio of around 33 dB in the worst case studied scenario.

8. Polarization 1D LiDAR

This chapter is focused on combining the polarimetric knowledge acquired during the development of the present thesis with the one-point LiDAR experimental setup described in chapter 7. After the calibration of the experimental 1D LiDAR, the concept of introducing polarization in the system was explored. The 1D LiDAR system was updated to enable measuring the normalized Stokes vector (described in section 6.2.1) reflected by different samples. To predict the polarization state from the reflection of a polarized emitted light pulse and to correlate the results obtained from our experimental 1D LiDAR with the measurements of the Mueller polarimeter described in section 6.3.1, the light reflected by different samples was measured by using polarimetric techniques in-built on the experimental LiDAR presented in chapter 7. In this sense, polarization components (two linear polarizers and a quarter wave plate) are introduced into the LiDAR prototype (see Figure 66).

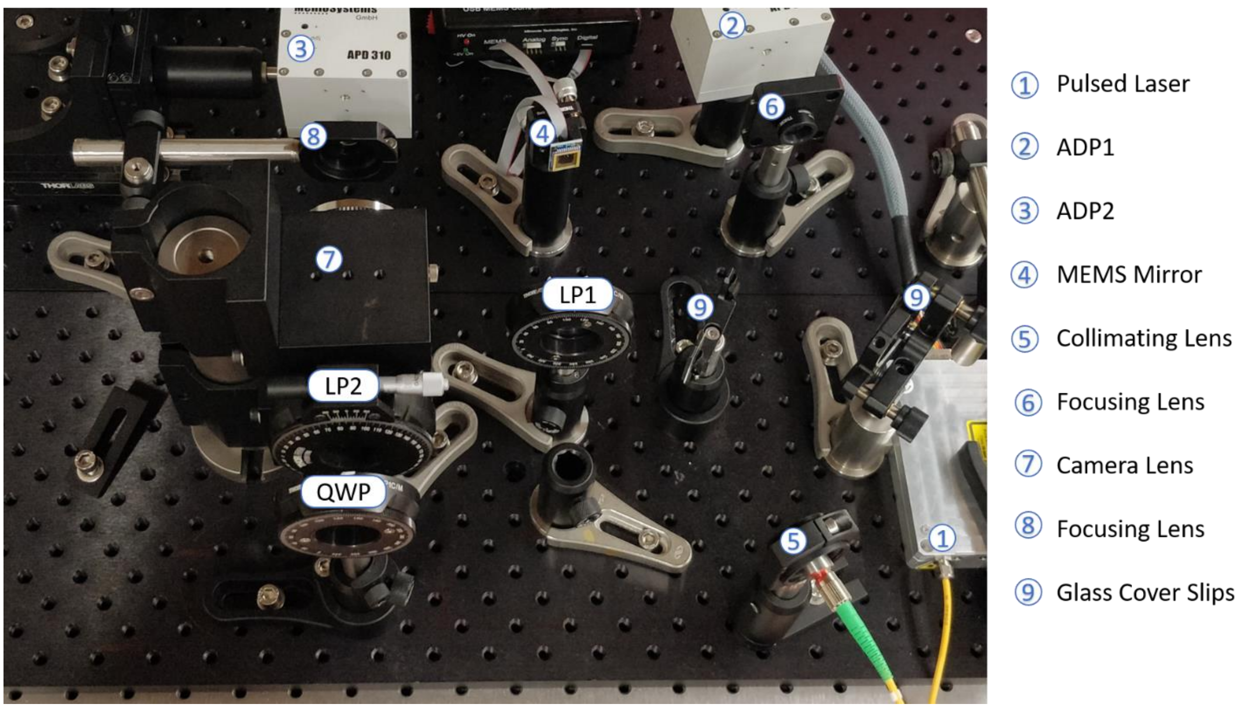

Figure 66. Experimental Polarization 1D LiDAR setup upgrade of the previous 1D LiDAR.

For a preliminary study, three materials were selected to be studied with this polarimetric LiDAR: a metallic car paint (Figure 67 (a)) and traffic signals without and with retroreflectors (Figure 67 (b) and (c), respectively).

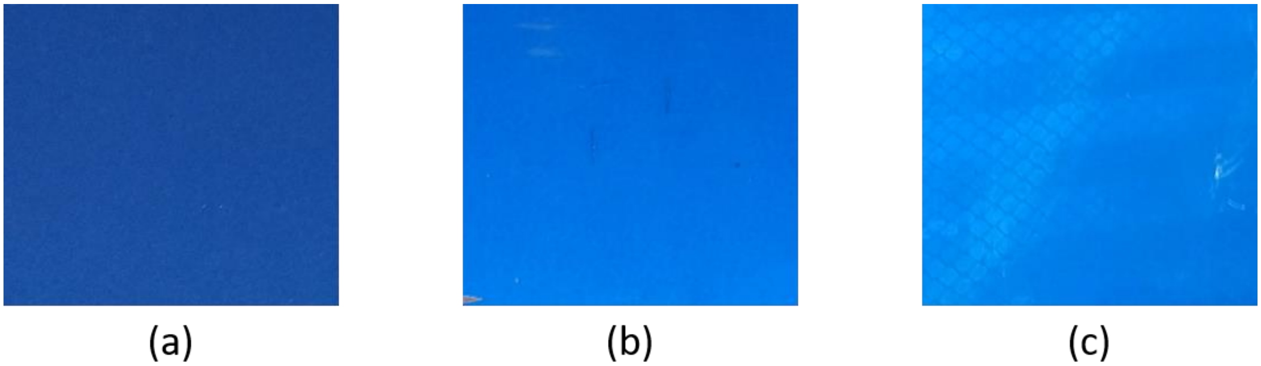

Figure 67. Photograph of the three samples that were subjects of the polarization 1D LiDAR study: (a) metallic car paint, and traffic signals (b) without and (c) with retroreflectors.

The main reason to choose the referred materials is that their Mueller matrices behaviour is clearly distinguishable (see Figure 49). In addition, the determination of the Mueller matrix is time consuming to be functional in autonomous driving. In contrast, the Stokes vector detection can be instantaneous [149], [152]. To this purpose, it was decided to illuminate the three samples with an HLP light state. The complete Stokes vector of the light beam reflected by the samples was measured at its specular reflection (i.e. SRA = 0°). At this moment, the setup is not able to measure the full Stokes vector simultaneously, so the measurements were taken sequentially in time.

Firstly, the Stokes vector from the HLP light reflected by the selected samples were mathematically predicted from the Mueller matrix images previously obtained with our complete Mueller polarimeter. The results from this study are summarized in Table 9.

Table 9. Normalized Mueller Matrix images, their respective average normalized Mueller Matrix and calculous of the HLP Stokes vector after interacting with the referred Mueller matrices, for three different materials (metallic car paint, regular traffic signal and retroreflector traffic signal) at a sample rotation of 0° (specular reflection).

Material	**Normalized Mueller Matrix Image**	**Average Normalized Mueller Matrix (M)**	$S_{out} = M \cdot \begin{pmatrix} 1 \\ 1 \\ 0 \\ 0 \end{pmatrix}$
Metallic Car Paint	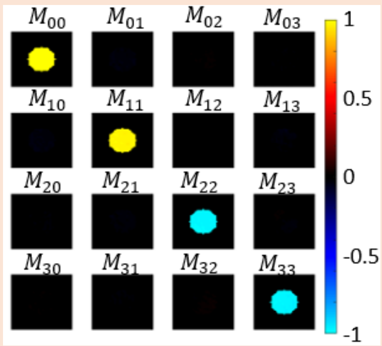	$\begin{pmatrix} 1.0000 & -0.027 \pm 0.006 & 0.011 \pm 0.008 & -0.008 \pm 0.007 \\ -0.030 \pm 0.005 & 0.977 \pm 0.005 & -0.001 \pm 0.005 & -0.020 \pm 0.01 \\ -0.011 \pm 0.007 & -0.021 \pm 0.007 & -0.980 \pm 0.004 & -0.01 \pm 0.02 \\ 0.009 \pm 0.006 & -0.010 \pm 0.009 & 0.01 \pm 0.01 & -0.976 \pm 0.006 \end{pmatrix}$	$\begin{pmatrix} 1.000 \pm 0.006 \\ 0.973 \pm 0.007 \\ -0.03 \pm 0.01 \\ 0.00 \pm 0.01 \end{pmatrix}$
Regular Traffic Signal	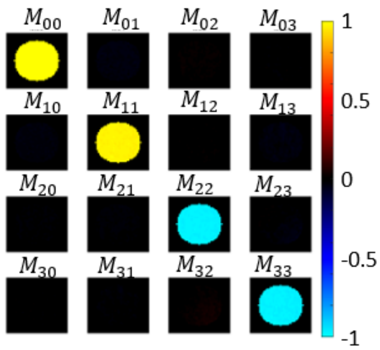	$\begin{pmatrix} 1.000 & -0.033 \pm 0.007 & 0.015 \pm 0.007 & -0.003 \pm 0.008 \\ -0.028 \pm 0.006 & 0.974 \pm 0.007 & 0.006 \pm 0.006 & -0.03 \pm 0.01 \\ -0.013 \pm 0.007 & -0.016 \pm 0.007 & -0.973 \pm 0.006 & 0.01 \pm 0.02 \\ -0.0012 \pm 0.007 & -0.011 \pm 0.009 & 0.02 \pm 0.02 & -0.971 \pm 0.007 \end{pmatrix}$	$\begin{pmatrix} 1.000 \pm 0.007 \\ 0.978 \pm 0.009 \\ -0.030 \pm 0.01 \\ -0.01 \pm 0.01 \end{pmatrix}$
Retroreflector Traffic Signal	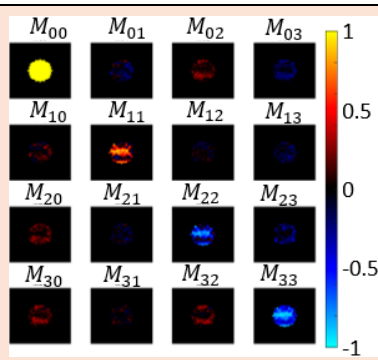	$\begin{pmatrix} 1.000 & -0.1 \pm 0.1 & 0.11 \pm 0.09 & -0.1164 \pm 0.09 \\ 0.1 \pm 0.1 & 0.4 \pm 0.3 & 0.00 \pm 0.07 & -0.0836 \pm 0.07 \\ 0.10 \pm 0.09 & -0.04 \pm 0.07 & -0.4 \pm 0.2 & -0.0967 \pm 0.1 \\ 0.1 \pm 0.1 & 0.00 \pm 0.06 & 0.1 \pm 0.1 & -0.6585 \pm 0.1 \end{pmatrix}$	$\begin{pmatrix} 1.0 \pm 0.1 \\ 0.46 \pm 0.3 \\ 0.1 \pm 0.1 \\ 0.1 \pm 0.1 \end{pmatrix}$

To generate the HLP state and to measure the Stokes vector from the specular reflection of each sample, the LiDAR proposed in Figure 56 was upgraded. To this end, on one hand, a calibrated linear polarizer (LP1), WP25M-UB [193] from *Thorlabs*, was used to generate the desired HLP state at the considered LiDAR's exit. On the other hand, a quarter wave plate (QWP), *Thorlabs* WPQ05M-1550 [194], and a linear polarizer (LP2), *Thorlabs* WP25M-UB [193] , were placed at the entrance of the detection system to analyse the six standard polarization states (HLP, VLP, LP+45°, LP-45°, RCP and LCP). The six analysed polarization states were calibrated using the Thorlabs polarimeter [163]. The final experimental implementation can be observed in Figure 66.

The light intensities measured from the backscattered light was recorded by using a digital oscilloscope (HDO4034 from *Teledyne Lecroy)*. To calculate the normalized Stokes vector reflected by the samples, Eq. (13) was used in respect to the maximum intensity. The comparation of the complete Stokes vectors measured experimentally with the calculated ones (from Table 9) is shown in Table 10.

Table 10.Comparation of Stokes vector of the specular reflection of HLP light in a metallic car paint, a regular traffic signal and a retroreflector traffic signal. Predicted normalized Stokes vectors calculated from the experimental Mueller matrices measured with our polarimeter are shown in the middle column, and experimentally normalized Stokes vectors measured with our 1D LiDAR are show in the right column.

Material	Predicted calculated normalized Stokes vector	Experimentally measured normalized Stokes vector
Metallic Car Paint	$\begin{pmatrix} 1.000 \pm 0.006 \\ 0.973 \pm 0.007 \\ -0.030 \pm 0.010 \\ 0.000 \pm 0.010 \end{pmatrix}$	$\begin{pmatrix} 1.0000 \\ 0.9841 \pm 0.0002 \\ -0.0500 \pm 0.0400 \\ -0.0200 \pm 0.0900 \end{pmatrix}$
Regular Traffic Signal	$\begin{pmatrix} 1.000 \pm 0.007 \\ 0.978 \pm 0.009 \\ -0.030 \pm 0.010 \\ -0.010 \pm 0.010 \end{pmatrix}$	$\begin{pmatrix} 1.0000 \\ 0.9509 \pm 0.0002 \\ 0.0200 \pm 0.0600 \\ 0.0650 \pm 0.0070 \end{pmatrix}$
Retroreflector Traffic Signal	$\begin{pmatrix} 1.00 \pm 0.1 \\ 0.46 \pm 0.3 \\ 0.10 \pm 0.1 \\ 0.10 \pm 0.1 \end{pmatrix}$	$\begin{pmatrix} 1.0000 \\ 0.4180 \pm 0.0007 \\ 0.0600 \pm 0.0800 \\ 0.0500 \pm 0.0200 \end{pmatrix}$

Before analysing Table 10, one must consider that none of the materials is homogenous. On the one hand, the traffic signals are real world samples with some dirt and scratches. On the other hand, although the metallic car paint is not a “real world” sample, it has mixed in its composition some reflective micro-flakes that grant it the metallic look. Therefore, one must consider that the data in Table 10 are not from the same exact area, meaning that the obtained differences between Stokes vectors are expected. In addition, the errors observed in Table 10 are due to fluctuations of the intensity of the lasers, small errors in the orientation of the QWPs and LPs, as well as phase variations in the LCVRs, and more importantly, the illuminated area in the two systems is not the same (owing to the lasers' beam size difference and to the fact that the lasers could be pointing at different regions in the sample).

Nevertheless, the metallic car paint shows similar results, as it is the most homogeneous sample. However, although the predicted and experimentally measured Stokes vectors present small differences between them, there are significant differences between some materials, such as between the retroreflector traffic signal and the two other samples. Consequently, it is perfectly possible to distinguish a retroreflector traffic signal from a regular traffic signal or a metallic car paint using a horizontal linear polarization state in a Polarization 1D LiDAR.

At this point, an extensive study of the generated polarization state, that better distinguishes the majority of the classified materials, is proposed. For this purpose, for future steps of this project, we suggest to characterize polarimetrically a great number of samples, and then, to study the best Stokes vectors to distinguish targets.

9. Conclusion

The present manuscript summarizes and reports the main work developed the academic year 2019/2020, in the facilities of the School of Sciences of the University of Minho.

Multiple worldwide companies are investing in developing a LiDAR system to implement in autonomous driving. LiDARs are active sensors that, by illuminating obstacles and measuring the retro-reflected light, can measure with great precision distances to obstacles in its surrounding, as well as, their shape. These characteristics make LiDARs a promising technology to the autonomous driving market.

Light polarization is a physical property that describes the transversal (to the direction of propagation) behaviour of a light wave. Whenever light interacts with matter, the polarization state of light might change. By means of this, a classification of materials through polarization is pursued. In this sense, a LiDAR that can distinguish materials through polarization can enhance the capability of making a more prudent decision in case of obstacle avoidance in autonomous driving.

Due to the referred reasons, this project furthers the idea of a LiDAR that can execute polarization measurements.

The first chapters are focused on describing the autonomous driving model, and the necessities surrounding sensor fusion. The components and techniques that are, nowadays, used in current LiDARs are also presented, as much as the state-of-the-art of the current developed LiDARs.

Then, two different types of Mueller polarimeters setups were built and described to appraise the capabilities of distinguishing between different materials, using a wavelength of 1550 nm. The Mueller polarimeters are distinguished by the method that they use to produce the PSG and PSA states. One of them makes use of linear polarizers and quarter wave plates and the other makes use of linear polarizers and liquid crystal variable retarders.

The Mueller polarimeter setups allowed to conclude that by means of light polarization at 1550 nm of wavelength, different materials have different polarimetric responses allowing material discrimination. In this sense, the diagonal elements of the Mueller matrix present more significant differences than the M_{03} and M_{30} components of the Mueller matrix. The graphical representations in Figure 50, allow clear distinction of materials, even if the sample rotation angle is unknown, and let extrapolate that material discrimination might enhance by using more than three Mueller matrix coefficients. The depolarization, diattenuation and retardance of each sample were also object of this study. Their determination proved to be time consuming, compared to the determination of Mueller matrix. For this reason, we conclude that these parameters do not show satisfactory results for autonomous driving.

The last part of this thesis is focused on the design, implementation and characterization of a Polarization 1D LiDAR. Firstly, the one-point LiDAR setup was presented, and a spatial calibration was sought. After that, an accuracy test was made, and afterwards the polarization concept was introduced to the already built setup. Due to the determination of a full Mueller matrix being too time consuming to be implemented in autonomous driving, we choose to only generate a polarization state and determine the full outcome Stokes vector from the light reflected by different targets. To test the Polarization One-Point LiDAR, we choose 3 different samples (metallic car paint, retroreflector traffic signal and regular traffic signal) and a horizontally linearly polarized state to be generated. The measurement was made detecting the specular reflection (sample rotation angle of 0°). The Polarization 1D LiDAR setup allows to conclude that polarization at a 1550nm LiDAR is capable of distinguishing between at least some relevant materials of great importance in autonomous vehicle safety.

The polarimetric response of the reflected light add information that does not depend on the reflectance of the targets, but on the materials constitution (note that the analysed Stokes vectors were normalized).

The studies reported in this present document allow to infer that polarization used in LiDAR must help a vehicle to make a more trustworthy decision and to avoid possible obstacles with lower time response.

10. Future Work

The results obtained in this thesis show that to combine polarimetric techniques with distance measurements can enhance the detection of road scene objects in autonomous driving applications. For this reason, future work that aims to improve the obtained results is proposed, in order to continue this project.

For future work, it is vital to increase the number of measured samples to enhance the plausibility of the present conclusions. The study should be kept by analysing the Mueller matrix of a great number of samples, and then, to determine the most adequate polarization state of emission that will cause a more distinguishable polarimetric response in the detection.

Furthermore, it could be interesting to study real-world samples in "out of the laboratory" conditions, as they can introduce relevant information to identify material classes. Note that there are various road scene objects that can not be measured in our laboratory (such as walls or crosswalks).

Moreover, after assembling an extensive data basis of different materials, a machine learning algorithm could and should be implemented to allow a quick material determination. In addition, it can be studied if it is necessary to know the sample rotation to distinguish road scene objects.

Also, it is important to continue working on the present Polarization 1D LiDAR, by upgrading it into a 3D Polarization LiDAR by means of controlling the MEMS mirror already implemented in the setup.

Bibliography

[1] worldometers, "Cars produced in the world - Worldometers," *worldometers*. [Online]. Available: https://www.worldometers.info/cars/. [Accessed: 07-Nov-2019].

[2] S. Thrun, "Toward robotic cars," *Commun. ACM*, vol. 53, no. 4, pp. 99–106, 2010, doi: 10.1145/1721654.1721679.

[3] S. Bundesamt, "Traffic accidents," *Destastis*. [Online]. Available: https://www.destatis.de/EN/Themes/Society-Environment/Traffic-Accidents/_node.html. [Accessed: 11-Nov-2019].

[4] WHO, "Climate impacts," *WHO*. [Online]. Available: https://www.who.int/sustainable-development/transport/health-risks/climate-impacts/en/. [Accessed: 11-Nov-2019].

[5] "WHO | Climate impacts," *WHO*, 2016.

[6] S. Narnakaje, "TI ' s smart sensors ideal for automated driving applications," *Texas Instruments*, pp. 1–7, 2017.

[7] A. K. Bhoopalam, N. Agatz, and R. Zuidwijk, "Planning of truck platoons: A literature review and directions for future research," *Transp. Res. Part B Methodol.*, vol. 107, pp. 212–228, Jan. 2018, doi: 10.1016/j.trb.2017.10.016.

[8] M. Alawadhi, J. Almazrouie, M. Kamil, and K. A. Khalil, "A systematic literature review of the factors influencing the adoption of autonomous driving," *Int. J. Syst. Assur. Eng. Manag.*, 2020, doi: 10.1007/s13198-020-00961-4.

[9] E. Guerra, "Planning for Cars That Drive Themselves: Metropolitan Planning Organizations, Regional Transportation Plans, and Autonomous Vehicles," *J. Plan. Educ. Res.*, vol. 36, no. 2, pp. 210–224, 2015, doi: 10.1177/0739456X15613591.

[10] KPMG, "Autonomous Vehicles Readiness Index Quick reader guide," *KPMG Int.*, 2019.

[11] M. Maurer, J. C. Gerdes, B. Lenz, and H. Winner, *Autonomous driving: Technical, legal and social aspects*. Springer Berlin Heidelberg, 2016.

[12] Benjamin Zhang, "Morgan Stanley: Autonomous Cars May Save US A Trillion Dollars," *Business Insider*, 2014. [Online]. Available: https://www.businessinsider.com/morgan-stanley-autonomous-cars-trillion-dollars-2014-9?IR=T. [Accessed: 11-Nov-2019].

[13] J. Kellett, R. Barreto, A. Van Den Hengel, and N. Vogiatzis, "How Might Autonomous Vehicles Impact the City? The Case of Commuting to Central Adelaide," *Urban Policy Res.*, vol. 37, no. 4, pp. 442–457, 2019, doi: 10.1080/08111146.2019.1674646.

[14] D. Feng, L. Rosenbaum, F. Timm, and K. Dietmayer, "Leveraging heteroscedastic aleatoric uncertainties for robust real-time LiDAR 3D object detection," in *IEEE Intelligent Vehicles Symposium, Proceedings*, 2019, vol. 2019-June, pp. 1280–1287, doi: 10.1109/IVS.2019.8814046.

[15] Grand View Research, "ADAS Market Size Worth $67," *Grand View Research*, 2018. [Online]. Available: https://www.grandviewresearch.com/press-release/global-advanced-driver-assistance-systems-adas-market. [Accessed: 11-Nov-2019].

[16] BMW Group, "AUTONOMES FAHREN BEI DER BMW GROUP." [Online]. Available: https://www.bmwgroup.com/en/NEXTGen/automated_driving.html. [Accessed: 22-Jul-2020].

[17] Volvocars, "Autonomous driving explained | Volvo Cars," *Volvo Cars*, 2016. [Online]. Available: https://www.volvocars.com/en-kw/own/own-and-enjoy/autonomous-driving. [Accessed: 22-Jul-2020].

[18] Groupe PSA., "Autonomous car & driving : vehicle automation | Groupe PSA." [Online]. Available: https://www.groupe-psa.com/en/story/en-route-vers-la-voiture-autonome/. [Accessed: 22-Jul-2020].

[19] SAE International, *Surface Vehicle Information Report - Alternative Automotive Fuels*. 2017.

[20] SAE, "Surface Vehicle," *SAE Int.*, p. 30, 2016.

[21] "SAE J3016 automated-driving graphic," *SAE International*, 2019. [Online]. Available: https://www.sae.org/news/2019/01/sae-updates-j3016-automated-driving-graphic. [Accessed: 11-Nov-2019].

[22] SAE International, "SAE Six Levels of Automation," *Www.Sae.Org/Autodrive*, 2014, doi: P141661.

[23] "Automated mobility," *Bosch Mobility Solutions*, 2019. [Online]. Available: https://www.bosch-mobility-solutions.com/en/highlights/automated-mobility/. [Accessed: 11-Nov-2019].

[24] T. Team, "Just How Far Ahead Is Tesla In Self-Driving?," *Forbes*, 2019. [Online]. Available: https://www.forbes.com/sites/greatspeculations/2019/11/08/just-how-far-ahead-is-tesla-in-self-driving/#224f5d481b24. [Accessed: 13-Nov-2019].

[25] A. FROST, "Hyundai successfully demonstrates autonomous truck platooning in Korea," *Traffic Technology Today*, 2019. [Online]. Available: https://www.traffictechnologytoday.com/news/autonomous-vehicles/hyundai-successfully-demonstrates-autonomous-truck-platooning-in-korea.html. [Accessed: 13-Nov-2019].

[26] J. Hughes, "Car Autonomy Levels Explained - The Drive," *TheDrive*, 2017. [Online]. Available: https://www.thedrive.com/sheetmetal/15724/what-are-these-levels-of-autonomy-anyway. [Accessed: 13-Nov-2019].

[27] J. Walker, "The Self-Driving Car Timeline – Predictions from the Top 11 Global Automakers | Emerj - Artificial Intelligence Research and Insight," *Emerj*, 2019. [Online]. Available: https://emerj.com/ai-adoption-timelines/self-driving-car-timeline-themselves-top-11-automakers/. [Accessed: 13-Nov-2019].

[28] K. Burke, "How Does a Self-Driving Car See?," *NVIDIA Blog*, 2019. [Online]. Available: https://blogs.nvidia.com/blog/2019/04/15/how-does-a-self-driving-car-see/. [Accessed: 15-Nov-2019].

[29] L. A. Klein, *Sensor and data fusion: A tool for information assessment and decision making: Second edition*, Second Edi. Spie, 2012.

[30] T. Dawkins, "Sensors Used In Autonomous Vehicles | Level Five Supplies," *Level Five Supplies*, 2019. [Online]. Available: https://levelfivesupplies.com/sensors-used-in-autonomous-vehicles/. [Accessed: 15-Nov-2019].

[31] T. Dawkins, “Sensors Used In Autonomous Vehicles | Level Five Supplies,” *Level Five Supplies*, 2019. [Online]. Available: https://levelfivesupplies.com/sensors-used-in-autonomous-vehicles/. [Accessed: 18-Nov-2019].

[32] H. K. Heidarsson and G. S. Sukhatme, “Obstacle detection and avoidance for an autonomous surface vehicle using a profiling sonar,” *Proc. - IEEE Int. Conf. Robot. Autom.*, pp. 731–736, 2011, doi: 10.1109/ICRA.2011.5980509.

[33] D. F. Meng, “What Will it Take for Fully Autonomous Vehicles to Become a Reality?,” *Viviota*, 2018. [Online]. Available: https://blog.viviota.com/what-will-it-take-for-fully-autonomous-vehicles-to-become-a-reality. [Accessed: 19-Feb-2020].

[34] S. Ipek, B. Scannell, and A. Parr, “The Autonomous Industrial Revolution | Analog Devices,” *Analog Devices*. [Online]. Available: https://www.analog.com/en/technical-articles/autonomous-industrial-revolution.html?gclid=EAIaIQobChMIsNeq5tfz5QIVBLDtCh2VdgLKEAAYASAAEgI7GvD_BwE#&as_qdr=y15. [Accessed: 18-Nov-2019].

[35] “Camera Based Moving Object Detection for Autonomous Driving,” pp. 1–10, 2017.

[36] K. Burke, “How Does a Self-Driving Car See?,” *nvidia*, 2019. [Online]. Available: https://blogs.nvidia.com/blog/2019/04/15/how-does-a-self-driving-car-see/. [Accessed: 18-Nov-2019].

[37] E. Yurtsever, J. Lambert, A. Carballo, and K. Takeda, “A Survey of Autonomous Driving: Common Practices and Emerging Technologies,” *arXiv Cornell Univ.*, 2019.

[38] M. Hansard, S. Lee, O. Choi, and R. Horaud, *Time of Flight Cameras : Principles , Methods , and Applications*. 2012.

[39] G. Rollmann, V. Schmid, M. Mekhaiel, and P. M. Knoll, “Short Range Radar System for Automotive Applications,” in *Advanced Microsystems for Automotive Applications 2003*, Springer Berlin Heidelberg, 2007, pp. 215–221.

[40] H. H. Meinel, “Evolving automotive radar - From the very beginnings into the future,” in *8th European Conference on Antennas and Propagation, EuCAP 2014*, 2014, pp. 3107–3114, doi: 10.1109/EuCAP.2014.6902486.

[41] European Commission, “A radar for your car | Shaping Europe’s digital future,” *European Commission*. [Online]. Available: https://ec.europa.eu/digital-single-market/en/node/329. [Accessed: 23-Jul-2020].

[42] J. Kocic, N. Jovicic, and V. Drndarevic, “Sensors and Sensor Fusion in Autonomous Vehicles,” in *2018 26th Telecommunications Forum, TELFOR 2018 - Proceedings*, 2018, doi: 10.1109/TELFOR.2018.8612054.

[43] G. Reina, D. Johnson, and J. Underwood, “Radar sensing for intelligent vehicles in urban environments,” *Sensors (Switzerland)*, vol. 15, no. 6, pp. 14661–14678, Jun. 2015, doi: 10.3390/s150614661.

[44] L. Frenzel, “Ultrasonic Sensors: A Smart Choice for Shorter-Range Applications,” *Electronic Design*, 2018. [Online]. Available: https://www.electronicdesign.com/industrial-automation/ultrasonic-sensors-smart-choice-shorter-range-applications. [Accessed: 18-Nov-2019].

[45] D. Langer and C. Thorpe, "Sonar Based Outdoor Vehicle Navigation and Collision Avoidance," *IEEE Int. Conf. Intell. Robot. Syst.*, vol. 2, pp. 1445–1450, 1992, doi: 10.1109/IROS.1992.594572.

[46] C. LAUTER, "Aurora to acquire Blackmore and their velocity-detecting lidar," *SPAR 3D*, 2019. [Online]. Available: https://www.spar3d.com/news/lidar/aurora-to-acquire-blackmore-adding-velocity-detecting-lidar-to-their-toolbox/. [Accessed: 23-Jul-2020].

[47] P. McManamon, *Field Guide to Lidar*. 2015.

[48] W. F. Blanchard, *Introduction to satellite navigation*, vol. 12, no. 5. 1994.

[49] Frost & Sullivan, "LiDAR: Driving the Future of Autonomous Navigation," *Frost & Sullivan*, pp. 1–30, 2016.

[50] G. Smolka, "Market trends in automotive lidar," *Photonics Spectra*, vol. 54, no. 1. pp. 56–59, 2020.

[51] W. Elmenreich, "Sensor Fusion in Time-Triggered Systems," Technischen Universit¨at Wien, 2002.

[52] D. Galar and U. Kumar, "Sensors and Data Acquisition," in *eMaintenance*, 2017, pp. 1–72.

[53] K. Heineke, P. Kampshoff, A. Mkrtchyan, and E. Shao, "Self-driving car technology: When will the robots hit the road?," *McKinsey Co.*, no. May, pp. 1–14, 2017.

[54] The Economist, "Self-driving cars need plenty of eyes on the road," *The Economist*, 2018. [Online]. Available: https://www.economist.com/graphic-detail/2018/03/02/self-driving-cars-need-plenty-of-eyes-on-the-road. [Accessed: 19-Feb-2020].

[55] U. Wandinger, "Introduction to Lidar," *Lidar*, pp. 1–18, 2006, doi: 10.1007/0-387-25101-4_1.

[56] P. F. McManamon, *LiDAR Technologies and Systems*. 2019.

[57] H. K. V Lotsch *et al.*, *LiDAR: Range-Resolved Optical Remote Sensing of the Atmosphere*. Springer, 2009.

[58] O. Cameron, "An Introduction to LIDAR: The Key Self-Driving Car Sensor," *voyage*, 2017.

[59] M. J. Starek, "Light detection and ranging (Lidar)," in *Encyclopedia of Earth Sciences Series*, 2016, p. 383.

[60] V. LiDAR, "How LiDAR Technology Enables Autonomous Cars to Operate Safely," *Velodyne LiDAR*, 2018. [Online]. Available: https://velodynelidar.com/newsroom/how-lidar-technology-enables-autonomous-cars-to-operate-safely/. [Accessed: 09-Dec-2019].

[61] J. Hecht, "Lasers for Lidar: FMCW lidar: An alternative for self-driving cars | Laser Focus World," *Laser Focus World*, 2019. [Online]. Available: https://www.laserfocusworld.com/home/article/16556322/lasers-for-lidar-fmcw-lidar-an-alternative-for-selfdriving-cars. [Accessed: 09-Dec-2019].

[62] Fraunhofer IWES, "LIDAR BUOY FOR FLEXIBLE SITE ASSESSMENT."

[63] Velodyne Inc., "HDL-64E S3 User's Manual and Programming Guide (Rev G)," *Velodyne*, p. 54, 2013.

[64] K. M. Lynch, N. Marchuk, and M. L. Elwin, "Controller Area Network (CAN)," in *Embedded Computing and Mechatronics with the PIC32*, 2016, pp. 249–265.

[65] B. E. A. Saleh and M. C. Teich, *Chapter 17: Semiconductor photon detectors*, Third. New York, USA: John Wiley & Sons, Inc., 2019.

[66] G. Lotha, “Stimulated emission | physics | Britannica,” *Britannica*, 2009. [Online]. Available: https://www.britannica.com/technology/stimulated-emission. [Accessed: 13-Dec-2019].

[67] I. C. Ferreira and M. I. Vasilevskiy, *Fisica Dos Semicondutores Fundamentos, Aplicacoes E Nanoestruturas*. Livraria Almedina, 2006.

[68] L. Kwok-san and T. Shiu-sing, “Further physics - What is laser?,” *Physics World*. [Online]. Available: http://www.hk-phy.org/articles/laser/laser_e.html. [Accessed: 10-Dec-2019].

[69] B. S. Rinkevichyus, I. L. Raskovskaya, and A. V. Tolkachev, “Principles and applications of laser refractography,” in *Proceedings - 2014 International Conference Laser Optics, LO 2014*, 2014, doi: 10.1109/LO.2014.6886398.

[70] C. E. Community, “Section 2.3: Basic Principles of Lasers,” *Advanced Manufacturing Laboratory*. [Online]. Available: http://www.aml.engineering.columbia.edu/ntm/level1/ch02/html/l1c02s03.html. [Accessed: 13-Dec-2019].

[71] P. Blood, “Principles of semiconductor lasers,” *Semicond. Lasers*, 2013.

[72] M. Griot, “Basic laser principles,” in *Introduction to Laser Technology*, 2009, pp. 36.2-36.32.

[73] F. Mandl, *Statistical Physics*. John Wiley & Sons, Inc., 2013.

[74] O. Svelto, *Principles of lasers*. Plenum Press, 2010.

[75] A. P. Napartovich, “Optical resonators,” in *Gas Lasers*, 2016, pp. 161–182.

[76] LiDAR - UK, “How does LiDAR work? The science behind the technology.,” *LiDAR - UK*, 2018. [Online]. Available: http://www.lidar-uk.com/how-lidar-works/. [Accessed: 10-Dec-2019].

[77] Tarun Agarwal, “All You Know About LIDAR Systems and Applications,” *ELPROCUS*, 2016. [Online]. Available: https://www.elprocus.com/lidar-light-detection-and-ranging-working-application/. [Accessed: 10-Dec-2019].

[78] HSU, “Components of a Lidar System,” *Humboldt State University*, 2015. [Online]. Available: http://gsp.humboldt.edu/OLM/Courses/GSP_216_Online/lesson7-1/components.html. [Accessed: 10-Dec-2019].

[79] Laser Focus World, “Automotive Lidar : Safety questions raised about 1550 nm lidar,” *World news*, pp. 13–16, 2019.

[80] International Electrotechnical Commission, “Safety of laser products - Part 1: Equipment classification, requirements and user’s guide (IEC 60825-1:1993+AMD1:1997+AMD2:2001 CSV),” *IEC*, p. 115, 2001.

[81] M. Born and E. Wolf, *Principles of Optics: Electromagnetic Theory of Propagation Interference and Diffraction of Light*, 7th editio. Cambridge University Press, 2013.

[82] M. V. Klein and T. E. Furtak, *Optics*. John Wiley & Sons, Inc., 1985.

[83] E. H. Linfoot, “Principles of Optics,” *Opt. Acta Int. J. Opt.*, vol. 8, no. 2, pp. 181–182, 1961, doi:

10.1080/713826373.

[84] R. Waters, “Circular aperture Rectangular aperture Fraunhofer Diffraction,” 2016. [Online]. Available: https://slideplayer.com/slide/7598459/. [Accessed: 06-Jan-2020].

[85] C. F. Bohren and D. R. Huffman, *Absorption and Scattering of Light by Small Particles*. Wiley, 1998.

[86] F. Corrigan, “UAVs In The Lidar Applications Sector Increases Substantially,” *DroneZon*, 2015.

[87] M. Wahl, “Time-Correlated Single Photon Counting,” *PicoQuant*, pp. 1–14, 2017.

[88] I. Edinburgh Instruments, “Time-Resolved Fluorescence | Edinburgh Instruments,” *Edinburgh Instruments*. [Online]. Available: https://www.edinst.com/techniques/time-resolved-fluorescence/. [Accessed: 19-Mar-2020].

[89] W. Becker, *The bh TCSPC Handbook*, Eigth. Becker & Hickl GmbH, 2010.

[90] T. S. P. Counting, “TCSPC – What is Time-Correlated Single Photon Counting ?,” *Edinburgh Instruments*, pp. 1–5, 2020.

[91] S. V. Polyakov, O. H. W. Siegmund, S. N. Ahmed, S. Roth, A. Maitland, and M. F. L’ANNUNZIATA, “Photomultiplier Tubes - an overview,” *ScienceDirect Topics*. [Online]. Available: https://www.sciencedirect.com/topics/physics-and-astronomy/photomultiplier-tubes. [Accessed: 22-Mar-2020].

[92] D. R. Paschotta, “Photomultipliers,” *RP Photonics*. [Online]. Available: https://www.rp-photonics.com/photomultipliers.html. [Accessed: 22-Mar-2020].

[93] S. V. Polyakov, “Photomultiplier Tubes,” in *Experimental Methods in the Physical Sciences*, vol. 45, 2013, pp. 69–82.

[94] YAWD, “Radiation drawing cloud chamber, radiation drawing cloud chamber #2370135.” [Online]. Available: https://ya-webdesign.com/imgdownload.html. [Accessed: 20-Mar-2020].

[95] P. Seitz and A. J. P. Theuwissen, *Single-Photon Imaging*. Springer Science & Business Media, 2011.

[96] B. Leskovar, “Microchannel plates,” *Phys. Today*, vol. 30, no. 11, pp. 42–49, 1977, doi: 10.1063/1.3037791.

[97] Del Mar Photonics, “Microchannel Plates,” *Del Mar Photonics*. [Online]. Available: http://www.dmphotonics.com/MCP_MCPImageIntensifiers/microchannel_plates.htm. [Accessed: 22-Mar-2020].

[98] Hamamatsu Photonics, “Microchannel plates (MCPs),” *Hamamatsu Photonics*. [Online]. Available: https://www.hamamatsu.com/us/en/product/optical-sensors/electron_ion-sensor/mcp/index.html. [Accessed: 22-Mar-2020].

[99] Andreas, “Mcp-de.svg.” [Online]. Available: https://commons.wikimedia.org/wiki/File:Mcp-de.svg. [Accessed: 22-Mar-2020].

[100] G. Ripoche and J. Harari, “Avalanche photodiodes,” in *Optoelectronic Sensors*, 2010, pp. 58–109.

[101] M. Hodges, “Improved APD design boosts photon-counting detector efficiency,” *Laser Focus World*, vol. 48, no. 5, pp. 66–69, 2012.

[102] W. Jiang, Y. Chalich, and M. J. Deen, “Sensors for positron emission tomography applications,”

Sensors (Switzerland), vol. 19, no. 22, 2019, doi: 10.3390/s19225019.

[103] D. R. Paschotta, "Photomultipliers," *RP Photonics*. .

[104] M. D. Williams, "Photon counting [2]," *Science*, vol. 215, no. 4534. p. 745, 1982, doi: 10.1126/science.215.4534.745-a.

[105] J. Yoshida, "Lidar Tech Today, Lidar Vendors Tomorrow," *EE Times*, 2018. [Online]. Available: https://www.eetimes.com/lidar-tech-today-lidar-vendors-tomorrow/. [Accessed: 23-Mar-2020].

[106] S. Royo and M. Ballesta-Garcia, "An overview of lidar imaging systems for autonomous vehicles," *Appl. Sci.*, vol. 9, no. 19, 2019, doi: 10.3390/app9194093.

[107] "Alpha Prime | Velodyne Lidar," *Velodyne Lidar*. [Online]. Available: https://velodynelidar.com/products/alpha-prime/. [Accessed: 02-Apr-2020].

[108] Scanlab, "File:Plexi Galvohalter.jpg." [Online]. Available: https://commons.wikimedia.org/wiki/File:Plexi_Galvohalter.jpg. [Accessed: 14-Mar-2020].

[109] V. C. Coffey, "What you need to know to buy a galvo-positioner," *Laser Focus World*, vol. 46, no. 9, pp. 61–63, 2010.

[110] Engineering 360, "Galvanometer Optical Scanners Information," *GlobalSpec*. [Online]. Available: https://www.globalspec.com/learnmore/optics_optical_components/optoelectronics/optical_scanners. [Accessed: 14-Mar-2020].

[111] G. F. Marshall, *Handbook of Optical and Laser Scanning*. 2016.

[112] M. Ozdogan, M. Daeichin, A. Ramini, and S. Towfighian, "Parametric resonance of a repulsive force MEMS electrostatic mirror," *Sensors Actuators, A Phys.*, vol. 265, pp. 20–31, 2017, doi: 10.1016/j.sna.2017.07.043.

[113] A. Strasser, P. Stelzer, C. Steger, and N. Druml, "Towards synchronous mode of multiple independently controlled MEMS mirrors," in *IFAC-PapersOnLine*, 2019, vol. 52, no. 15, pp. 31–36, doi: 10.1016/j.ifacol.2019.11.645.

[114] J. Rigelsford, "MEMS Scanning Mirror," *Sens. Rev.*, vol. 23, no. 3, 2003, doi: 10.1108/sr.2003.08723cad.011.

[115] I. PALOMAR TECHNOLOGIES, "Micro-Optoelectronic Mechanical Systems (MOEMS)," *Palomar Technologies*, 2019. [Online]. Available: https://www.palomartechnologies.com/applications/micro-optoelectronic-mechanical-systems. [Accessed: 15-Mar-2020].

[116] D. Shaddock, "Laser beam steering subsystem - an optical phased array," *DQS - ANU*, 2019. [Online]. Available: https://physics.anu.edu.au/quantum/cgp/research/spacetech/gracefo/optical-phased-array.php. [Accessed: 16-Mar-2020].

[117] L. Xu, J. Zhang, and L. Y. Wu, "An Optical Phased Array for LIDAR," doi: 10.1088/1742-6596/772/1/012004.

[118] B. Wowk, "Phased Array Optics," in *Nanotechnology*, 2020.

[119] D. Schoech and D. Schoech, "Technology: Overview," in *Encyclopedia of Social Work*, 2013.

[120] N. Aeronautics, "Super Resolution 3D Flash LIDAR," *Nasa Technol.*, 2011.

[121] F. Amzajerdian, V. E. Roback, P. F. Brewster, G. D. Hines, and A. Bulyshev, "Imaging Flash Lidar for Autonomous Safe Landing and Spacecraft Proximity Operation."

[122] J. Peii, M. McCord, and J. Ye, "US20170307758A1 - Scanning Lidar Systems for Three-Dimensional Sensing - Google Patents," 2017. [Online]. Available: https://patents.google.com/patent/US20170307758?oq=micro+motion+technology+cepton+patent. [Accessed: 17-Mar-2020].

[123] Cepton Technologies Inc, "Miniature Lidar," *Photonics Spectra*, 2018. [Online]. Available: https://www.photonics.com/Products/Miniature_Lidar/pr63328. [Accessed: 17-Mar-2020].

[124] Electronic Engineering Journal, "Cepton LiDAR Goes Anti-MEMS Route," *EEJournal*. [Online]. Available: https://www.eejournal.com/article/cepton-lidar-goes-anti-mems-route/. [Accessed: 17-Mar-2020].

[125] Cepton Technologies Inc, "The Silicon Valley Approach to Lidar Sensor Development," 2018.

[126] J. Thompson, "100 real-world applications of LiDAR," *ITProPortal*, 2020.

[127] F. Zhao, H. Jiang, and Z. Liu, "Recent development of automotive LiDAR technology, industry and trends," in *SPIE*, 2019, no. August 2019, p. 178, doi: 10.1117/12.2540277.

[128] N. C. NEBRASKA, "LiDAR Market 2020-2023 | Global Industry Key Players, Facts, Fig," *NEWS CHANNEL NEBRASKA*. [Online]. Available: https://www.newschannelnebraska.com/story/41560851/lidar-market-20202023-global-industry-key-players-facts-figures-share-trends-applications-analytical-insights-segmentation-and-forecast-with-competitive-landscape-by-2023. [Accessed: 02-Mar-2020].

[129] N. Wijeyasinghe and K. Ghaffarzadeh, "Lidar 2020-2030," in *Technologies, Players, Markets & Forecasts*.

[130] CES, "CES - The Global Stage for Innovation - CES 2020," *Consumer Technology Association*, 2019. [Online]. Available: https://www.ces.tech/. [Accessed: 24-Mar-2020].

[131] Velodyne Inc., "velabit sensor released by velodyne | Vision Systems Design," *Velodyne Inc.* [Online]. Available: https://www.vision-systems.com/3d-imaging/article/14169507/velabit-sensor-released-by-velodyne. [Accessed: 24-Mar-2020].

[132] P. E. Ross, "Velodyne Will Sell a Lidar for $100," *IEEE Spectrum*, 2020.

[133] J. R. Schott, *Fundamentals of polarimetric remote sensing*. SPIE PRESS, 2009.

[134] S. Cloude, *Polarisation: Applications in Remote Sensing*, First. Oxford University Press, 2010.

[135] J. S. Tyo, D. L. Goldstein, D. B. Chenault, and J. A. Shaw, "Review of passive imaging polarimetry for remote sensing applications," *OSA publishing*, pp. 5453–5469, 2006.

[136] F. Snik *et al.*, "An overview of polarimetric sensing techniques and technology with applications to different research fields," in *SPIE*, 2014.

[137] Leipzig, "Polarization LIDAR technique," *Tropos*.

[138] R. A. Reed *et al.*, "Lidar backscatter properties of Al2O3 rocket exhaust particle," *Spacecr. Rocket.*, vol. 42, pp. 711–715, 2005.

[139] K. Sassen, “Polarization in lidar: a review,” *Polariz. Sci. Remote Sens.*, vol. 5158, p. 151, 2003, doi: 10.1117/12.507006.

[140] G. David *et al.*, “UV polarization lidar for remote sensing new particles formation in the atmosphere,” *Opt. Express*, vol. 22, no. S3, p. A1009, 2014, doi: 10.1364/oe.22.0a1009.

[141] S. N. P. John H. Seinfeld, *Atmospheric Chemistry and Physics: From Air Pollution to Climate Change*. Wiley, 2006.

[142] D. M. Winker, J. R. Pelon, and M. P. McCormick, “The CALIPSO mission: spaceborne lidar for observation of aerosols and clouds,” in *Lidar Remote Sensing for Industry and Environment Monitoring III*, 2003, vol. 4893, p. 1, doi: 10.1117/12.466539.

[143] Paul S. Banks, “Systems and methods of high resolution three-dimensional imaging,” *US Pat. 8471895B2*, Nov. 2013.

[144] Paul S. Banks, B. Schmidt, C. S. Tuvey, and L. N. Venneri, “3d imaging system and method,” US20170248796A1, Feb-2017.

[145] J. B. dos Santos, “Proof-of-concept of a Single-point Time-of- Flight LiDAR System and Guidelines towards Integrated High-accuracy Timing, Advanced Polarization Sensing and Scanning with a MEMS Micromirror,” 2018.

[146] C. K. Keyser, R. K. Martin, P. K. Nguyen, and A. M. Adams, “Single-Pulse Mueller Matrix LiDAR Polarimeter: Modeling and Demonstration,” *IEEE Trans. Geosci. Remote Sens.*, vol. 57, no. 6, pp. 3296–3307, 2019, doi: 10.1109/TGRS.2018.2883242.

[147] D. G. Jones, D. H. Goldstein, and J. C. Spaulding, “Reflective and polarimetric characteristics of urban materials,” in *Polarization: Measurement, Analysis, and Remote Sensing VII*, 2006, vol. 6240, p. 62400A, doi: 10.1117/12.665012.

[148] E. M. Purcell and D. J. Morin, *Electricity and Magnetism*. Cambridge University Press, 2013.

[149] D. H. Goldstein, *Polarized Light*. 2014.

[150] “6. Spectroscopic Ellipsometry |,” *kristof lodewijks.be*. [Online]. Available: http://www.kristoflodewijks.be/research/theoretical-background/6-spectroscopic-ellipsometry/. [Accessed: 29-Mar-2020].

[151] R. M. A. Azzam and N. M. . Bashara, *Ellipsometry and Polarized Light*. North-Holland Publishing Company, 1977.

[152] R. A. Chipman, *Polarized Light and Optical Systems*. CRC Press, 2019.

[153] A. Peinado, “Design of polarimeters based on liquid crystals and biaxial crystals for polarization metrology,” Universitat Autònoma de Barcelona, 2014.

[154] “File:Poincare sphere.svg - Wikipedia.” [Online]. Available: https://en.wikipedia.org/wiki/File:Poincare_sphere.svg. [Accessed: 29-Mar-2020].

[155] J. Freudenthal, “Intuitive interpretation of Mueller matrices of transmission,” *Hinds Instruments*, 2018.

[156] S.-Y. Lu and R. A. Chipman, “Interpretation of Mueller matrices based on polar decomposition RETARDANCE : A REVIEW,” *J. Opt. Soc. Am. A*, vol. 13, no. 5, pp. 1106–1113, 1996.

[157] R. A. . Chipman, "Polarimetry," in *Handbook of Optical Metrology: Principles and Applications*, Second., 2015, pp. 627–675.

[158] A. Lizana, I. Estévez, A. Turpin, C. Ramirez, A. Peinado, and J. Campos, "Implementation and performance of an in-line incomplete Stokes polarimeter based on a single biaxial crystal," *Appl. Opt.*, vol. 54, no. 29, p. 8758, Oct. 2015, doi: 10.1364/ao.54.008758.

[159] K. M. Twietmeyer and R. A. Chipman, "Optimization of Mueller matrix polarimeters in the presence of error sources," *Opt. Express*, vol. 16, no. 15, p. 11589, 2008, doi: 10.1364/oe.16.011589.

[160] N. C. Bruce, J. M. López-Téllez, O. Rodríguez-Núñez, and O. G. Rodríguez-Herrera, "Permitted experimental errors for optimized variable-retarder Mueller-matrix polarimeters," *Opt. Express*, vol. 26, no. 11, p. 13693, 2018, doi: 10.1364/oe.26.013693.

[161] G. H. Golub and C. F. Van Loan, *Matrix Computation*, Fourth. JHU Press, 2013.

[162] R. A. Horn and C. R. Johnson, *Matrix Analysis*, Second. 2012.

[163] Thorlabs, "Thorlabs." [Online]. Available: https://www.thorlabs.com/. [Accessed: 03-Jun-2020].

[164] J. V.D. Wirjawan, "Consecutive polarizers arrangement producing maximum polarized light intensity," in *AIP Conference Proceedings*, 2016, doi: 10.1063/1.4943751.

[165] Allied Vision, "Digital Industrial Camera Solutions," *Allied Vision*. [Online]. Available: https://www.alliedvision.com/en/digital-industrial-camera-solutions.html. [Accessed: 07-Aug-2020].

[166] Kowa, "Kowa Industrial lenses for Machine Vision and CCTV." [Online]. Available: https://www.kowa-lenses.com/en/. [Accessed: 21-Jul-2020].

[167] B. J. DeBoo, J. M. Sasian, and R. A. Chipman, "Depolarization of diffusely reflecting man-made objects," *Appl. Opt.*, vol. 44, no. 26, pp. 5434–5445, Sep. 2005, doi: 10.1364/AO.44.005434.

[168] M. Optics, "Meadowlark Optics." [Online]. Available: https://www.meadowlark.com/. [Accessed: 03-Jun-2020].

[169] L. C. Suite, "Liquid Crystal Variable Retarders These," *Meadowlark Opt.*

[170] A. De Martino, Y.-K. Kim, E. Garcia-Caurel, B. Laude, and B. Drévillon, "Optimized Mueller polarimeter with liquid crystals," *Opt. Lett.*, vol. 28, no. 8, p. 616, Apr. 2003, doi: 10.1364/ol.28.000616.

[171] J. S. Tyo, "Design of optimal polarimeters: Maximization of signal-to-noise ratio and minimization of systematic error," *Appl. Opt.*, vol. 41, no. 4, pp. 619–630, 2002, doi: 10.1364/AO.41.000619.

[172] Velodyne, "Velodyne Lidar," *Http://Velodynelidar.Com/*, p. 2800, 2013.

[173] LeddarTech, "LeddarTech." [Online]. Available: https://leddartech.com/. [Accessed: 01-Aug-2020].

[174] Quanergy, "Quanergy – LiDAR sensors and smart sensing solutions." [Online]. Available: https://quanergy.com/. [Accessed: 01-Aug-2020].

[175] Valeo, "Valeo - Smart technology for smarter cars," *Valeo*. [Online]. Available: https://www.valeo.com/en/. [Accessed: 01-Aug-2020].

[176] Ouster, "High-resolution digital lidar: autonomous vehicles, robotics, drones." [Online]. Available: https://ouster.com/. [Accessed: 01-Aug-2020].

[177] M. Hirz and B. Walzel, “Sensor and object recognition technologies for self-driving cars,” *Comput. Aided. Des. Appl.*, vol. 15, no. 4, pp. 501–508, Jan. 2018, doi: 10.1080/16864360.2017.1419638.

[178] K. Company, “Keopsys company designs your fiber lasers and fiber amplifiers.” [Online]. Available: https://www.keopsys.com/. [Accessed: 17-Jun-2020].

[179] M. Systems, “High Sensitivity Avalanche Photodetector | Menlo Systems,” *Menlo Systems*. [Online]. Available: https://www.menlosystems.com/products/photodetectors/apd310/. [Accessed: 17-Jun-2020].

[180] Thorlabs, “Thorlabs - F240APC-1550 1550 nm, f = 8.18 mm, NA = 0.49 FC/APC Fiber Collimation Pkg.” [Online]. Available: https://www.thorlabs.com/thorproduct.cfm?partnumber=F240APC-1550. [Accessed: 30-Jun-2020].

[181] Thorlabs, “Mounted N-BK7 Plano-Convex Lenses (AR Coating: 650 - 1050 nm).” [Online]. Available: https://www.thorlabs.com/newgrouppage9.cfm?objectgroup_id=6278. [Accessed: 25-Jun-2020].

[182] Computar, “TEC-55 : Manual Iris: Monofocal Lenses: Products.” [Online]. Available: https://computar.com/product/561/TEC-55. [Accessed: 25-Jun-2020].

[183] T. LeCroy, “Teledyne LeCroy | Oscilloscopes | Protocol Analyzers.” [Online]. Available: https://teledynelecroy.com/. [Accessed: 30-Jun-2020].

[184] A. S. Huntington, *InGaAs Avalanche Photodiodes for Ranging and Lidar*. 2020.

[185] Jorge Leite Martins de Carvalho, *Sistemas de controle automático*. Livros Téc. e Cient. Editora, 2020.

[186] B. & H. GmbH, “Becker & Hickl GmbH.” [Online]. Available: https://www.becker-hickl.com/. [Accessed: 27-Jun-2020].

[187] Becker & Hickl GmbH, “A-PPI-D - Becker & Hickl GmbH.” [Online]. Available: https://www.becker-hickl.com/products/a-ppi-d/. [Accessed: 30-Jun-2020].

[188] E. Instruments, “What is TCSPC?,” 2013.

[189] J. Fjeldsted, “Time-of-Flight Mass Spectrometry.” .

[190] B. & H. GmbH., “TCSPC Package - Becker & Hickl GmbH,” *Becker & Hickl GmbH*. [Online]. Available: https://www.becker-hickl.com/products/tcspc-package/#product-download. [Accessed: 03-Jul-2020].

[191] “ISO 5725-1:1994(en), Accuracy (trueness and precision) of measurement methods and results — Part 1: General principles and definitions,” *International Organization for Standardization*, 1994. [Online]. Available: https://www.iso.org/obp/ui/#iso:std:iso:5725:-1:ed-1:v1:en. [Accessed: 06-Jul-2020].

[192] A. Sensors, “Understanding Accuracy and Precision for MEMS Pressure Sensors,” *All Sensors*, pp. 1–5.

[193] Thorlabs, “Thorlabs - WP25M-UB Ø25.0 mm Mounted Wire Grid Polarizer, 250 nm to 4 µm,” 2017. [Online]. Available: https://www.thorlabs.com/thorproduct.cfm?partnumber=WP25M-UB. [Accessed: 11-Jul-2020].

[194] Thorlabs, “Thorlabs - WPQ05M-1550 Ø1/2" Zero-Order Quarter-Wave Plate, Ø1" Mount, 1550 nm.” [Online]. Available: https://www.thorlabs.com/thorproduct.cfm?partnumber=WPQ05M-1550. [Accessed: 11-Jul-2020].

Annex A

Table 11. Normalized Evaluation of the 1D Lidar precision as a function of the distance range (Range (m)). Experimental Results Distributions and their best Gaussian fits.

Range (m)	Experimental Result Distribution and its best Gaussian fit	***Range*** (m)	***Experimental Result Distribution and its best Gaussian fit***
0.4999	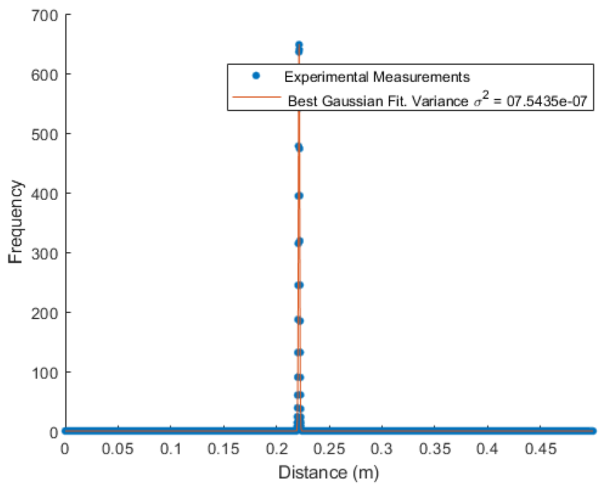	29.92	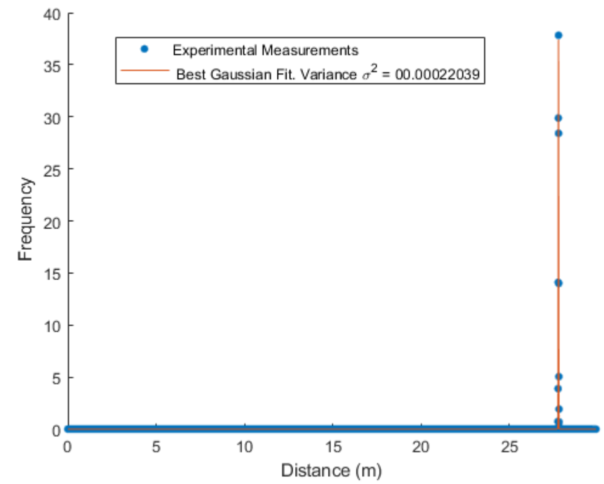
0.7498	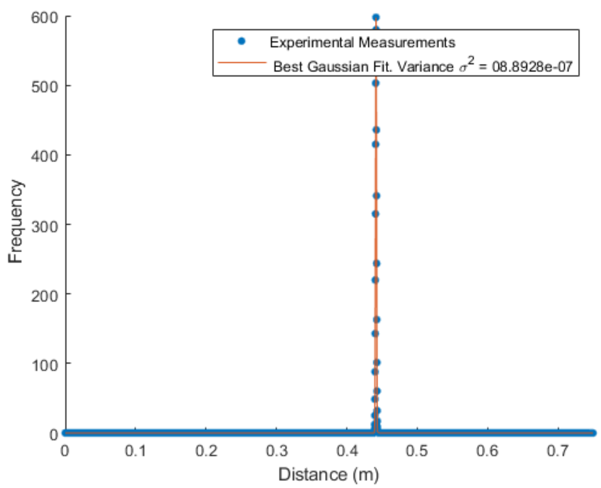	38.96	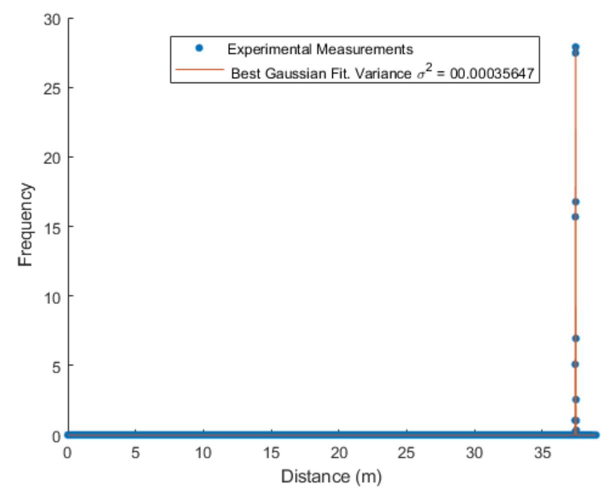

<table>
<tr>
<td>1.500</td>
<td>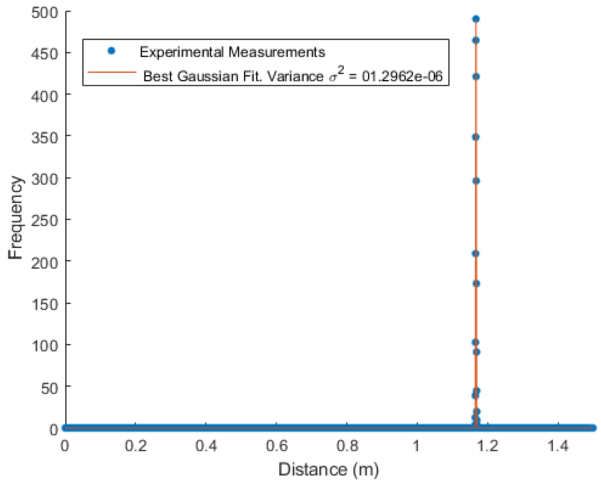
</td>
<td>44.99</td>
<td>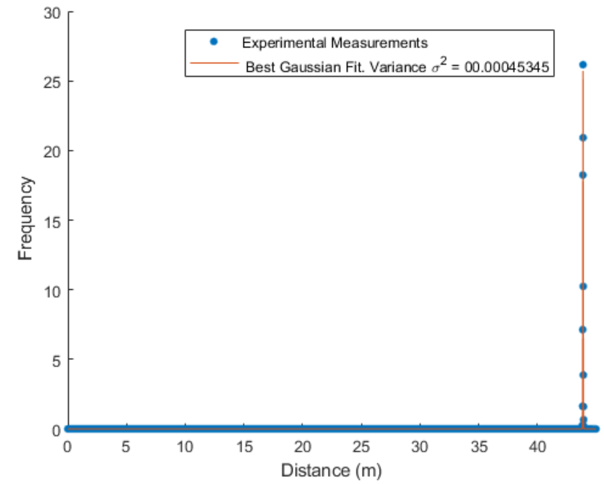
</td>
</tr>
<tr>
<td>3.749</td>
<td>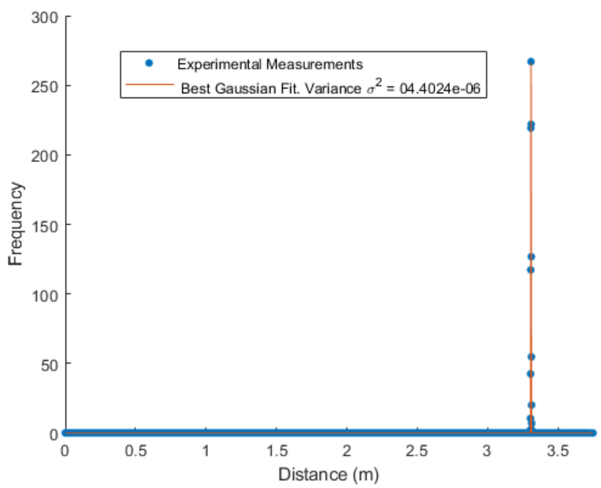
</td>
<td>59.84</td>
<td>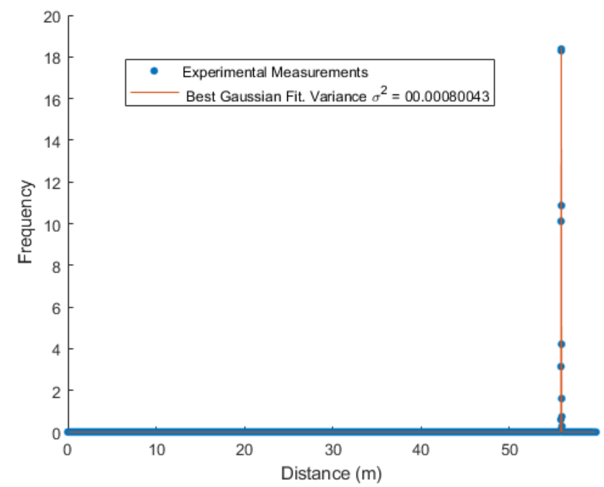
</td>
</tr>
</table>

7.498	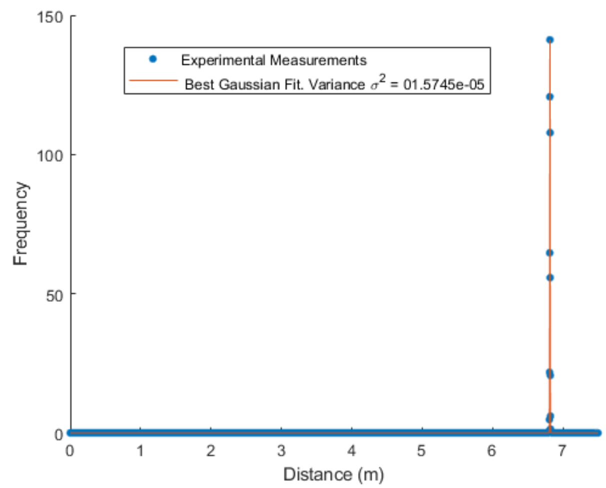	74.98	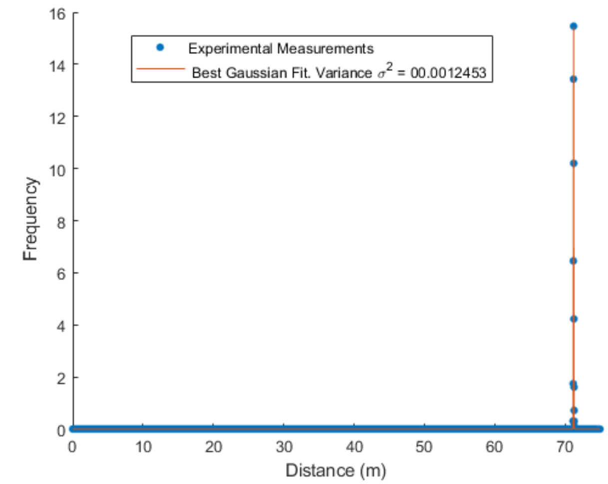
11.98	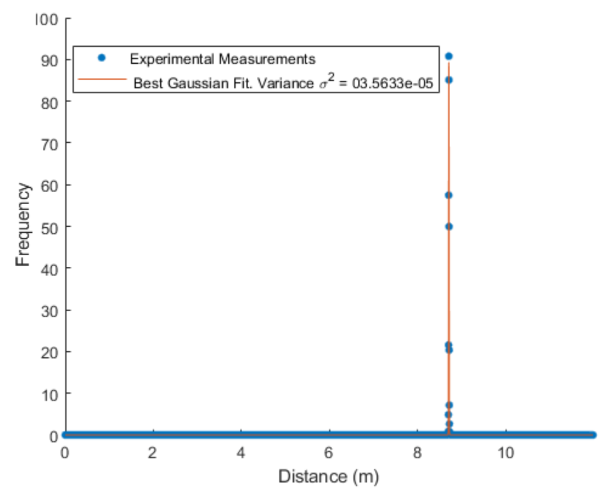	90.11	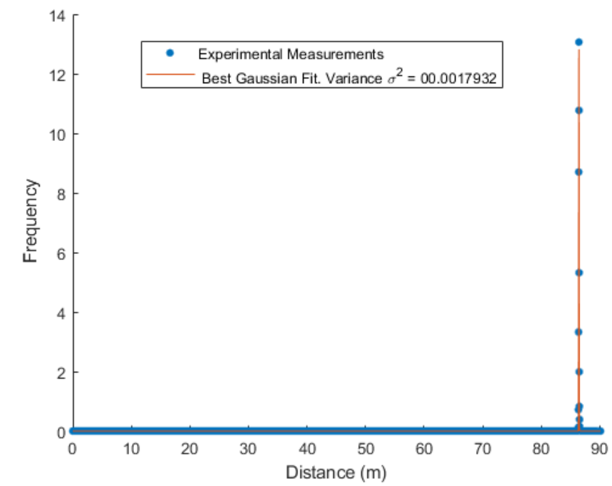

14.96	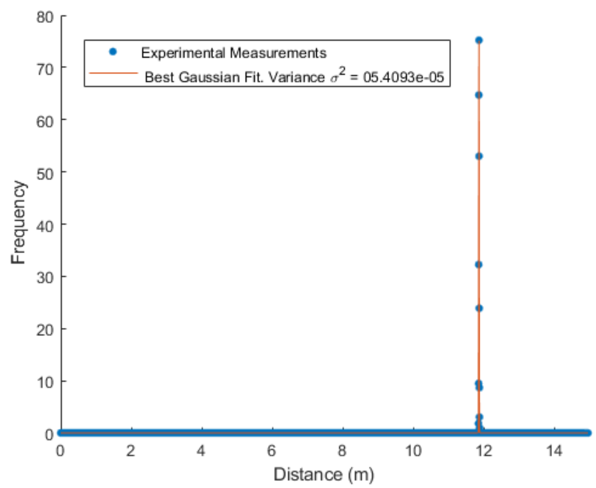	103.5	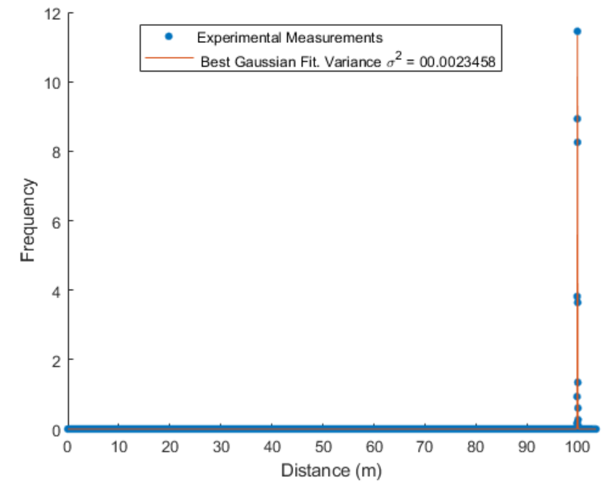
22.49